International
Progress Report

IPR-99-08

Äspö Hard Rock Laboratory

Impact of flow geometry, flow regime, two-phase flow and degassing on the transmissivity of rough fractures

John E. Gale

Fracflow Consultants Inc.

May 1999

Svensk Kärnbränslehantering AB
Swedish Nuclear Fuel
and Waste Management Co
Box 5864
SE-102 40 Stockholm Sweden
Tel 08-459 84 00
+46 8 459 84 00
Fax 08-661 57 19
+46 8 661 57 19

Äspö Hard Rock
Laboratory

Äspö Hard Rock Laboratory

Impact of flow geometry, flow regime, two-phase flow and degassing on the transmissivity of rough fractures

John E. Gale

Fracflow Consultants Inc.

May 1999

RAPPORTNUMMER
IPR-99-08

TILLHÖR/REG.NR
F60K

FÖRFATTARE
John Gale

DATUM

TILLSTYRKT

DATUM

GODKÄNT/FASTSTÄLLT
Olle Olsson

DATUM
1999-06-03

IMPACT OF FLOW GEOMETRY, FLOW REGIME, TWO-PHASE FLOW AND DEGASSING ON THE TRANSMISSIVITY OF ROUGH FRACTURES

John E. Gale
Fracflow Consultants Inc.
154 Major's Path
St. John's, Nfld. A1A 5A1
Canada

May 1999

Abstract

Three sets of laboratory experiments have been conducted to examine the impacts of gas evolving or degassing within fracture planes as the fluid pressure drops below the bubble pressure, or the pressure at which the water has been saturated with a specific gas, on the transmissivity of discrete fracture planes. These experiments were conducted on a large scale physical model, that contained a fracture plane created using a geotextile fabric, measuring approximately 3.5 square metres, four small samples that measured approximately 200 mm by 300 mm and a plastic replica of the fracture surface that was cast from a concrete model with a fracture surface that was formed by the same geotextile material.

The large scale physical model experiments demonstrated that flow regime and overall fracture transmissivity are major factors that can both mask or control the impacts of both two-phase flow and degassing on fracture transmissivity. Experiments on plastic replicas of the fracture surface used in the large scale physical model and the smaller concrete model, confirmed that the low trapping capacity and the high hydraulic conductivity that is present in fracture surfaces with this level of uniform roughness results in the gas bubbles being swept from the fracture plane before the bubbles can aggregate and reduce the fracture transmissivity. Single, two-phase and degassing flow experiments on the small scale samples also showed that the structure of the fracture pore space plays a major role in determining the relative importance of the degassing impacts that were observed. The degassing experiments on the small samples showed a clear reduction in fracture transmissivity due to degassing.

Numerical model simulations, utilizing the spatial structure of the fracture pore space that was generated by mapping the resin impregnated pore space, demonstrated that using physical measurements of the fracture pore space to provide local estimates of hydraulic conductivity provides an excellent match between measured and computed flowrates.

This suite of laboratory experiments and preliminary numerical simulations have demonstrated that degassing within fracture planes can produce significant changes in the apparent transmissivity of discrete fractures. The relative impact of degassing on fracture transmissivity is determined both by the magnitude of the fracture transmissivity, the fracture roughness or trapping capacity of the fracture plane, the type of gas present in the water phase and the percent of the gas that is dissolved in the water. In addition, the flow geometry and the resulting changes in flow regime with increasing flowrate or increasing hydraulic gradient can both mask changes in the observed fracture transmissivity and amplify these changes.

Executive Summary

This applied research programme includes three sets of laboratory experiments, which were conducted to examine the impacts of gas evolving or degassing within fracture planes as the fluid pressure drops below the bubble pressure, or the pressure at which the water has been saturated with a specific gas, on the transmissivity of discrete fracture planes. The main focus of this work was to determine the relative effects of sample size, fracture deformation, changes in flow regime, two-phase flow and degassing on changes in fracture transmissivity. In addition, these experiments were designed to examine the role of fracture roughness and relative fracture roughness on the trapping capacity of discrete fractures as these factors apply to changes in fracture transmissivity due to degassing.

In the first set of experiments, a series of single phase flow experiments that were being completed on an existing large scale physical model were extended to include a series of two-phase flow experiments. In these two-phase flow experiments, both water and gas were injected into the fracture plane at the same time. In addition, tests were conducted where a gas saturated water was injected into the fracture plane and the fluid pressure decreased to induce the gas to evolve or degass within the fracture plane. The Large Scale Physical Model (LSPM) provides a fracture surface that is approximately 3.5 square metres in area. This physical model was constructed from high strength concrete and the fracture plane was created by imprinting a geotextile fabric into the concrete surface between the two halves of the model. The resulting fracture plane was characterized by a uniform small scale roughness. A 50 mm diameter borehole was drilled into this fracture plane to intersect the fracture plane at an angle of 42 degrees in the center of the fracture plane, creating an elliptical opening or sink within the fracture plane. The fracture plane was instrumented with a series of manometers to measure pressure heads during linear, divergent or convergent flow experiments. Flatjacks, coupled to a reaction frame, were used to change the normal stress acting across the fracture plane and hence induce fracture closure. These changes in load permitted a range of relative fracture roughness to be created in the various single and two-phase flow experiments.

Single phase flow experiments on this large model showed that, with increasing flowrate, the change in flow regime from laminar to turbulent, or some degree of turbulence, produces additional head losses due to increased fluid velocity. When these head losses are used with the measured flowrates to compute fracture transmissivities, major changes in the fracture transmissivity are computed. The addition of gas to the injection water introduced additional head losses and hence additional changes in fracture transmissivity. However, the two-phase flow impacts can be masked by the changes induced by the changes in the flow regime. In addition, the fracture in this LSPM was highly conductive, with a uniform roughness that produced a low gas trapping capacity, and the high flowrates that were associated with the high hydraulic gradients tended to sweep both the raw gas phase during the two-phase experiments and the gas bubbles that were assumed to have evolved during the degassing experiments out of the fracture plane before the gas could form effective blockage of the fracture pore space. However,

despite these offsetting impacts, significant reductions in fracture transmissivity during the two-phase flow experiments were measured. It is clear that degassing in field situations will be most apparent in rough fractures with low to moderate transmissivities in which the borehole has a small angle of intersection with the fracture plane.

The main effort in this laboratory program consisted of a series of degassing experiments on four small scale samples of both artificial and natural fracture planes. The samples were nominally about 200 mm wide by 300 mm in length. One sample was formed by sand-blasting a sawcut in a limestone sample. The second sample was constructed from high strength concrete using the geotextile approach used in constructing the LSPM discussed above. The two other fracture samples were obtained by overcoring natural fractures at the Pilot Resin site at Äspö. These samples were subjected to a series of normal and shear (for the limestone and concrete samples) loading and unloading cycles that, as the fractures closed and opened, generated a range of relative roughness on the fracture planes. Both single phase, air invasion (imibibition) and air injection tests were conducted on the first two samples. The full suite of tests were completed on the two Äspö samples, including a full suite of degassing experiments at different normal stress levels using water saturated either with carbon dioxide or nitrogen at the water injection pressure.

The air invasion and air injection tests, which focused on measuring the volume of water expelled from the fracture plane, should reflect the differences in the fracture pore structure and the resulting capillary pressure within the fracture plane. However, the interpretation of these tests is unclear due to experimental difficulties. For example, when conducting tests using air or nitrogen gas followed by tests using carbon dioxide gas, the carbon dioxide tended to flush out the air or nitrogen from the fracture plane, producing an increase in fracture transmissivity rather than a decrease.

For degassing experiments on the first Äspö sample, most of the experiments were conducted with water that was saturated with carbon dioxide gas due to its lower bubble pressure and the higher gas contents that could be achieved at the proposed test pressures. For these experiments, reductions in fracture transmissivity were clearly noted at the different stress levels as the outlet pressure was dropped below the bubble pressure. However, the fracture transmissivity values tended to fluctuate considerably at each pressure step which was assumed to be partly due to a periodic flushing of evolved gas from the fracture plane or capillary pressure effects on the manometer tubes that were used to measure the fluid pressures. This assumption is consistent with the periodic spurts of bubbles of gas in the discharge line. Degassing with nitrogen gas produced a much more stable set of fracture transmissivity values as the outlet pressure was dropped below the bubble pressure. Degassing experiments on the second Äspö sample produced a clear demonstration of the impacts of evolving nitrogen gas on the transmissivity of a discrete fracture. At each normal stress level, as the outlet pressure was decreased below the bubble pressure there was a clear decrease in the fracture transmissivity due to degassing. The role of other factors, such as head loss due to increased fluid velocity and possible changes in the flow regime from laminar to turbulent flow, in contributing to the observed decreases in fracture transmissivity needs to be assessed.

At the end of each suite of experiments on all four samples, tracer tests were completed at the final loading step, followed by the injection of a room temperature curing resin into

the fracture plane. The fracture plane was then sectioned, photographed and the outline of the resin filled fracture plane was digitized. The distribution parameters for the resin filled pore space in each fracture, along with the distribution of the contact areas, was determined for each sample. For the second Äspö sample, the full sample plane was mapped along a series of perpendicular profiles, spaced approximately 10 mm apart. These data were analyzed and the semi-variograms for the pore space were generated. The data were then kriged to determine the spatial distribution of the combined fracture pore space and the contact areas. In addition, the kriged data were used to generate the cell values for a 1.5 mm and a 5 mm grid spacing for the porous media model MODFLOW. Flow simulations demonstrated that using the measured pore space as input parameters with which to calculate cell hydraulic conductivities produced an excellent match between measured and computed flowrates for similar geometry and flow boundary conditions when the 1.5 mm grid values were used. Averaging the apertures over a 5 mm grid reduced the degree of fit between the measured and the computed flowrates.

A key question is how do the gas bubbles as they evolve in the fracture plane reduce the fracture transmissivity. Does the evolving gas fill the large pores or do the bubbles migrate through the pore space and eventually block the smaller pores that form the throats or so called bottle-necks in the fracture pore space? To provide a preliminary assessment of the role of the large and small apertures on the reduction of fracture transmissivity by degassing, the large apertures were selectively removed from the aperture distribution and the generated aperture or hydraulic conductivity grid until the measured degassing flowrates and computed flowrates matched the measured flowrates. To obtain a match for the second step of the degassing experiment at 10 MPa for the second Äspö sample, the overall pore space of the fracture had to be reduced, by successively removing the large apertures, to 80.5 % of the initial pore space that was used in the single phase modeling. To fit the numerical model to the measured flows at step 3 of this degassing experiment the pore space had to be reduced to 94.6% of the original pore space of the model.

To model the effects of blocking of smaller apertures, the smaller apertures were successively removed from the model and set to the minimum value. In the original model, the smallest aperture was 0.002 mm. To match model computed flows to flows measured in step 2 all apertures up to 0.100 mm had to be removed which represented a reduction to 91.9 % of the original pore space, reducing the average aperture from 0.158 mm to 0.145 mm. To fit the model to the step 3 data, apertures up to 0.074 mm were removed for a average aperture of 0.152 mm, representing 96.1 % of the original pore space.

The final set of laboratory experiments consisted of constructing replicas of the fracture surface that was used in the LSPM experiment and in the concrete sample. This replica had a very high hydraulic conductivity and a very low bubble trapping capacity. These two factors produced high fluid velocities that effectively swept the bubbles from the fracture pore space before they had an opportunity to coalesce and block the fracture pore space. The observed changes in fracture transmissivity with increasing gradients included both degassing effects and effects due to changes in the flow regime.

This suite of laboratory experiments and preliminary numerical simulations have demonstrated that degassing within fracture planes can produce significant changes in the apparent transmissivity of discrete fractures. The relative impact of degassing on fracture transmissivity is determined both by the magnitude of the fracture transmissivity, the fracture roughness or trapping capacity of the fracture plane, the type of gas present in the water phase and the percent of the gas that is dissolved in the water. In addition, the flow geometry and the resulting changes in flow regime with increasing flowrate or increasing hydraulic gradient can both mask changes in the observed fracture transmissivity and amplify these changes.

Contents

List of Figures

List of Tables

1 Introduction

1.1 Background

Experimental work in the final phase of the Stripa project showed a significant decrease in the total volume of groundwater inflow, into a 50 m length of excavated drift in the Stripa granite, in comparison to the total inflow to the first 50 m length of a ring of 100 m long boreholes (the simulated drift experiment) that outlined the perimeter of the drift (Olsson, 1992). Attempts to predict the total inflow to the ring of boreholes, using both continuum and discrete fracture numerical codes, produced results that were in close agreement with the actual measurements. However, similar attempts to predict the inflow to the drift, using the same numerical codes and the loading part of the basic empirical stress-compliance relationships for discrete fractures, produced predictions that were not in agreement with the inflow measurements. A number of different processes have been assumed in order to explain the discrepancy between the predicted and measured drift inflows. These assumed processes include the effects of degassing due to the lowering of the fluid pressures in and near the drift, resulting in two-phase flow conditions (Long et al., 1995), and reductions in permeability due to excavation induced stresses and dynamic loading during blasting for the drift excavation.

Attempts to determine which of the above two, or other, processes was the controlling process, centred on the differences between the boundary conditions during the SDE and the drift inflow measurements. The main hydraulic difference consisted of 17 m of water back pressure (hydraulic head) on the boreholes during the final drawdown step in the SDE as compared to atmospheric pressures or zero hydraulic head in the drift experiment. The groundwater in the fractured granite had high levels of dissolved gasses. Gas bubbles were observed in the outflow lines from the boreholes during the SDE. The distribution of flows from the fractures along the boreholes compared to those along the drift surface appeared to be different. The remaining 50 m sections of the D-boreholes showed a reduction in flowrates between the initial measurements at the time of the SDE and a second set of borehole measurements that were made after the drift was excavated.

If one considers that the diameter of the drift is approximately 30 times larger than the individual boreholes, rigid model concepts suggest that there should be a scale effect that should result in larger flows into the drift. However, the stresses induced by the excavation of the drift influence a much larger area or zone than the stress concentrations around each borehole. Moreover, while the diameter of the borehole is only a small fraction of the average fracture spacing, the diameter of the drift is several multiples of the average fracture spacing. Given the highly deformable nature of the fracture system, the larger drift size allows the rock blocks in the drift wall to move in response to the drift excavation and changes in the stresses around the drift. Drift convergence and or dilation is frequently observed in mining and underground excavation investigations.

The size of the drift relative to the fracture spacing and the 3-D nature of the fracture system coupled with the high stress concentrations, produced by the anisotropic stress field, will produce significant changes in the normal and shear stresses acting on the fracture planes in the drift walls. Given the stress dependent nature of fracture apertures, there is a real possibility of substantial normal and shear displacement on and along the fracture planes with resultant changes in permeability. In addition to the impact of drift induced stress concentrations on permeability, one has to consider the impact of dynamic loading during blasting, for drift excavation, on fracture permeability. Dynamic loading of fracture planes can produce a permanent reduction in fracture apertures and hence this could lead to lower fracture permeabilities that would be superimposed on other stress induced changes in fracture permeability.

Natural fractures have rough surfaces and are characterized by variable apertures within each fracture plane. Initial experiments suggest that fracture roughness, aperture variation and the range of the initial average apertures are important factors in controlling two-phase flow through discrete fractures. The distribution of apertures for a given fracture roughness is a function of the normal and shear stress acting on the fracture plane. Thus, any attempt to experimentally evaluate the effects of drift excavation on ground water inflow must recognize the coupled nature of the degassing and the coupled stress-flow properties of joints. In addition, the experimental configuration must allow for the same degrees of freedom, in terms of fracture displacement, as those expected in-situ and a close approximation of the loading events and loading pathways to which the actual drifts are exposed.

1.2 Objectives and Scope

To assess the coupled effects and relative contributions of degassing and excavation-induced fracture deformation on drift inflows, an experimental study of two-phase flow, and specifically degassing, under different stress conditions was undertaken to support the in-situ experiments at the Äspö laboratory. The first phase of this project consisted of a literature review and feasibility study supported by preliminary experiments on fabricated fractures that are characterized by uniform roughness (Gale, 1994). This phase of the overall project consisted of a detailed study of two-phase flow in a large 2 m by 2 m fabricated fracture surface and two-phase flow and degassing in two small fabricated fracture planes and in two samples of a natural fracture plane from the Äspö site. In addition, plastic replicas were constructed of one of the fabricated fractures to attempt to visualize the degassing process in a fracture with uniform roughness.

Analysis and interpretation of the experimental data were supported by detailed pore structure characterization of both the fabricated and the natural fractures and preliminary numerical simulations using a porous media model representation of the fracture pore space. The main thrust of the experimental program was to provide background data on the coupled stress-flow properties and the structure of the pathways within discrete natural and fabricated fractures in order to determine the relationship between these properties, the fracture pore structure and any observed changes in permeability induced by two-phase flow and degassing under laboratory conditions for application to

repository sites. The detailed scope and objectives for each component of this program are given in each of the following chapters in this report.

1.3 Basic Concepts

Multiphase flow consisting of the movement of two or more fluids (including gases) through fractures and fractured rocks is a complex process involving a number of basic concepts. These include the basic concepts of (1) Saturation Ratio, (2) Interfacial Tension and Wettability, (3) Capillary Pressure, (4) Capillary Pressure Curves and Hysteresis, and (5) Relative Permeability. These concepts have been discussed by a number of authors and are reviewed with respect to fracture systems in Gale (1994). In addition to the above concepts, two related parameters need to be considered when interpreting changes in fracture transmissivity that are observed with increasing drawdown in a borehole in a saturated fracture system. These parameters are the angle between the wellbore and the fracture plane and the change in fluid velocity as the fluid converges towards the borehole.

Given the variation in fracture orientations that exist in any fractured rock mass, and the range in wellbore directions used to investigate the flow properties of these rock masses, it is reasonable to assume that any given wellbore will have the possibility of intersecting fracture planes at all angles from 0 to 90 degrees. Thus in drilling through any given part of the rock mass, there will be fractures that range from those that are oriented parallel to, and those that are oriented perpendicular to, the wellbore axis. When the wellbore is oriented perpendicular to the fracture plane, the flow geometry during withdrawal will be essentially radial and will exhibit a typical logarithmic change in pressure or head as one approaches the wellbore. By contrast, fractures oriented parallel to the wellbore will exhibit a typical linear change in pressure or head around the wellbore.

Under radial flow conditions, the fluid moves through an ever decreasing area of the reservoir or fracture plane as it converges on the wellbore. As the area through which the volume of flow is passing decreases the fluid velocity increases. Under linear flow geometry, the area remains the same over the entire flowpath (except for the changes due to spatial structure of the porespace) and hence the fluid velocity remains the same in the fracture plane if the aperture is constant. Plots of friction factor or head loss versus Reynolds number, or fluid velocity, for flow in rough pipes (Figure 1-1; Lomize, 1951; in Romm, 1966), show the typical head loss with increasing fluid velocity and the head loss at the transition from laminar to turbulent flow at critical velocities. These plots also show that with increasing roughness, the transition from laminar to turbulent flow takes places at much lower fluid velocities in discrete fractures and that this transition zone covers a much greater range of fluid velocities.

The theoretical effects of the fracture-wellbore intersection angle on the drawdown or pressure distributions around the wellbore, assuming a constant flowrate, are shown for five different intersection angles, including one set of experimental data, in Figure 1-2. These head distributions have been calculated using the basic equations for laminar and turbulent flow in a single fracture as outlined in Rissler (1978) for both linear and radial

flow with approximations to calculate the head distributions for the non-orthogonal fracture intersections. For an intersection angle of 90 degrees or less, the head loss or drawdown, when plotted on a semi-log plot would be a straight line if laminar flow conditions existed over the entire flowpath. Deviations from a straight line in Figure 1-2 are due to the onset of turbulence as the fluid converges and the velocity increases as it moves towards the wellbore. The additional head loss due to turbulent flow can be estimated by fitting a line to the straight line part of each curve on the right-hand side of the figure and extrapolating this straight line to intersect the edge of the wellbore. The difference between the drawdown indicated by the intersection of this line with the wellbore and the actual calculated drawdown is the head loss or skin effect due to turbulence or turbulent flow.

Figure 1-2 also shows the experimental data from a large physical fracture model study that was conducted by Atkinson et al. (1994). In this physical model, the fracture was oriented perpendicular to the wellbore, ie an intersection angle of 90 degrees. Figure 1-2 shows that there is very close agreement between the experimental and the theoretical distance versus drawdown curves. Based on these drawdown curves, it is clear that the drawdown or head loss required to conduct a given volume of fluid into the borehole under linear flow conditions, ie when the fracture is parallel to the borehole, is only a small fraction of the drawdown required to move fluid into the borehole under radial flow conditions. In addition, for the same flowrate the linear flow case shows no evidence of head loss due to turbulent flow while the radial flow case shows significant additional drawdown or head loss due to turbulent flow.

To demonstrate the effects of fracture orientation on flowrate to a wellbore that is intersected by a single fracture plane, the geometry of the large scale physical model used in this study was simulated using a 3-D finite difference numerical model as discussed in Chapter 2. This model is 1.61 m wide by 1.88 m in length. The fracture aperture was set at 1.343 mm, which is approximately equal to the fracture aperture under 0.2 MPa of normal stress. Six different fracture intersection angles were simulated, from perpendicular to the wellbore axis to approximately parallel to the wellbore over about 1 m of length. Figure 1-3 shows how the flowrate through this fracture, under a gradient of 9.5 m, varies as a function of intersection angle. As the intersection angle falls below 30 degrees, there is a dramatic threefold increase in the flowrate.

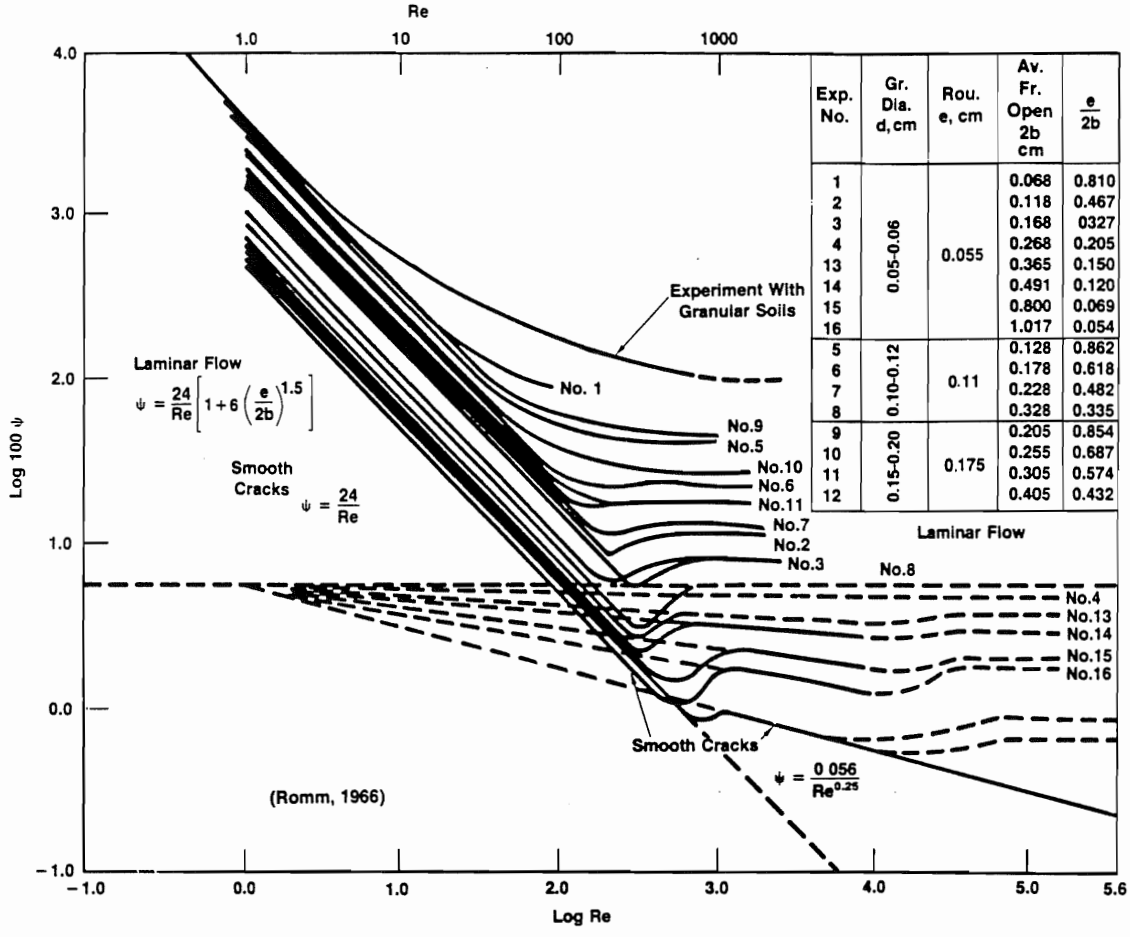

Figure 1-1. Effects of fluid velocity or Reynolds number on friction or head loss (after Romm, 1966).

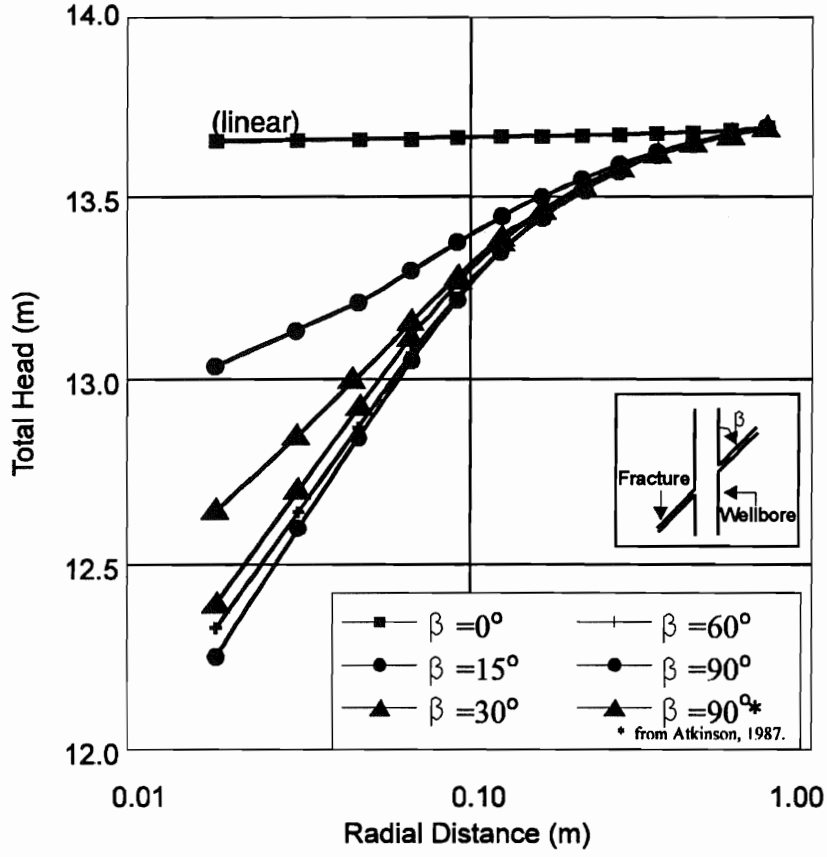

Figure 1-2. Comparison of head loss in flow through discrete fractures with experimental data.

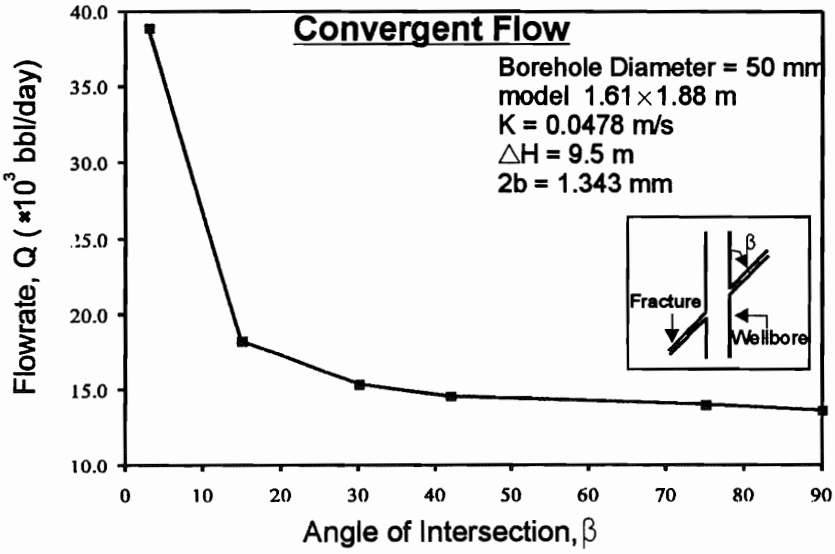

Figure 1-3. Changes in flowrate as a function of fracture intersection angle.

2 Large Scale Model Experiments

2.1 Description of Large Scale Physical Model

A large scale physical model (LSPM) test facility, that included a fabricated fracture sample measuring approximately 2 m x 2 m in plan view with flow dimensions of 1.61 m by 1.88 m, was constructed in order to study how the angle between the wellbore and the fracture plane affects flowrate versus drawdown relationships, as a function of normal stress, for both single and two phase flow in discrete fractures. Flow experiments for this study were conducted while the fracture plane was subjected to a range of effective normal stresses, up to approximately 1.0 MPa, and under both linear and near radial flow geometry.

The overall two-phase flow part of this research program was designed to examine the gas saturations and hydraulic conditions that result in gas bubbles forming both a discontinuous phase (degassing) and a continuous phase in the fracture plane. The effect of the discontinuous gas phase on the relative permeability of the fracture plane to water and the role of the pressure gradient in the movement of the continuous gas phase in fractures, with a range of relative roughness and apertures produced by changing the normal stress, have been examined.

Details of the large scale physical model construction are given in Gale (1994) and Gale et al. (1996) and only a brief summary will be given in this report. The reaction frame for the physical model consists of five rings, each fabricated from four steel beams (Figure 2-1; Note the approximate 2 m dimensions of the sample for scale.). Loads are applied using stainless steel flatjacks. This flatjack system is used to provide loading on top and bottom of the physical model for the single fracture case in this current physical model.

The current physical model was constructed of high strength concrete (measuring approximately 2 m x 2 m x 2 m). The fracture surface was created using a woven geotextile (that was removed after the concrete cured) to ensure the same degree of small scale surface roughness over the entire fracture plane. This small scale roughness closely resembles natural fractures in both mechanical, surface roughness and flow properties. An internal support frame was used to support, during construction, the internal sensors, which included the internal manometer ports, strain gauges, thermocouples, resistivity electrodes as well as the copper tubes for cooling during concrete curing, wellbore guides, inserts for sample lifting, gas injection ports and the flow reservoirs around the outside edge of the model. These flow reservoirs were used to control the flow and fluid pressure boundary conditions during testing.

After the concrete had hardened for several weeks, the sides of the frame and the mould were removed and an inclined borehole, forming a 42 degree angle with the fracture

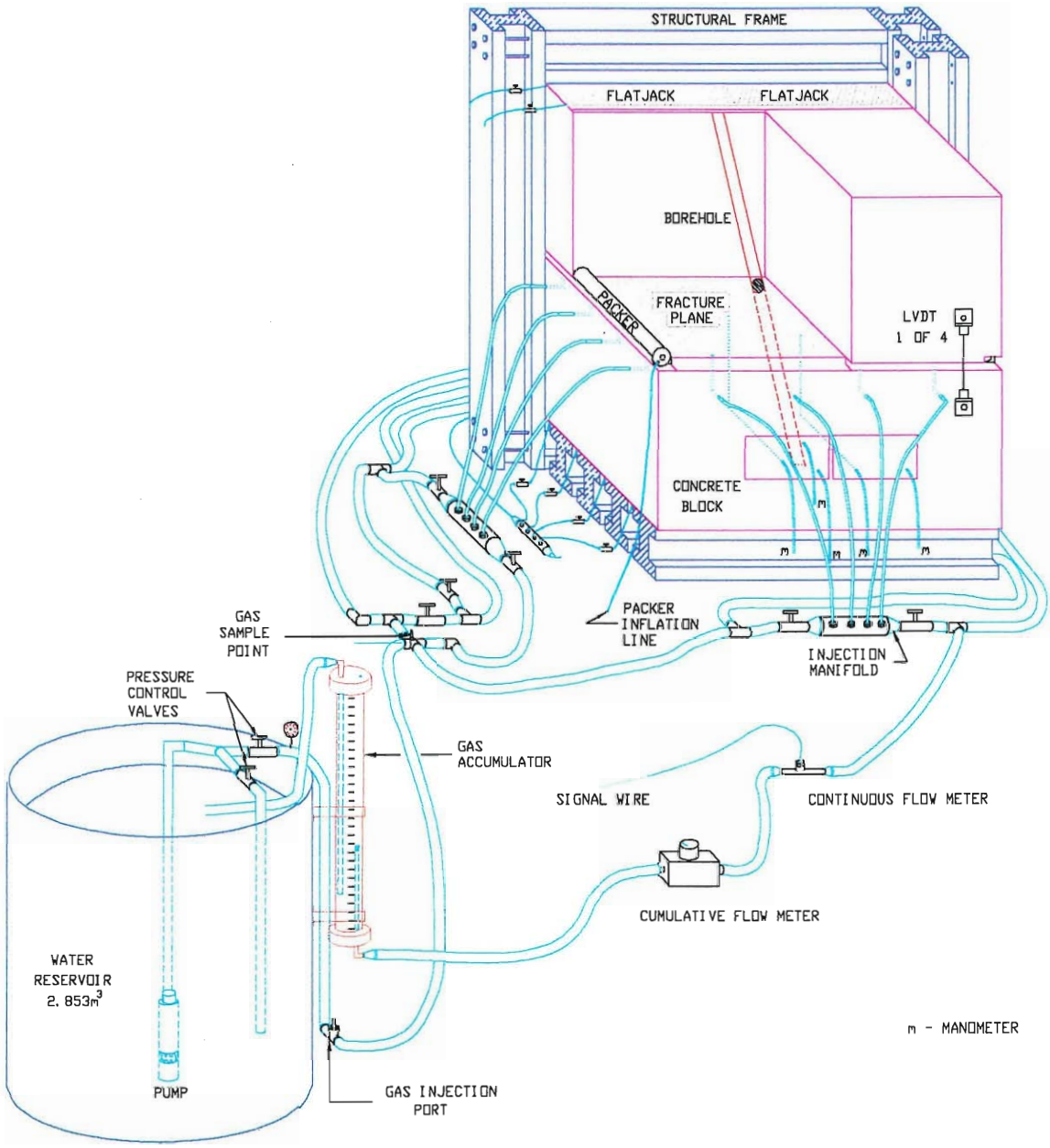

Figure 2–1. Schematic of Large Scale Physical Model (LSPM) and flow test equipment.

plane, was drilled through the center of the model to intersect the mid-point of the fracture plane, creating an elliptical opening in the middle of the fracture plane. Fracture displacements due to uniaxial loading of the model or in response to the pressure heads, generated during flow tests within the fracture plane, were monitored using four external Linear Voltage Differential Transducers (LVDT) that were installed across the fracture plane (Figure 2-1).

Figure 2-2 shows a vertical view of the fracture surface on top of the bottom half of the physical model after the concrete had cured, the two halves had been wedged apart, the geotextile removed and the top half of the model had been lifted and moved parallel to the lower block to provide access to the manometer, gas and resistivity ports. This photograph shows the inclined borehole penetrating the lower block and the manometer ports that were opened in the lower block. The eight lines of manometer ports that were built into the model are shown in Figure 2-3. Each array of manometers originates at the borehole and the different lines are labeled alphabetical starting with A at the three o'clock position and moving in a clockwise direction to H in the upper right hand quadrant. The model is oriented with array G on the north side and array C on the south side. Figure 2-4 shows a side view of the top and bottom blocks after they had been separated and prior to final assembly.

2.2 Single and Two Phase Flow Test Procedures

The model was configured to provide flow between any two of the outside edges of the model or between any one, two, three or all four of the outside edges and the central borehole in the model. This configuration was designed to permit either linear, convergent or divergent flow geometry. The existing borehole in the large scale physical model is 50 mm in diameter. Figure 2-5 shows the normal stress loading path and the flow tests that were conducted on this physical model with this borehole size.

Water was supplied to the fracture plane through 16, 15.9 mm OD, water injection ports that are located around the outside edge of the fracture plane (Figure 2-3). The water injection ports were connected to the flow injection system which consisted of a 2.85 cubic metre steel reservoir, a submersible pump, 50 mm flow lines, PVC manifolds and 50 mm gate valves (Figure 2-1). The flowrates were measured using one or all three of 1) an in-line electronic flowmeter on the discharge line, 2) a cumulative flowmeter also on the discharge line and 3) manual measurements at the end of the return line. Flowrate was controlled using the two 50 mm gate valves on the main line from the pump, one to control the discharge directly back to the reservoir and the second to control the flow to the LSPM. By regulating these valves the desired flowrate or boundary pressure could be obtained. The upper 200 mm of the 42.5° borehole was sleeved, sealed, valved and connected to the flow system via the 50 mm flow lines.

Discharge water from the flow tests was re-circulated back to the water reservoir through an elevated constant head tank, that was used to maintain a back pressure on the model during testing. The flow system was capable of flowing at rates between 1 to 50 Lpm for all three flow configurations. For convergent flow, water was injected through

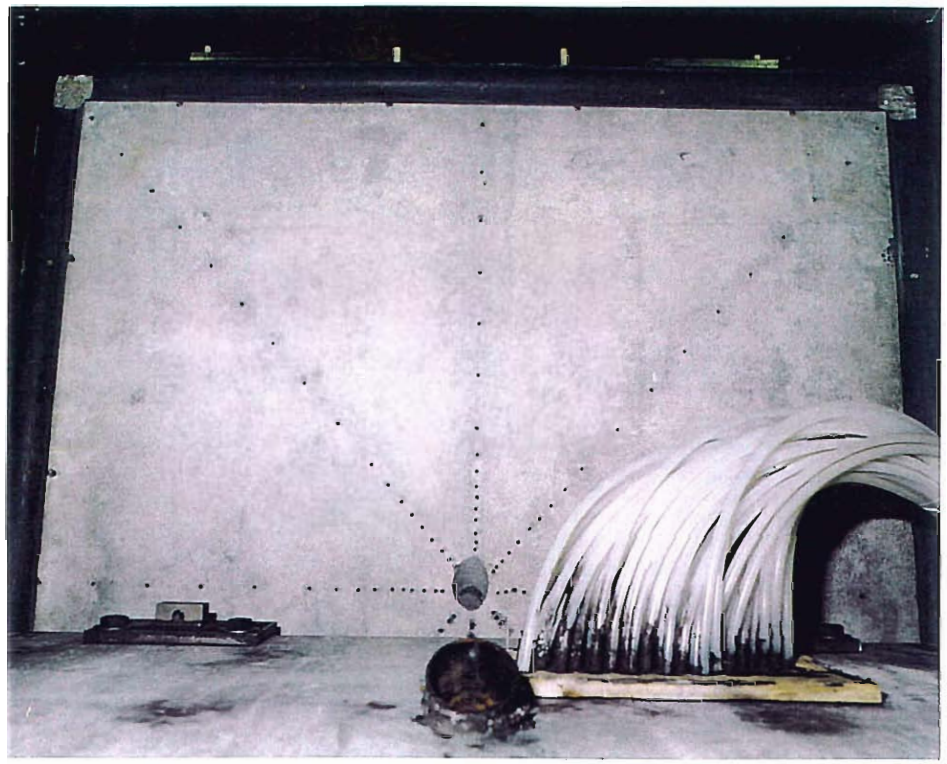

Figure 2-2. Photograph of fracture surface and 50mm borehole.

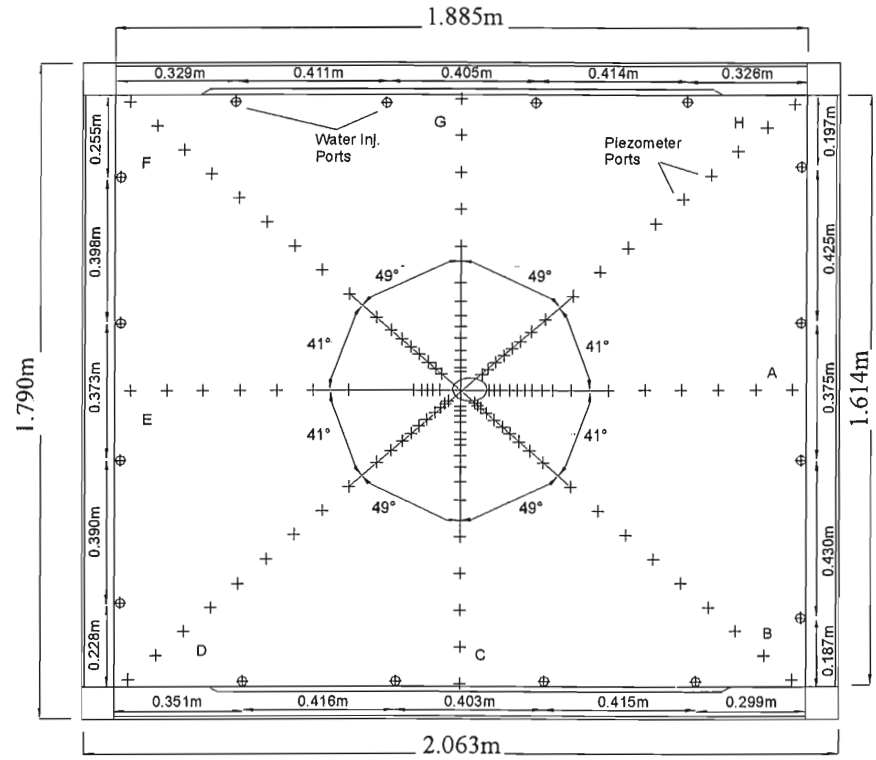

Figure 2-3. Diagram of fracture surface and manometer distribution.

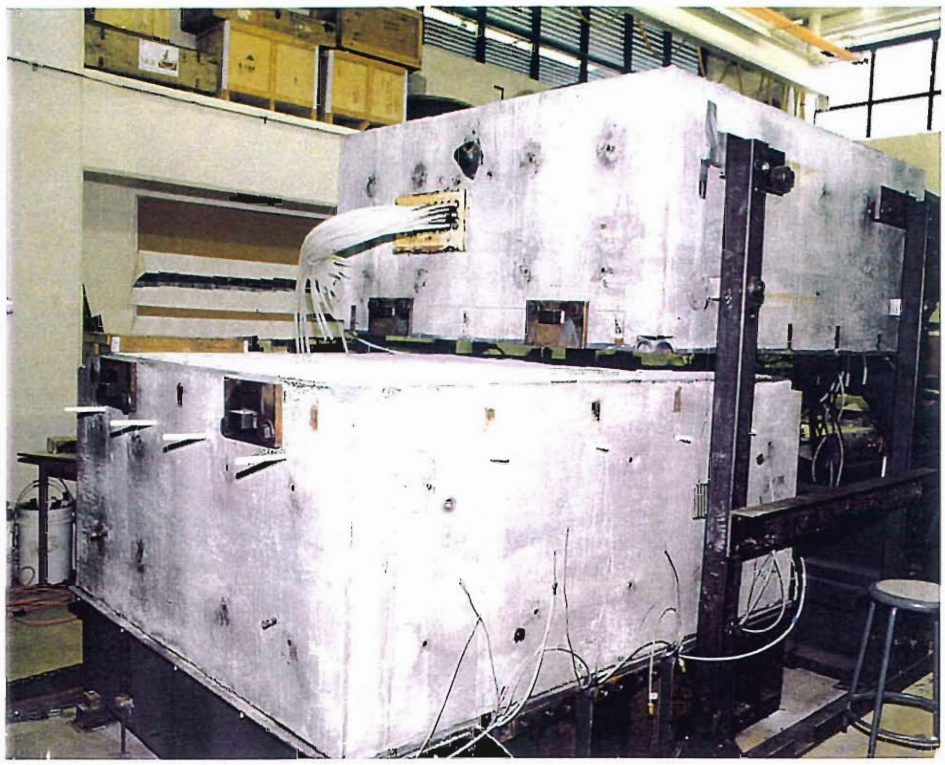

Figure 2-4. Side view showing top part of LSPM suspended above the bottom block. Note size of block for scale.

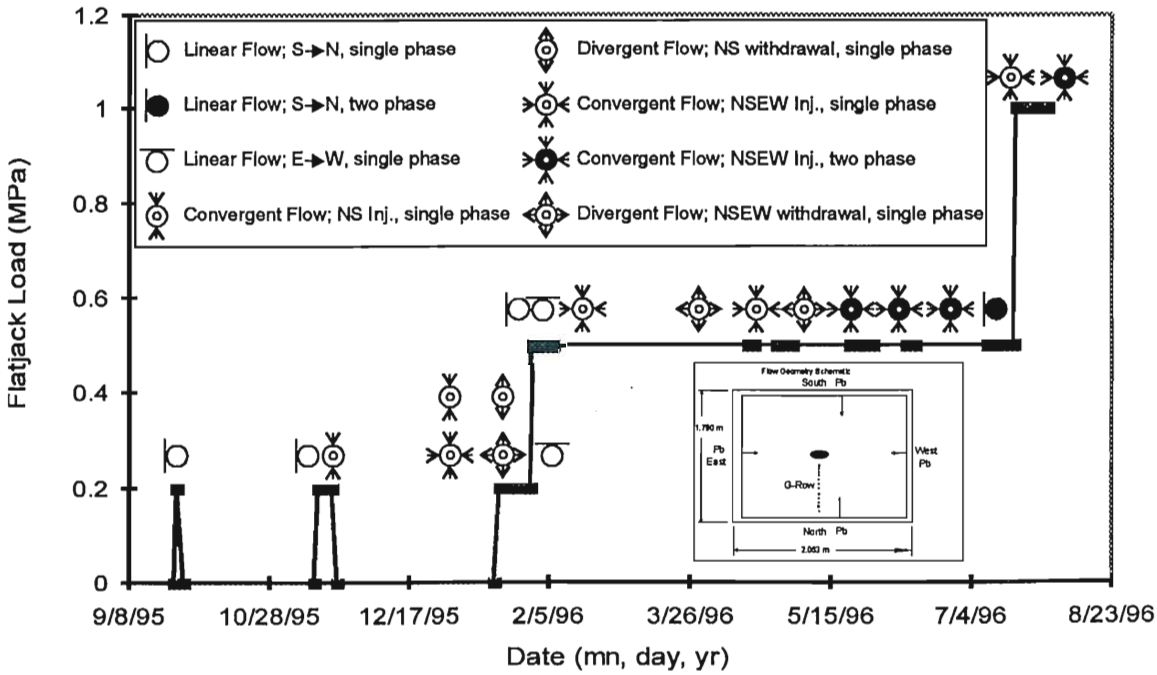

Figure 2-5. Schematic showing the loading and flow test history conducted on the Large Scale Physical Model.

two and/or all four sides of the model and discharged through the borehole, simulating the pumping of a fractured reservoir. For divergent flow, water was injected into the borehole and discharged through two and/or all four sides, simulating an injection test. Linear flow tests consisted of flowing water across the fracture from one side to the other in any desired combination. Linear flow tests were used to calculate the fracture aperture of the model, for given uniaxial loads, in order to calibrate the numerical model.

Figure 2-1 shows the large water storage tank in the foreground, the test frame and physical model in the background. A clear plexiglass tank (gas accumulator), approximately 0.25 m in diameter and 2 m in height, was attached to the water tank to measure the amount of free gas in the water at the outflow end of the flow circuit. The level of water in the plexiglass tank was set at a specified level, near the top of the tank, at the beginning of each test. Under steady state, single phase, flow conditions, the level of water in the tank will remain essentially constant (except for minor variations due to changes in flowrate) since the gas pressure will be sufficient to maintain flow out of the large diameter discharge line at the top of the plexiglass tank. During two phase flow, the diffuser over the inlet tube at the bottom of the tank ensures that most of the gas, at a bubble pressure of greater than the back pressure on the plexiglass tank, in the water nucleates to form bubbles and rises to add to the gas in the space at the top of the water tank. By measuring the height of the water in the tank, it is possible to determine the gas pressure above the water and from this obtain an estimate of the volume of gas that was released from the water that had moved through the fracture plane.

2.3 Effects of Flow Geometry and Gradient on Measured Flowrates and Fracture Transmissivities

The first step in assessing the impact of a gas phase on fracture transmissivity was to establish the pattern of hydraulic head or pressure head (pressure head can be used since the fracture plane was essentially horizontal and the manometers measure pressure heads only) over the fracture plane under different flow and hydraulic head boundary conditions. Figure 2-6 shows a contour map of pressure heads under linear flow conditions, ie. flow is from one side of the physical model to the other side. This contour map was created by kriging the pressure heads from all of the measurable manometers in the fracture plane under steady state flow conditions. The approximate planar nature of the pressure head field, for these effective stress conditions, suggests that the fracture aperture, while characterized by small scale roughness, is relatively uniform over the entire fracture plane. However, increasing the fluid pressures relative to the total normal stress, produces a change in fracture aperture, by hydraulic jacking, which is reflected in a distinct break in the hydraulic head profile in the direction of flow. Similarly, Figure 2-7 shows the distribution of pressure heads for convergent flow from the north and south outside boundaries to the central borehole. This contour map shows the very steep hydraulic gradients that are developed around the wellbore during convergent flow. With this increase in hydraulic gradient, there is a proportional change in the fluid velocity, increasing the frictional head loss around the well bore.

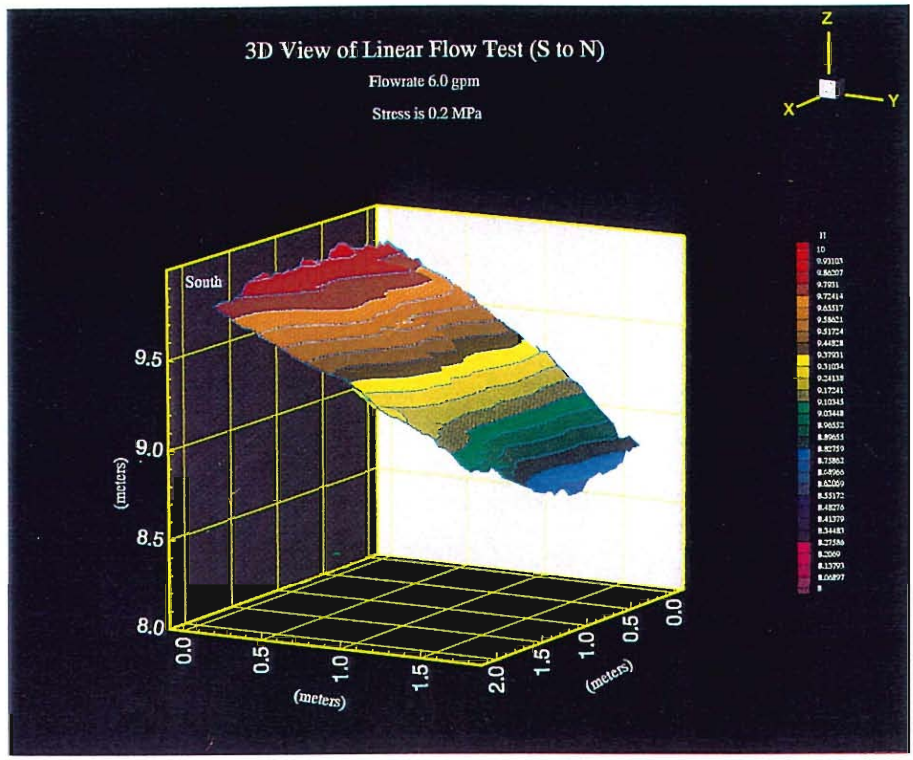

Figure 2-6. Three dimensional view of the distribution of kriged pressure heads over the LSPM fracture plane under linear flow conditions.

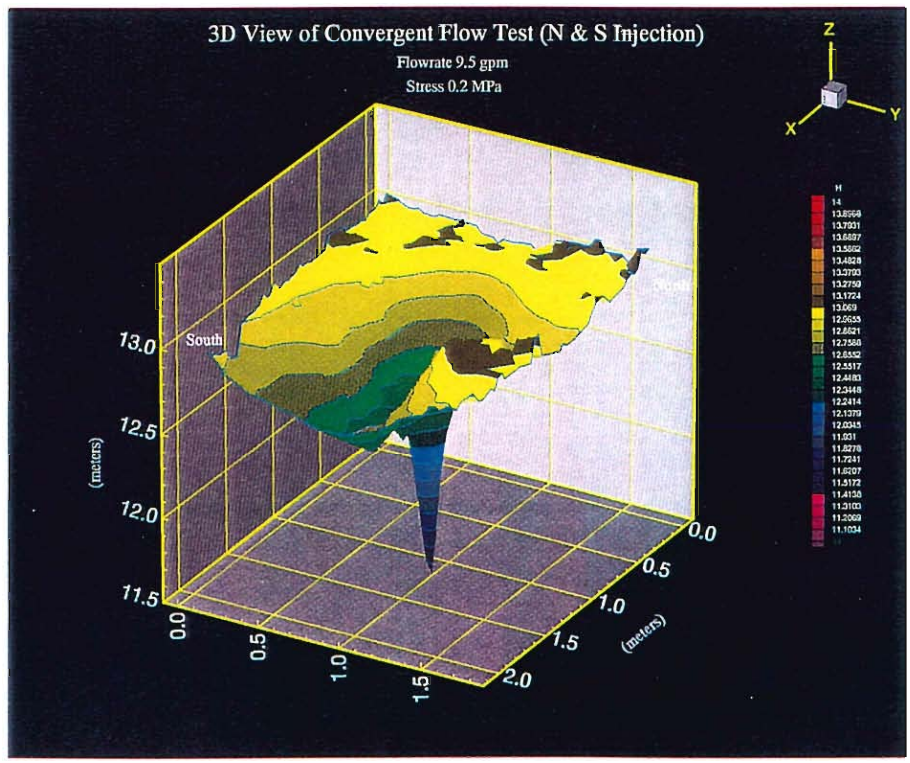

Figure 2-7. Three dimensional view of the distribution of kriged pressure heads over the fracture plane under convergent flow conditions.

The dashed or broken lines in Figures 2-8, 2-9 and 2-10 show the measured pressure heads along the G row of manometers for convergent flow for three different normal stress conditions, 0.2 MPa, 0.5 MPa, and 1.0 MPa, for four different flowrates that ranged from approximately 4 L/min to approximately 45 L/min. The measured steady state flowrates and the hydraulic heads applied on the boundary are shown on each plot. Under laminar flow conditions, the hydraulic heads along a given radial direction will plot as a straight line on a semi-log plot of hydraulic head versus radial distance for purely radial convergent flow in an isotropic medium. For these three sets of experimental data, the plots of pressure head all show a similar pattern in which the pressure heads for the low flowrates are essential a straight line but with increasing flowrate the plot of pressure heads versus distance becomes increasingly non-linear suggesting the onset of turbulence.

The additional head loss due to the onset of turbulence could be larger than the observed loss because the assumed increase in fracture aperture due to the jacking forces, produced by the higher fluid pressures, would offset the head loss in the outer sections of the fracture plane. This jacking can be inferred from the sudden increase in gradient at approximately 0.1 m from the edge of the well bore. The higher gradients that were measured within 0.1 m of the well bore, indicate an apparent decrease in the fracture transmissivity under convergent flow and with increasing flowrates.

2.4 Comparison of Measured and Computed Single Phase Fracture Transmissivities

In order to evaluate the changes in measured fracture transmissivities, a simple single phase porous media model of the LSPM was constructed using Visual MODFLOW. This numerical model consists of three, 10 mm thick, layers; the second or middle layer represents the fracture plane. The outside dimensions of the numerical model are 2.20 m x 2.00 m. A 20 mm grid or mesh (Figure 2-11) was superimposed on the surface of the fracture plane, producing 110 columns by 100 rows. Inactive or no flow cells, shown as a dark band in Figure 2-11, border the model leaving an active flow area of 1.61 m x 1.88 m which matches the flow area of the LSPM. The mesh was subdivided (Figure 2-11) to produce a 10 mm grid over the center 400 mm in both the north-south and east-west directions, adding an additional 20 rows and 20 columns to the mesh. For convergent flow modeling, the mesh was further refined around the borehole to produce a 5 mm grid (Figure 2-11b). The borehole was created by using inactive cells to define the shape and location of the physical model borehole, with a ring of constant head cells forming the edge of the borehole. To calculate the flowrate through the fracture plane, the flux through a row or column perpendicular to the direction of flow was computed by MODFLOW. For convergent flow the flux through a ring of cells around the borehole was computed using the zone budget option in MODFLOW.

The experimental head values from the manometer readings in the large scale physical model were used to calibrate the numerical model. These data were entered as observation well data in the Visual MODFLOW model (Figure 2-11b) at the measured manometer locations.

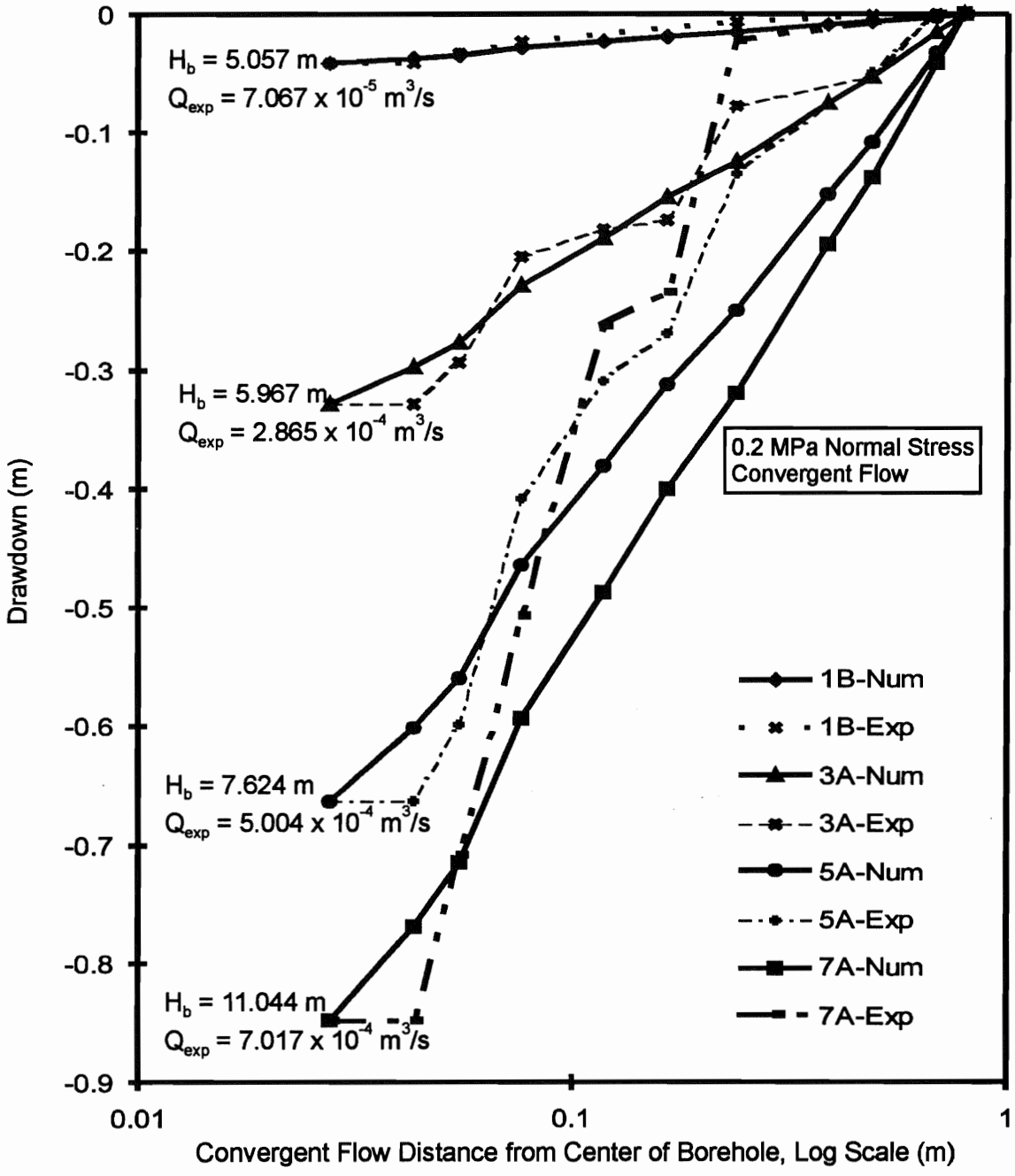

Figure 2-8. Comparison of model and experimental plots of drawdown along the G row of manometers under convergent flow at 0.2 MPa normal stress. Large scale physical model (1.61 m x 1.88 m) with 50 mm diameter borehole at an intersection angle of 42 °.

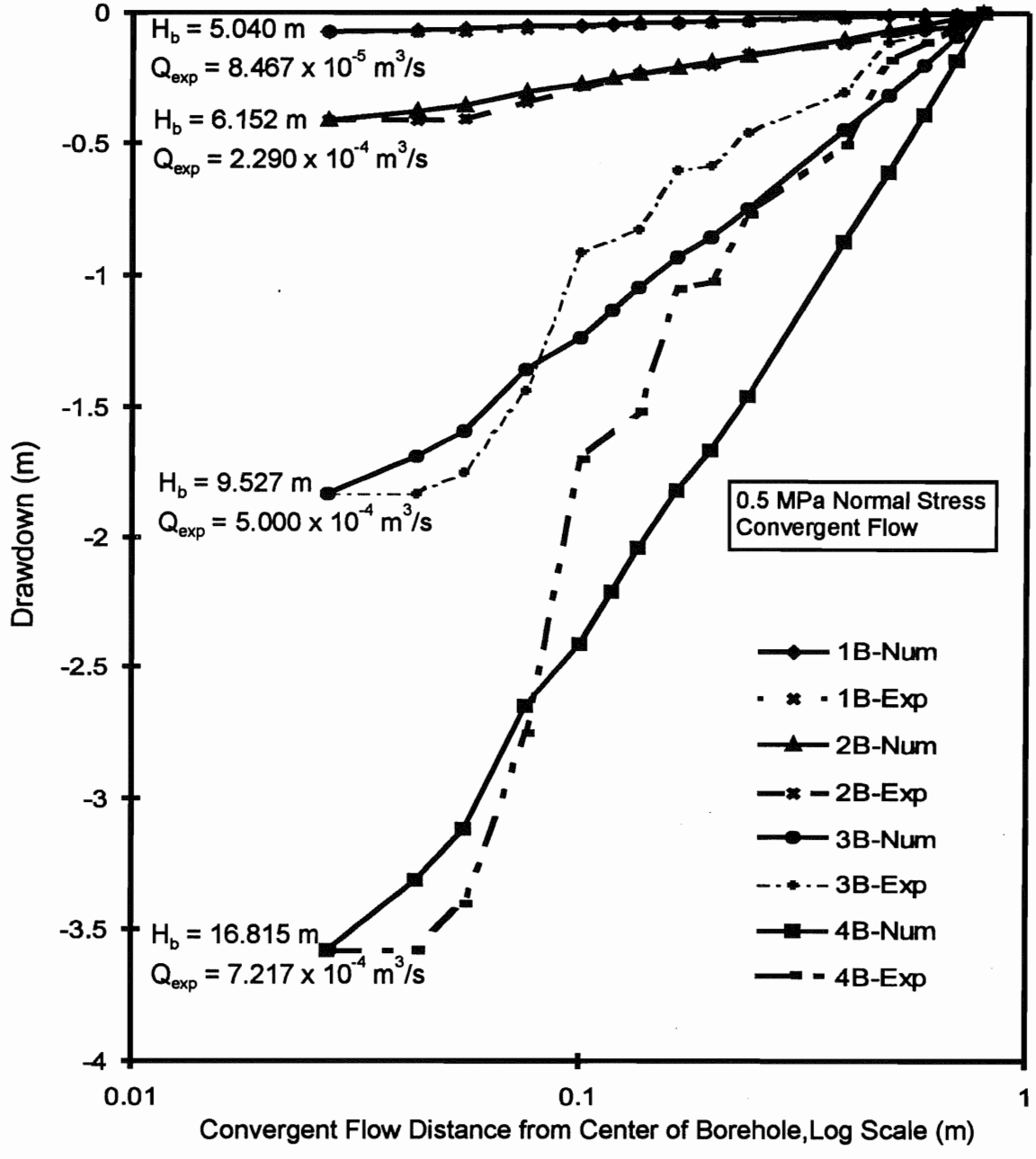

Figure 2-9. Comparison of model and experimental plots of drawdown along the G row of manometers under convergent flow at 0.5 MPa normal stress. Large scale physical model (1.61 m x 1.88 m) with 50 mm diameter borehole at an intersection angle of 42 °.

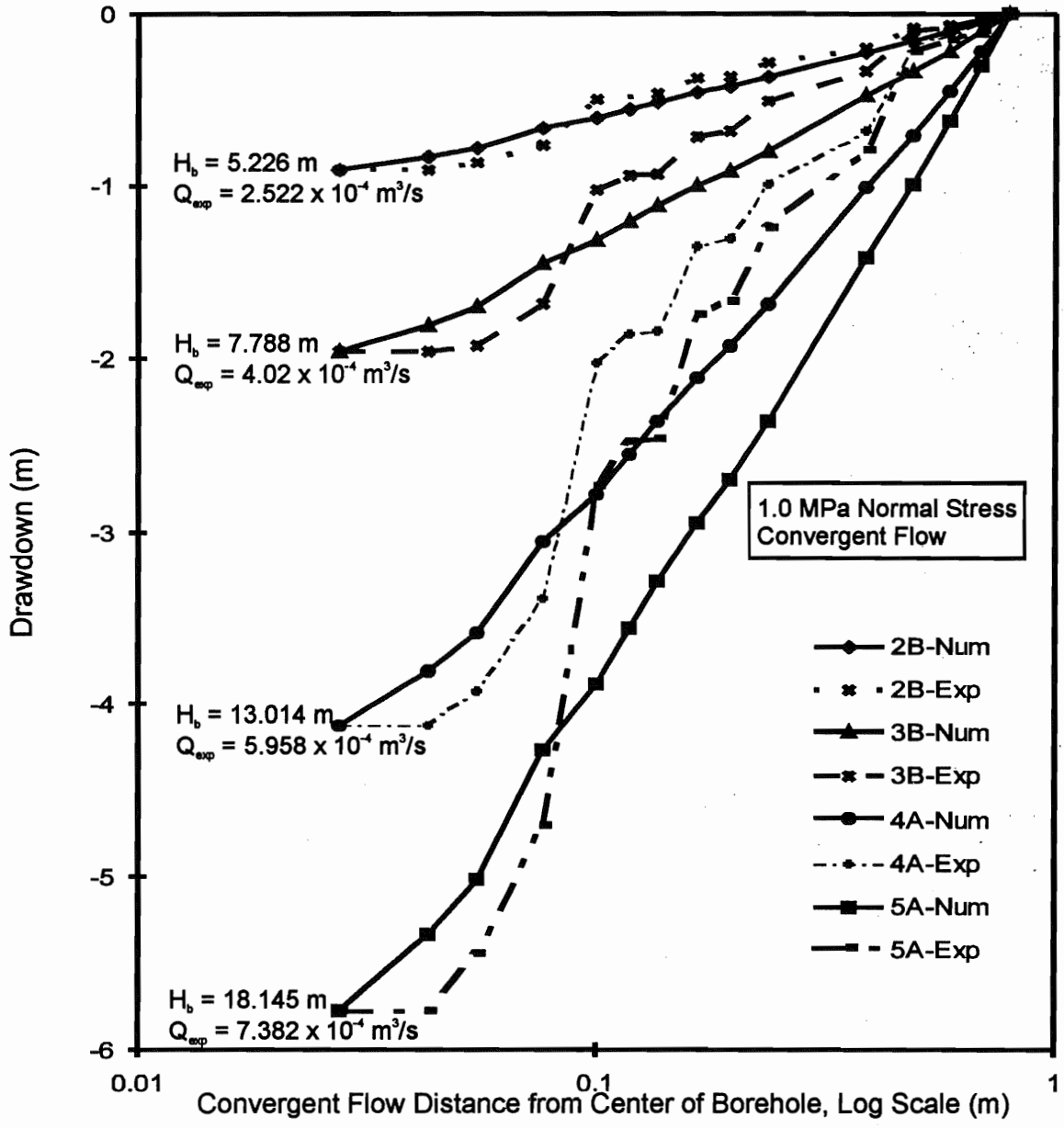

Figure 2-10. Comparison of model and experimental plots of drawdown along the G row of manometers under convergent flow at 1.0 MPa normal stress. Large scale physical model (1.61 m x 1.88 m) with 50 mm diameter borehole at an intersection angle of 42°.

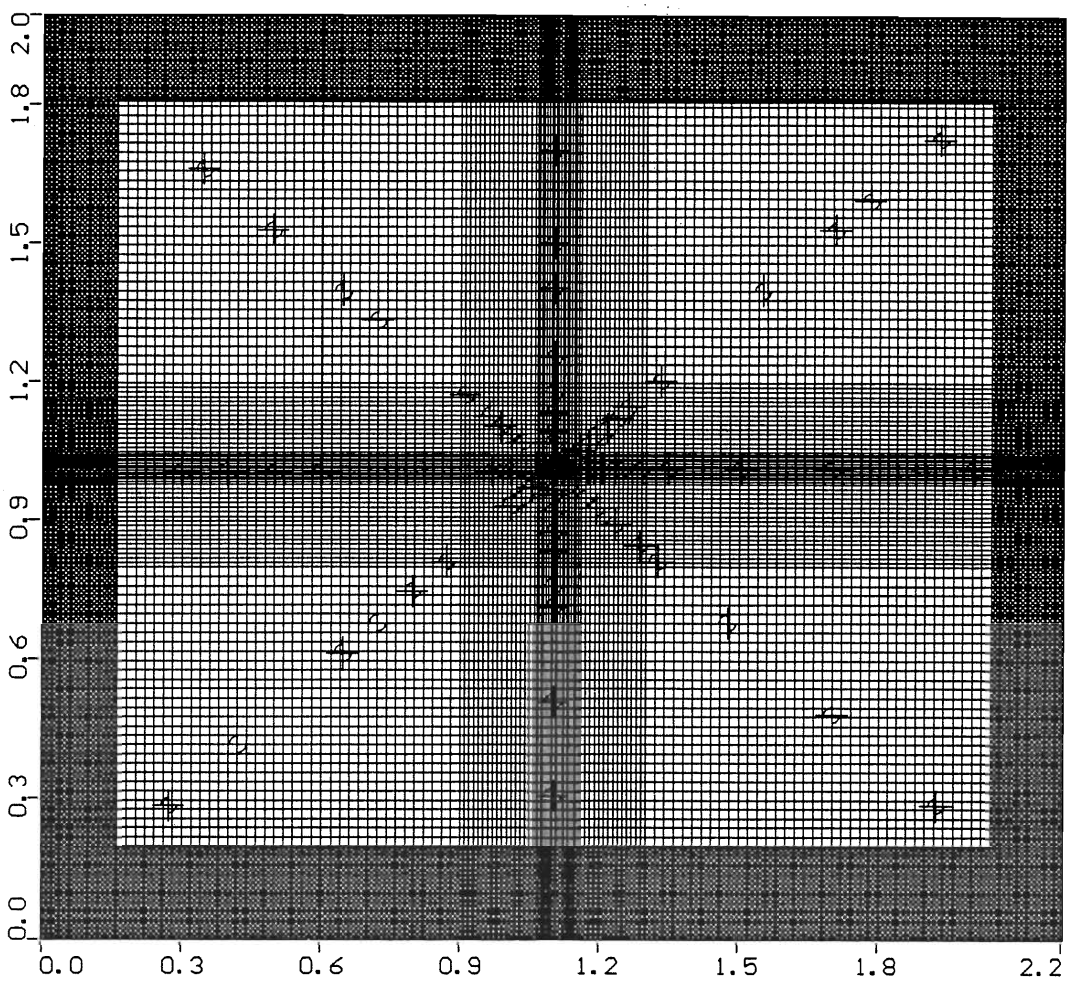

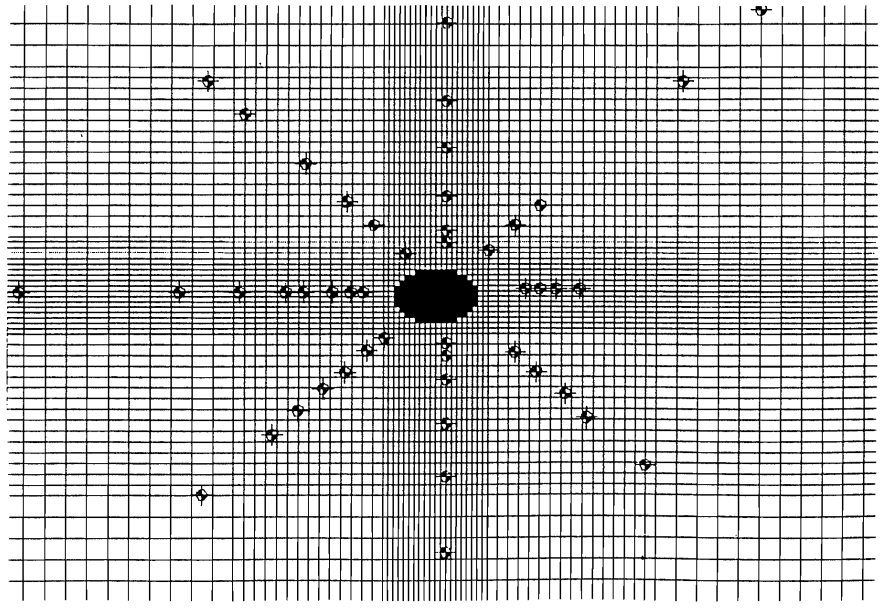

Figure 2-11. MODFLOW mesh for LSPM (a) and detailed mesh (b) around borehole for the 42 degree borehole orientation.

For convergent flow tests at 0.5 MPa and 1.0 MPa of total normal stress, pressure heads were recorded only in the north-south row of manometers. Therefore, for consistency in comparing the tests results, north-south data were used also for the experiment that was conducted with 0.2 MPa of normal stress on the fracture plane. For convergent flow the lowest value of the two manometers closest to the borehole, either G2 or C2 was used as the borehole constant head value. This borehole constant head value was used in the ring of cells on the edge of the borehole to establish the internal boundary condition.

The low flow experimental data for east-west linear flow at 0.2 MPa normal stress were used to calibrate the numerical model for the 0.2 MPa normal stress experiment. The experimental and numerical hydraulic heads were plotted as a function of the east-west distance and the steps or breaks in this curve were used to locate the sections (bands) where the hydraulic conductivity values varied. An average conductivity value was initially calculated using the lowest stable flowrates that were measured and the pressure head gradients, corresponding to these flowrates, averaged over the full flow field. Using this value and the band widths determined from the head versus distance plot, the different conductivity band values were calculated from the conductivity averaging equation for the case of flow perpendicular to the hydraulic units (Fetter, 1995). Figure 2-12 (a) shows the bands of conductivity values for 0.2 MPa normal stress. Once the east-west conductivity distribution was determined the model was run for the north-south linear flow condition again at low flow to determine any anisotropy. For the experimental and model flows to provide a reasonable match, an anisotropy of 0.68 was needed.

The model was calibrated for the 0.5 MPa normal stress experiment in the same manner as described above for 0.2 MPa normal stress experiment. Figure 2-12 (b) show the bands of hydraulic conductivity values for 0.5 MPa normal stress. The anisotropy for this loading was 0.94. The location and width of the bands at 0.2 MPa and 0.5 MPa was very similar.

For 1.0 MPa loading, only convergent flow data and only data for the north-south manometers were available, therefore the 0.5 MPa band pattern was used as the reference case in the 1.0 MPa model. The average conductivity value was calculated from the low flow experimental data, as was done for the other two stress levels. To determine the individual band conductivities at 1.0 MPa, the ratio between the conductivity values for the bands at 0.2 MPa and 0.5 MPa was used at the 1.0 MPa stress level to proportionally assign the overall average hydraulic conductivity to the individual bands.

Using the low flowrates measured for the linear flow geometry experiments as the reference for both the higher gradient tests and for the MODFLOW simulations, Figure 2-13 shows that the plot of measured flowrates versus hydraulic gradient is essentially a straight line. Using the measured heads on the model boundaries as input to the numerical model, and starting at essentially the same reference point the computed flowrates with increasing gradient are much lower than the measured flowrates at the same gradient. The difference between the measured and computed flowrates at the highest gradients for each experiment is much higher for the 0.2 MPa normal stress experiment than it is for the 0.5 MPa normal stress experiment.

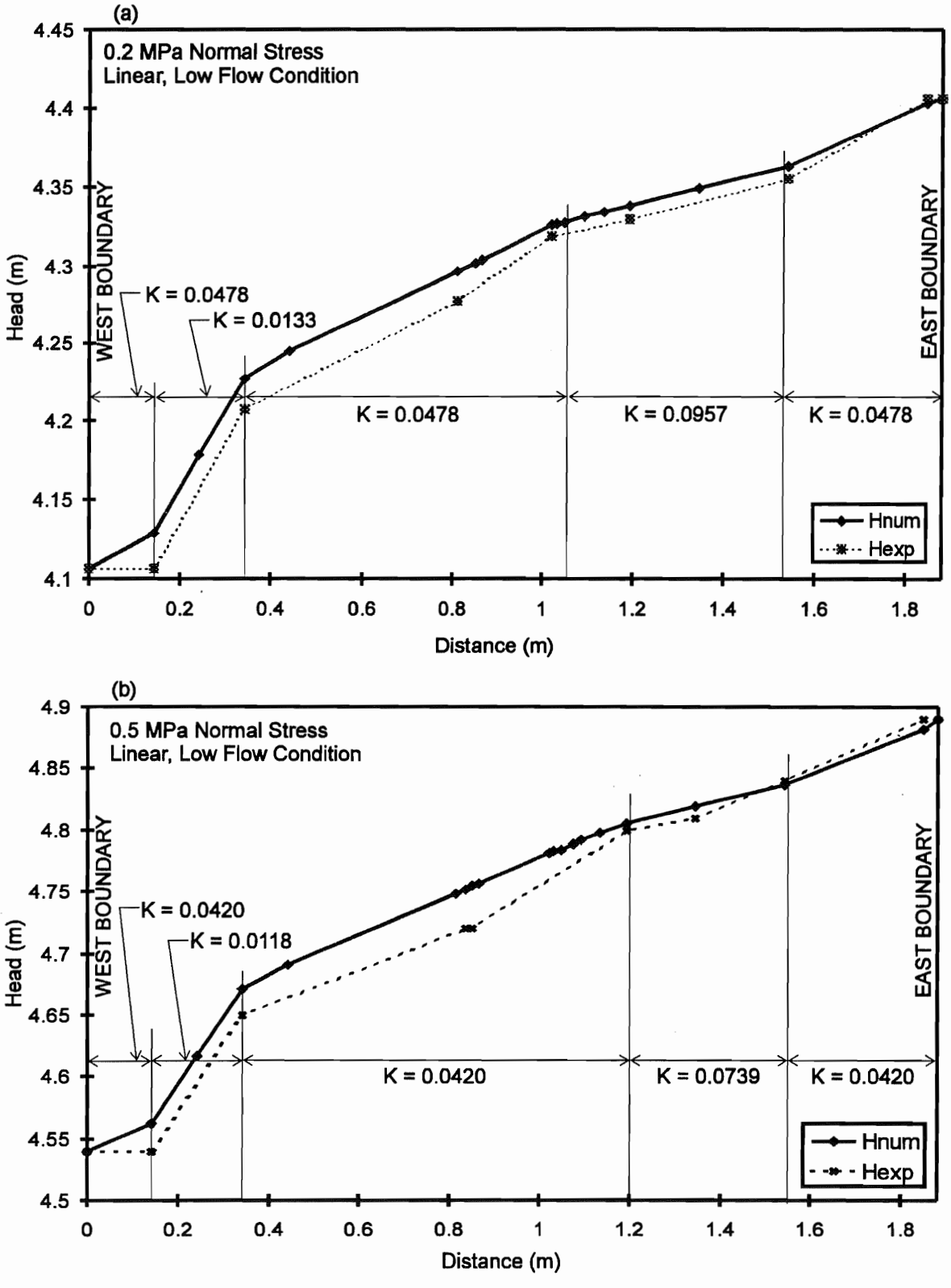

Figure 2-12. Plot of head versus distance showing bands of conductivity (K in m/s) values in the numerical model from the west to the east boundary for the linear low flow condition calibration at (a) 0.2 MPa normal stress and (b) 0.5 MPa normal stress. Large scale physical model (1.61 m x 1.88m).

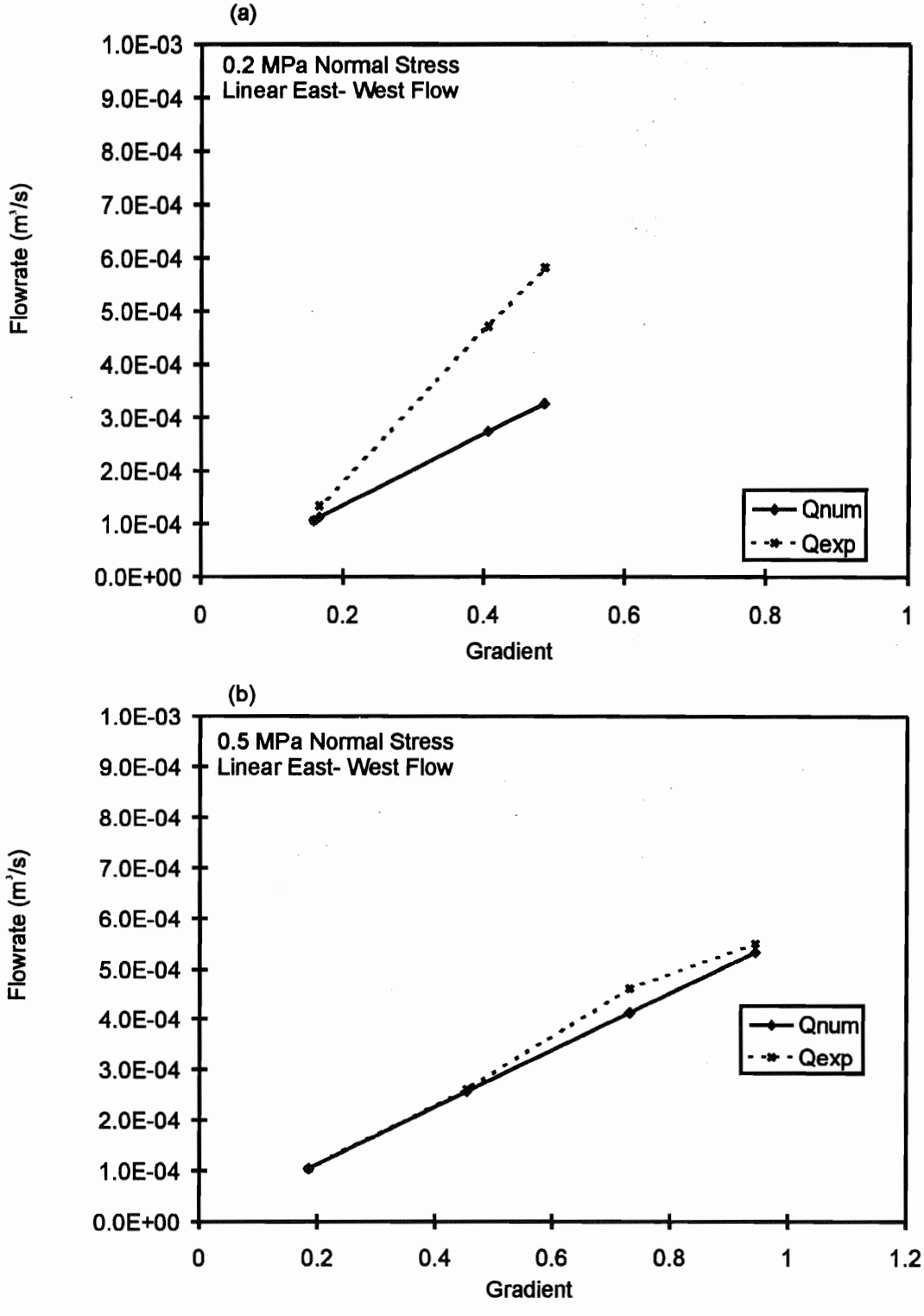

Figure 2-13. Comparison of model flowrates with experimentally measured flowrates for linear east- west flow at (a)0.2 MPa normal stress and (b) 0.5 MPa normal stress. Large scale physical model (1.61 m x 1.88 m).

Figures 2-8, 2-9 and 2-10 also include the results of the computed changes in pressure head as a function of distance from the center of the wellbore based on the Visual MODFLOW simulations of these convergent flow experiments. As expected, a laminar flow porous media model, which includes the inferred variation in hydraulic conductivity, calculates a relatively straight line on the semi-log drawdown versus distance from the well bore plot. Note that the last data point on these plots represents the edge of the borehole at 0.025 m. Comparison of the model and experimental results suggests that fracture opening around the outside edge of the model is partly offsetting the increased head loss due to increased fluid velocity as the fluid approaches the wellbore.

Figures 2-14 and 2-15 show the impact of changing the flow geometry from linear to convergent flow for the 0.2, 0.5 and the 1.0 MPa normal stress experiments. For convergent flow, the measured flowrate versus gradient data plots are more non-linear and plot below the computed flowrate versus gradient curve for the same pressure head boundary conditions and the same reference flowrate. Also, under convergent flow conditions, the difference between the computed and measured flowrates is greater at the higher normal stresses than at the lower normal stress level, which is the reverse of the pattern seen under linear flow. Based on a comparison of the measured versus computed flowrates, it is clear that there is a reduction in apparent fracture transmissivity at the higher flowrates under convergent flow and that there is a corresponding increase in apparent fracture transmissivity with increasing flowrate under linear flow conditions in the same fracture plane at the same stress levels. This pattern is clearly shown in the transmissivity versus gradient plots in Figures 2-16, 2-17 and 2-18, for both linear and convergent flow for all three stress conditions. These figures also provide the pressure head boundary conditions and the corresponding flowrate data for each experiment. The constant transmissivity value used in the numerical model is shown on each plot for easy reference. The difference between the fracture transmissivities calculated from the measured data and the computed data at the smallest gradient, reflects that a rigorous attempt was not made to calibrate the model at the low flowrates.

2.5 Effects of Two Phase Flow on Measured Fracture Transmissivities

Once the single phase fracture transmissivities had been measured for both linear and convergent flow boundary conditions at the three main stress levels, a series of preliminary two phase flow experiments were conducted. These initial two-phase flow experiments consisted of injecting nitrogen gas at relatively high flowrates into one or more (up to four, spaced approximately 10 cm apart) gas injection ports that were located in the upper block of the sample around the outside edge of the model and approximately 4 cm inside of the water injection ports shown in Figure 2-3. These gas injection ports were designed to provide a continuous flow of nitrogen through the fracture plane. The pressure used to inject the gas was just sufficient to overcome the entry pressures in the saturated fracture plane and produce a continuous gas stream through one or more of the gas injection ports. However, even with the relatively uniform roughness of the fracture surface, each port is characterized by a slightly

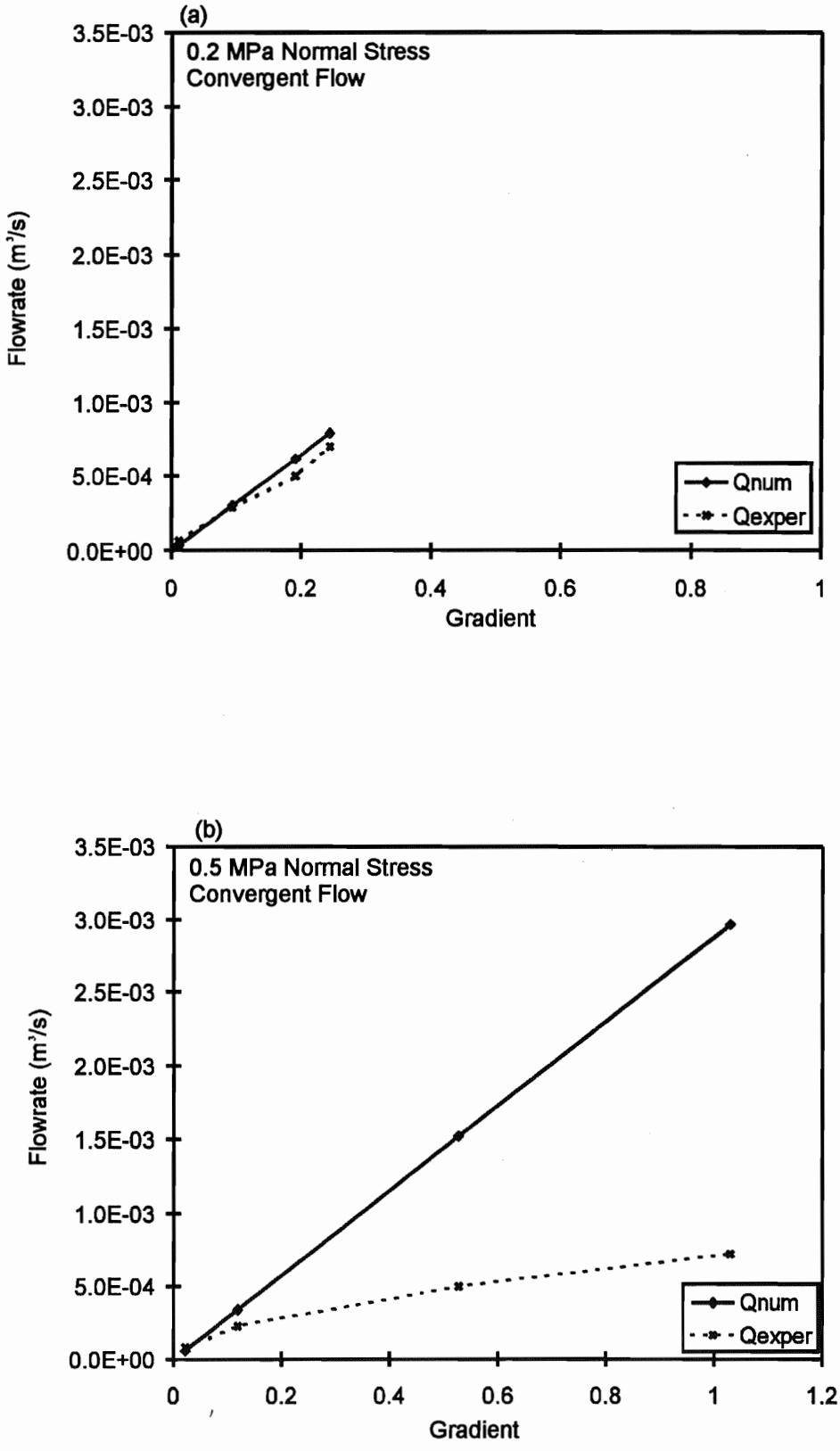

Figure 2-14. Comparison of model flowrates with experimentally measured flowrates for convergent flow at (a) 0.2 MPa normal stress and (b) 0.5 MPa normal stress. Large scale physical model (1.61 m x 1.88 m) with 50 mm diameter borehole at anintersection angle of 42 °.

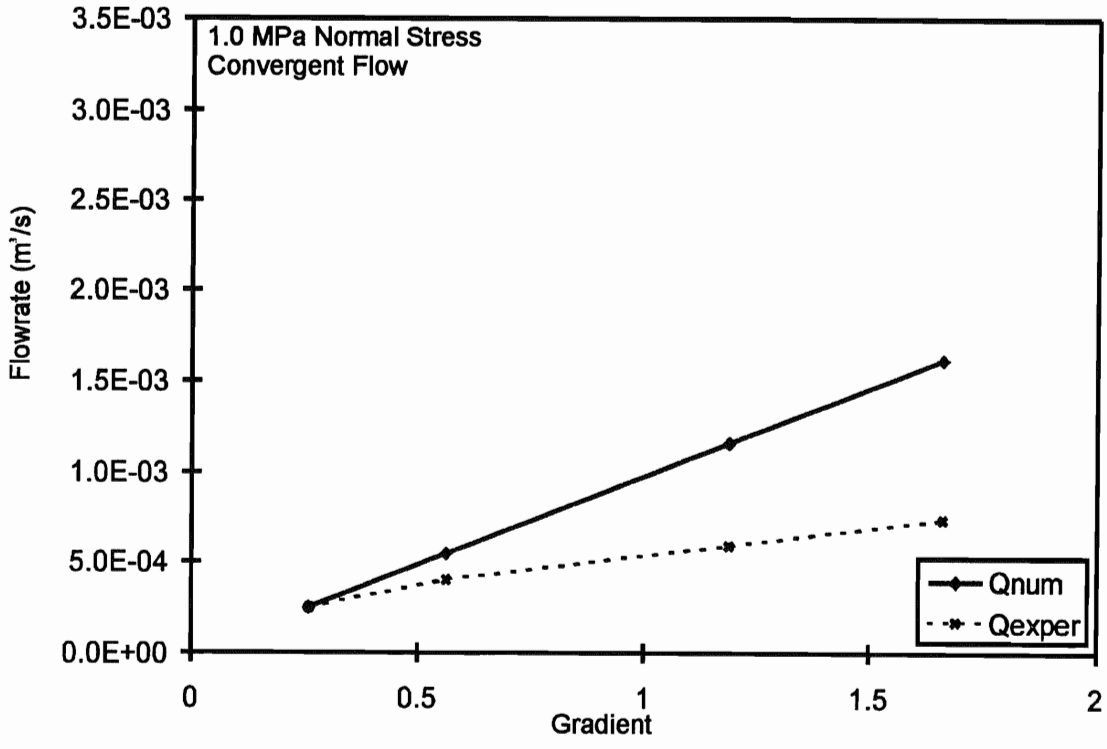

Figure 2-15. Comparison of model flowrates with experimentally measured flowrates for convergent flow at 1.0 MPa normal stress. Large scale physical model (1.61 m x 1.88 m) with 50 mm borehole at an intersection angle of 42 °.

different entry pressure. Thus, while a constant gas pressure was applied to a number of ports, the flowrate of the gas from each port was very variable and at times a port would stop accepting gas for a short period of time. However, even with this uneven distribution of the nitrogen gas injection flowrates, the water flow in the fracture plane when gas was being injected was reduced by 40% to 60% of the flowrates that were measured during the single phase experiments. Volumes of gas flow, not corrected for changes in the water column in the plexiglass tank, measured as a separate gas phase were generally about a factor of three greater than the final measured water flowrates during these initial experiments.

In a second set of two phase flow experiments under linear flow geometry, a constant gas pressure was applied to all fifteen gas ports along the south side of the model (the inflow side) and both gas and water were withdrawn from the north side of the model. In this experiment, a higher gas pressure (equal to about 5.2 m of water head) was maintained to ensure gas flow into more of the gas injection ports, about ten of the fifteen ports. With the higher gas flowrates (three to four times greater than in the first experiment), the measured water flowrates were very variable showing reductions to as low as 10% to 20% of the water flowrates that were measured during equivalent single phase flow tests. The higher gas pressures and gas flowrates appeared to push the water through the fracture plane producing pulsing flowrates that frequently exceeded the

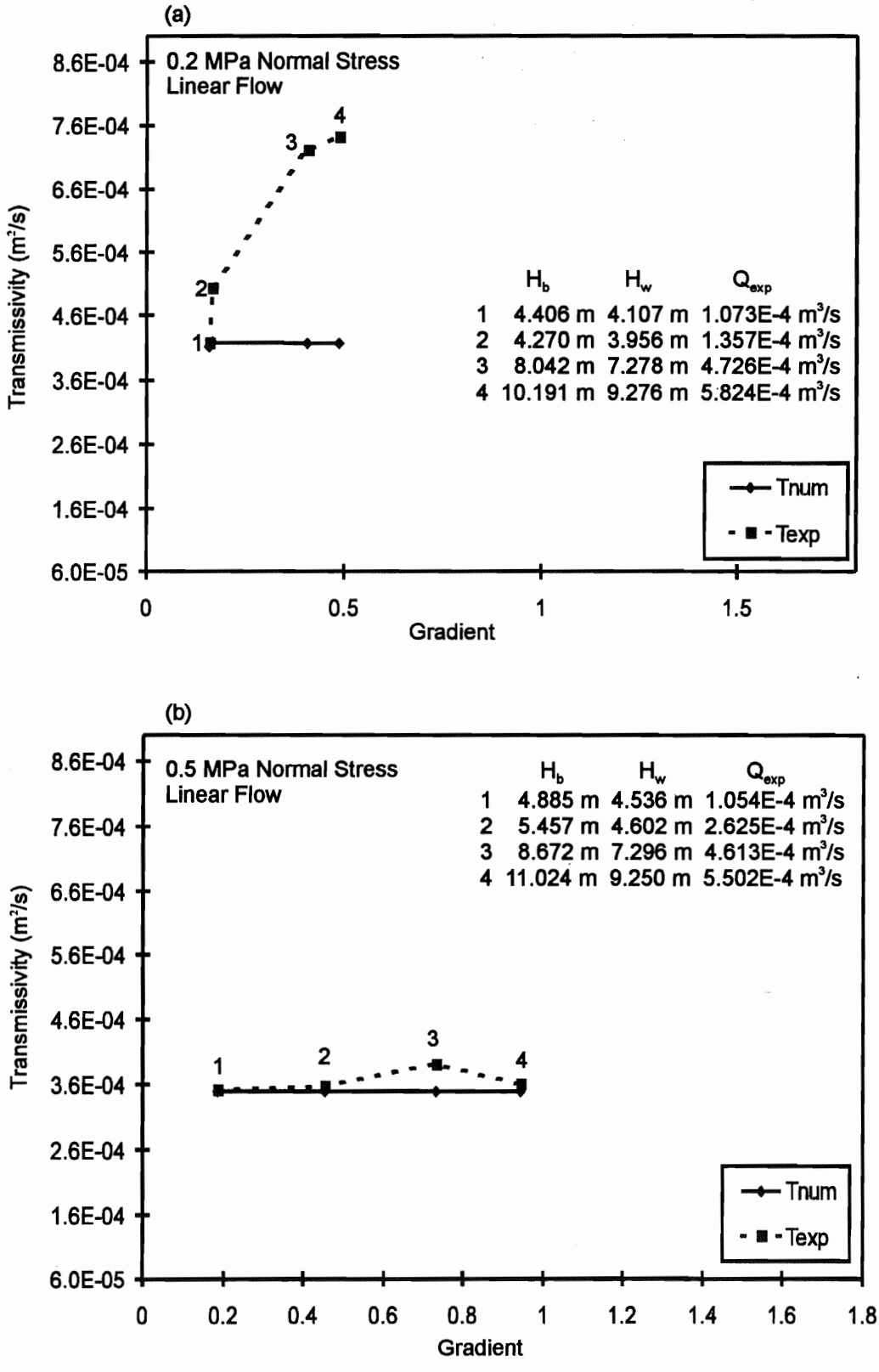

Figure 2-16. Comparison of model transmissivity with transmissivity computed from experimental data for linear east-west flow at (a) 0.2 MPa normal stress and (b) 0.5 MPa normal stress, large scale physical model (1.61 m x 1.88 m).

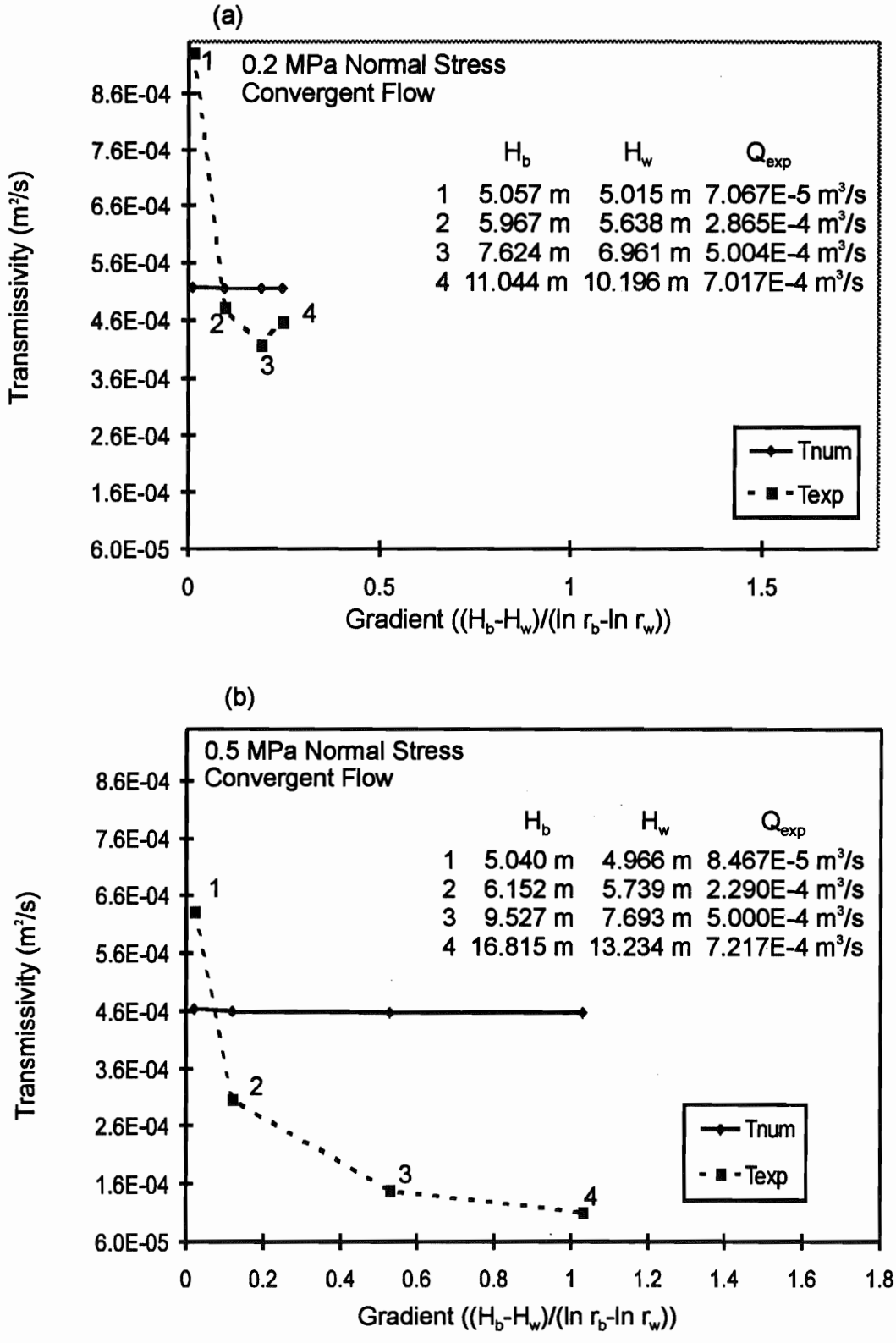

Figure 2-17. Comparison of model transmissivity with transmissivity computed from experimental data for convergent flow at (a) 0.2 MPa normal stress and (b) 0.5 MPa normal stress, large scale physical model (1.61 m X 1.88 m) with 50 mm diameter borehole at an intersection angle of 42°.

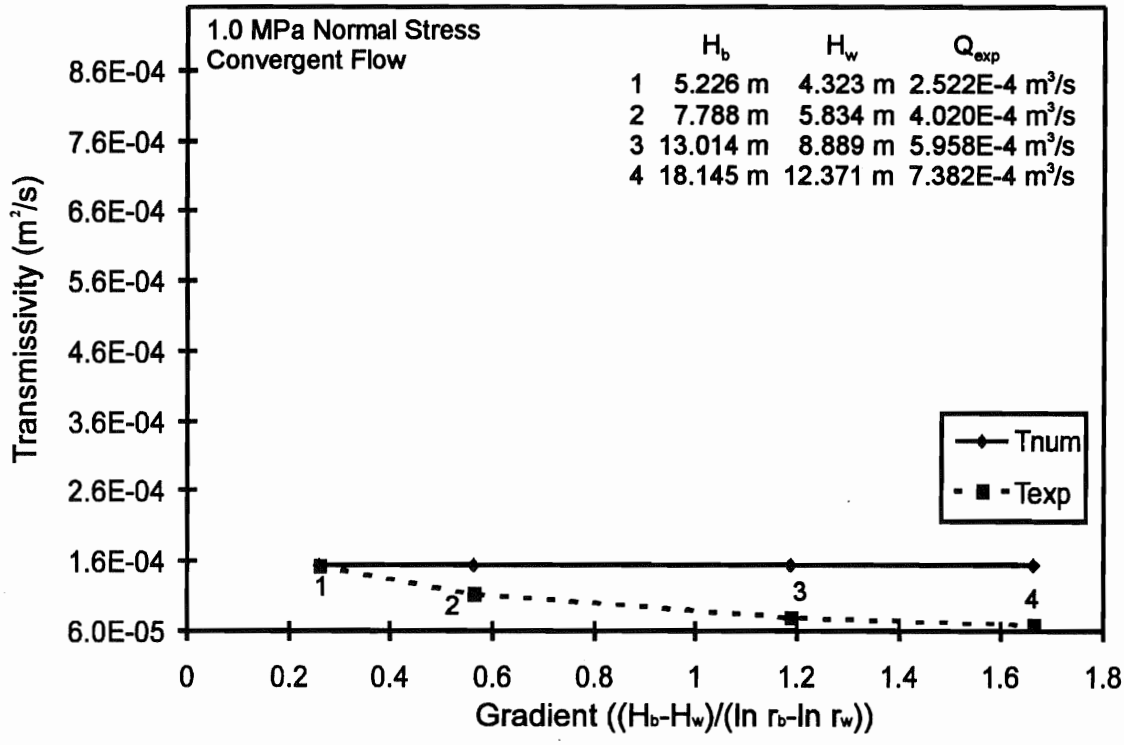

Figure 2-18. Comparison of model transmissivity with transmissivity computed from experimental data for convergent flow at 1.0 MPa normal stress. Large scale physical model (1.61 m x 1.88 m) with 50 mm diameter borehole at an intersection angle of 42°.

reference single phase flowrate for very short periods of time. Water flow out of the fracture plane was very localized, indicating that the water had to seek a way around gas pockets in the fracture plane and the sections of the fracture plane that were assumed to be filled with a continuous stream of gas.

Flow tests were also conducted under convergent flow conditions with injection into two sides of the model (the north and south sides). The measured reductions in water flow during two-phase flow, when referenced to the single phase flow rates, were similar to those observed in the previous linear flow experiments. These preliminary experiments were conducted at a constant normal stress (about 0.5 MPa) and hence the fracture had the same relative roughness.

To provide a more controlled experiment to evaluate the effects of a continuous gas steam on the saturated fracture transmissivities, the flow circuit was modified by adding a gas injection port (Figure 2-1) to the water injection line close to the water injection pump. Miniature gas meters were used to control and measure the volume rate of gas that was injected into the main water line at this location. Table 2-1 shows the volume flowrate of gas as a percent (2.5% or 5%) of the measured water flow, at the applied water pressure. Figures 2-19 and 2-20 present the results of the experiments conducted

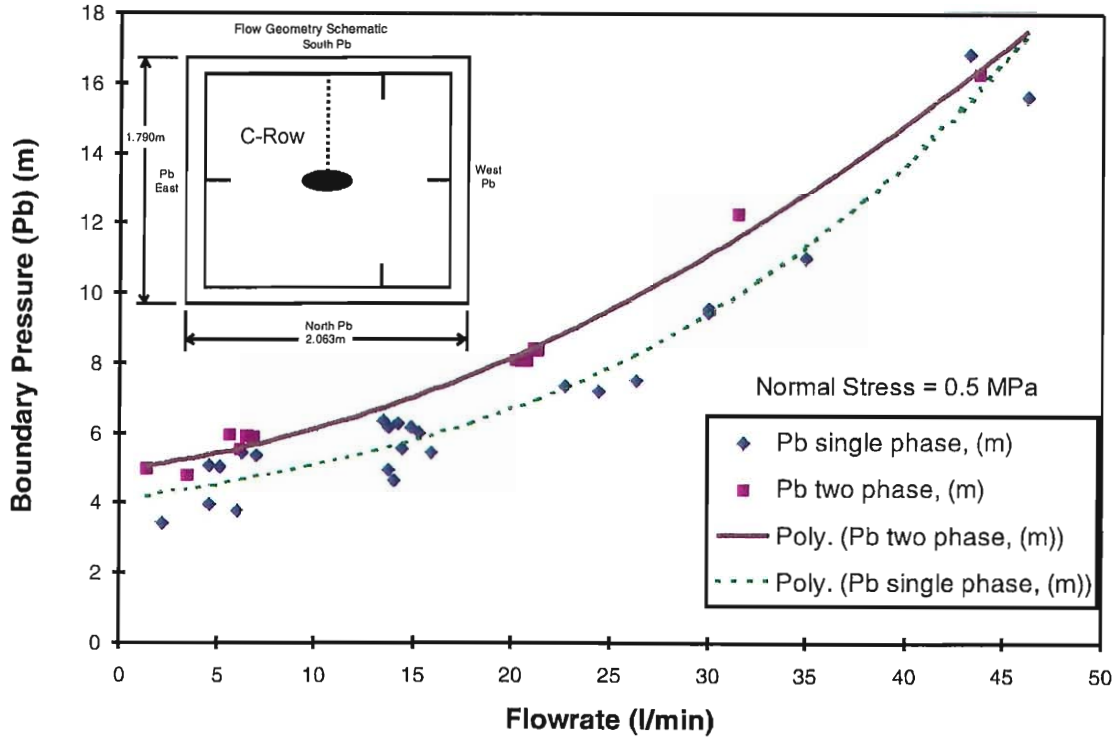

Figure 2-19. Plot of the total or absolute pressure heads along and the C row of manometers, for a range of flow rates, under both single phase flow and for flow with different gas contents, under convergent flow.

under convergent flow conditions for the 0.5 MPa normal stress level for water flowrates that range from approximately 1.0 litres per minute to approximately 45 litres per minute.

Figure 2-19 is a plot of the fluid pressures on the model boundary during each experiment versus the final steady state flowrate for that test. These data show that the flowrate versus boundary pressure curve is highly non-linear with increasing flowrate. It is clear that higher boundary pressures were required for the two phase flow experiments to produce the same flowrates as those measured during the single phase flow experiments. Some of the scatter in the single phase flow data is due to the changes introduced by the long periods of time that the fracture plane was under load between flow tests (ie possible creep effects) and the loading and unloading of the model due to repeated changes in fluid pressure (see Figure 2-5). Normalizing the pressure data by subtracting the measured borehole pressures from the boundary pressures to show the drop in fluid pressure from the outside edge of the model to the central borehole (Figure 2-20), shows that the overall non-linear shape of the pressure drop versus flowrate curve with increasing flowrate is retained. When the data are replotted in this manner, it is obvious that the single phase and the two phase curves differ only by about 3 to 5 %. In addition, both Figures 2-19 and 2-20 show that the difference between single and two phase flow decreases with increasing flowrate and increasing gradient or pressure drop.

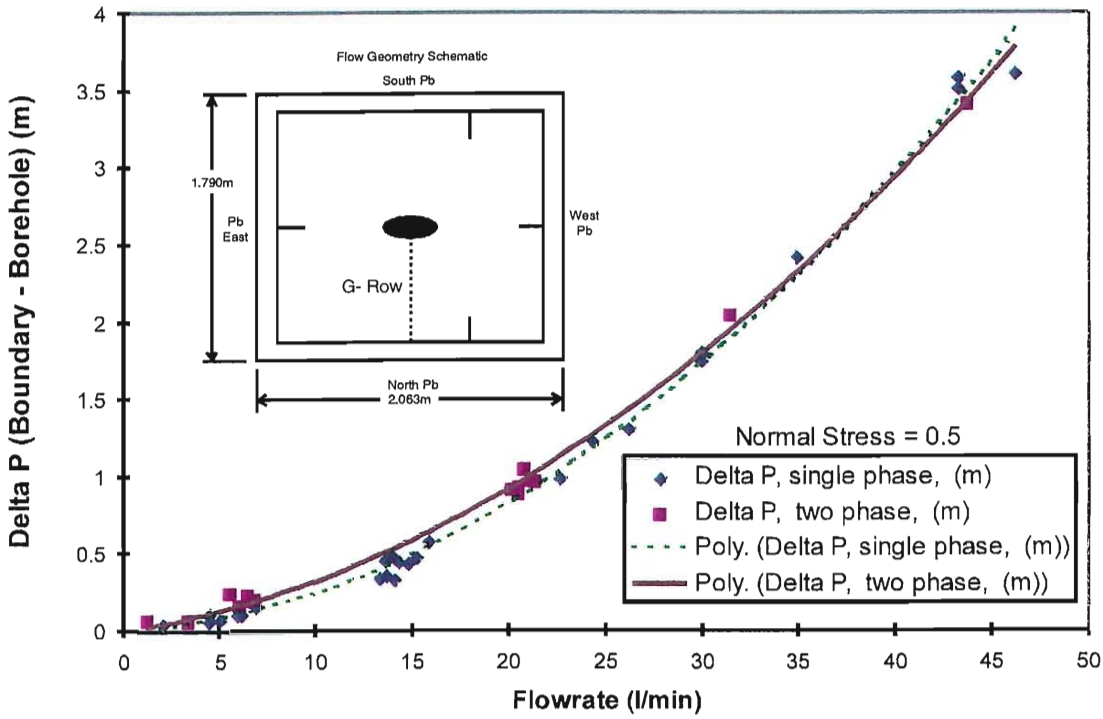

Figure 2-20. Plot of the loss in pressure head (Delta P) as a function of flowrate for both single phase and two phase flow.

A final set of two phase experiments were completed to determine the effects of degassing on the measured fracture transmissivities. For these experiments the flow tanks described in the following chapter were used to saturate the water with carbon dioxide gas at a specified bubble pressure. The fluid pressure within the fracture plane was controlled using a downstream valve and the pressure in the borehole was gradually reduced to generate convergent flow boundary conditions. As the fluid pressure was decreased below the bubble pressure for the gas, bubbles formed in the outlet pipe. However, despite repeated efforts, no significant changes in flowrate could be detected during these degassing experiments. The combined water storage tanks that were used to saturate the water with gas at the specified pressure had a total capacity of less than 400 litres and this limited the length of time at which the flowrates could be maintained at the higher gradients.

2.6 Comparison of Measured and Computed Two Phase Fracture Transmissivities

Figures 2-21 and 2-22 show a selection of the single and two phase flow drawdown curves, measured along the G row of manometers. The solid lines show the results obtained using the MODFLOW model of the LSPM which is based on the calibrations discussed in the earlier sections of this chapter. These results were obtained by assigning the measured boundary conditions to simulation the flowrate and the drawdowns. Although the MODFLOW model includes the inferred variability in hydraulic conductivity over the fracture plane, there are significant differences between the computed pressure profiles or drawdowns and the measured drawdowns with increasing total drawdown and increases in flowrate. At low flowrates, the computed and measured profiles agree reasonably well for both single phase and two phase flow. With increasing flowrate, there is a marked transition or jump in the pressure profile or drawdown at approximately 0.09 m from the center of the borehole. At distances greater than 0.1 m from the center of the borehole, the measured gradients are less than the computed gradients at the higher flowrates.

The differences between the computed and measured flowrates are shown in Figure 2-23 for both the 0.5 and the 1.0 MPa normal stress experiments. This figure shows that while there is a large change in the difference between the computed and measured flowrates with increasing gradient for the 0.5 MPa experiment, there is very little difference in the flowrates between the single phase and two phase flow experiments. Comparison of the transmissivities computed from the experimental data with those used in the model, show the same pattern. The difference between the model transmissivities and those determined from the experimental data are very significant and the differences normally increase with increasing flowrate, especially for the 0.5 MPa stress level. However, the differences between the transmissivities determined from the measured single phase and two phase flow data are more erratic and much smaller.

These initial large scale model experiments were conducted on an existing physical model of a fracture surface which was characterized by small scale roughness and a relatively high fracture hydraulic conductivity. It is clear that changes in the flow regime from laminar to turbulence produces significant non-linear changes in the flowrate with increasing flowrate. The differences in the measured flowrates for single and two phase flow under convergent flow conditions are thought to be partly due to entry pressure effects as the gas and water enter the fracture plane in the boundary reservoirs. The overall effect of the 2.5 to 5 % gas contents is to produce a reduction in flowrate of a similar magnitude to the gas concentration. With increasing flowrates, this difference decreases, demonstrating the dominating effect of the high flowrates that sweep the gas out of the fracture plane due to the low bubble trapping capacity of this fracture plane with its well defined uniform roughness. Much smaller fracture apertures with larger bubble trapping capacity, that will generate high gradients with low flowrates, are needed to clearly separate experimentally the effects of degassing and two phase flow and the effects of non-linear flow in discrete fractures. In addition, since the angle of intersection between the wellbore and the fracture plane will determine the distribution of pressure heads in the immediate vicinity of the wellbore, a range of wellbore-fracture intersection angles should be examined.

Table 2-1 Percent gas for convergent flow tests at two different stress levels

Run	Stress Level (MPa)	Q_{exp} (m^3/s)	H_b (m)	% Gas
2A (gas)	0.5	9.33E-5	5.949	5*
3A (gas)	0.5	5.25E-4	12.239	5*
4A (gas)	0.5	7.29E-4	16.314	5
1B (gas)	1.0	3.00E-6	4.938	2.5
2B (gas)	1.0	2.23E-4	6.885	2.5
2C (gas)	1.0	2.13E-4	6.841	2.5

* Estimated Values

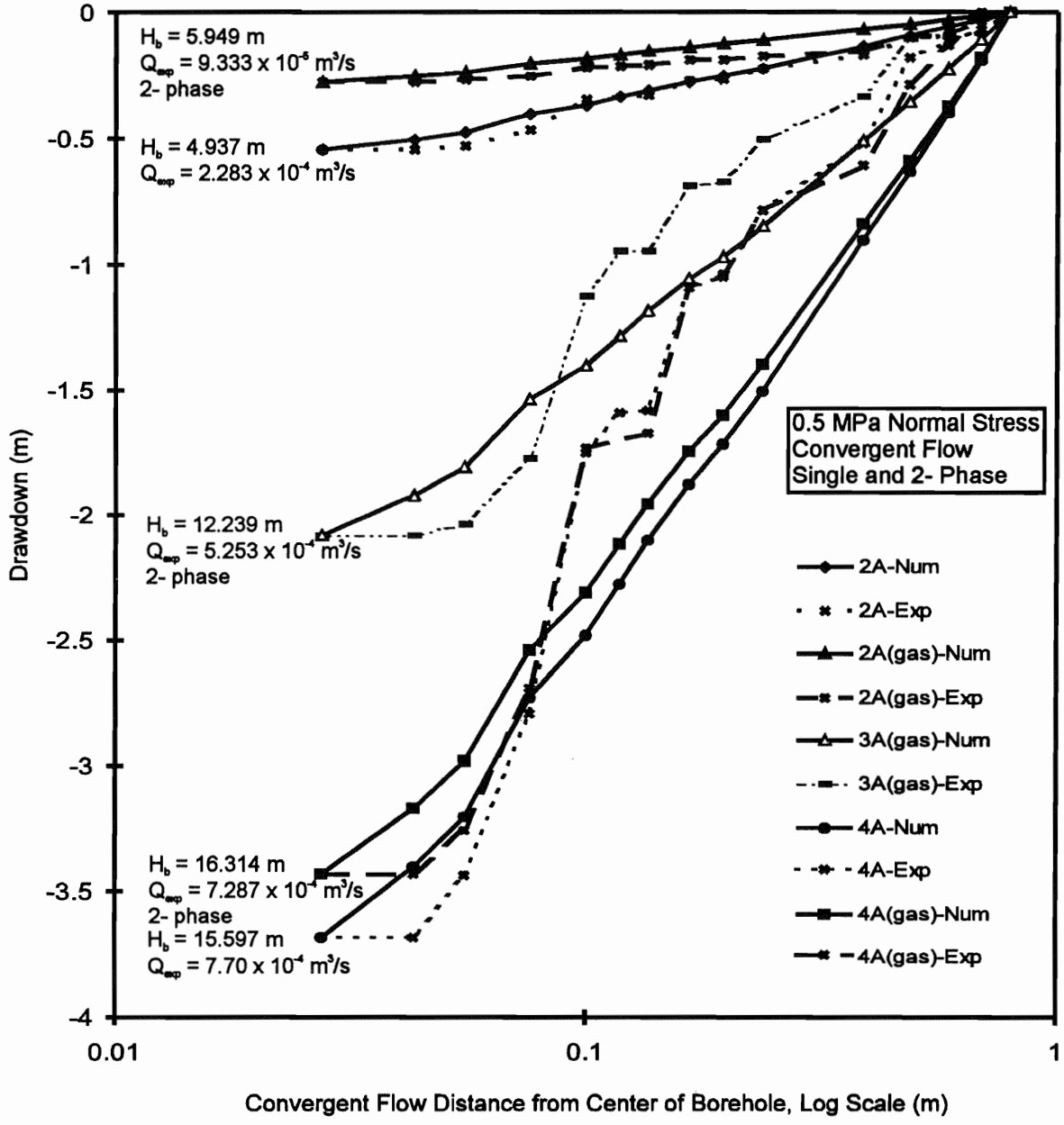

Figure 2-21. Comparison of model and experimental plots of drawdown along the G row of manometers under both single and 2-phase convergent flow at 0.5 MPa normal stress. Large scale physical model (1.61 m x 1.88 m) with 50 mm diameter borehole at an intersection angle of 42 °.

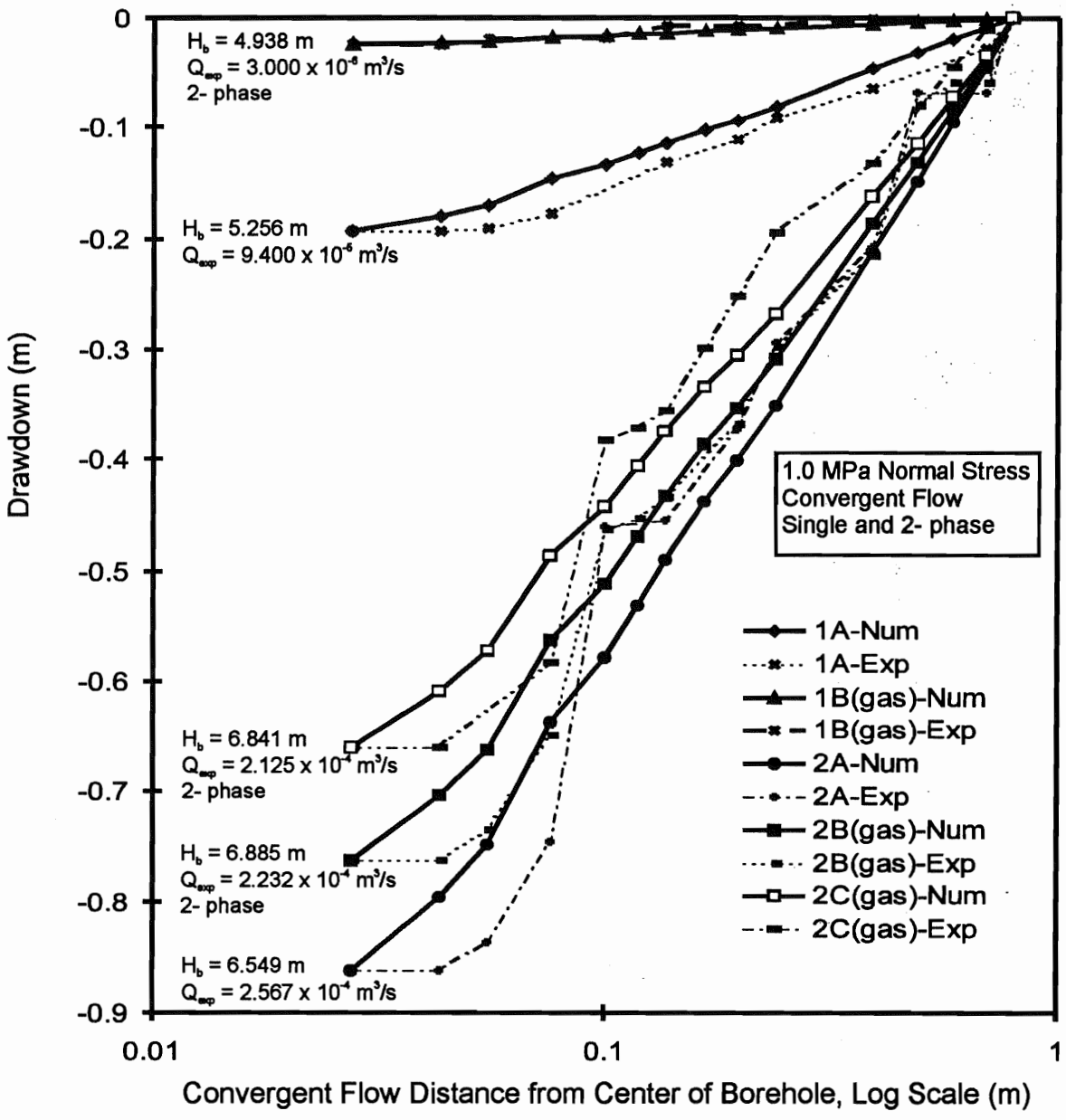

Figure 2-22. Comparison of model and experimental plots of drawdown along the G row of manometers under both single and 2-phase convergent flow at 1.0 MPa normal stress. Large scale physical model (1.61 m x 1.88 m) with 50 mm diameter borehole at an intersection angle of 42 °.

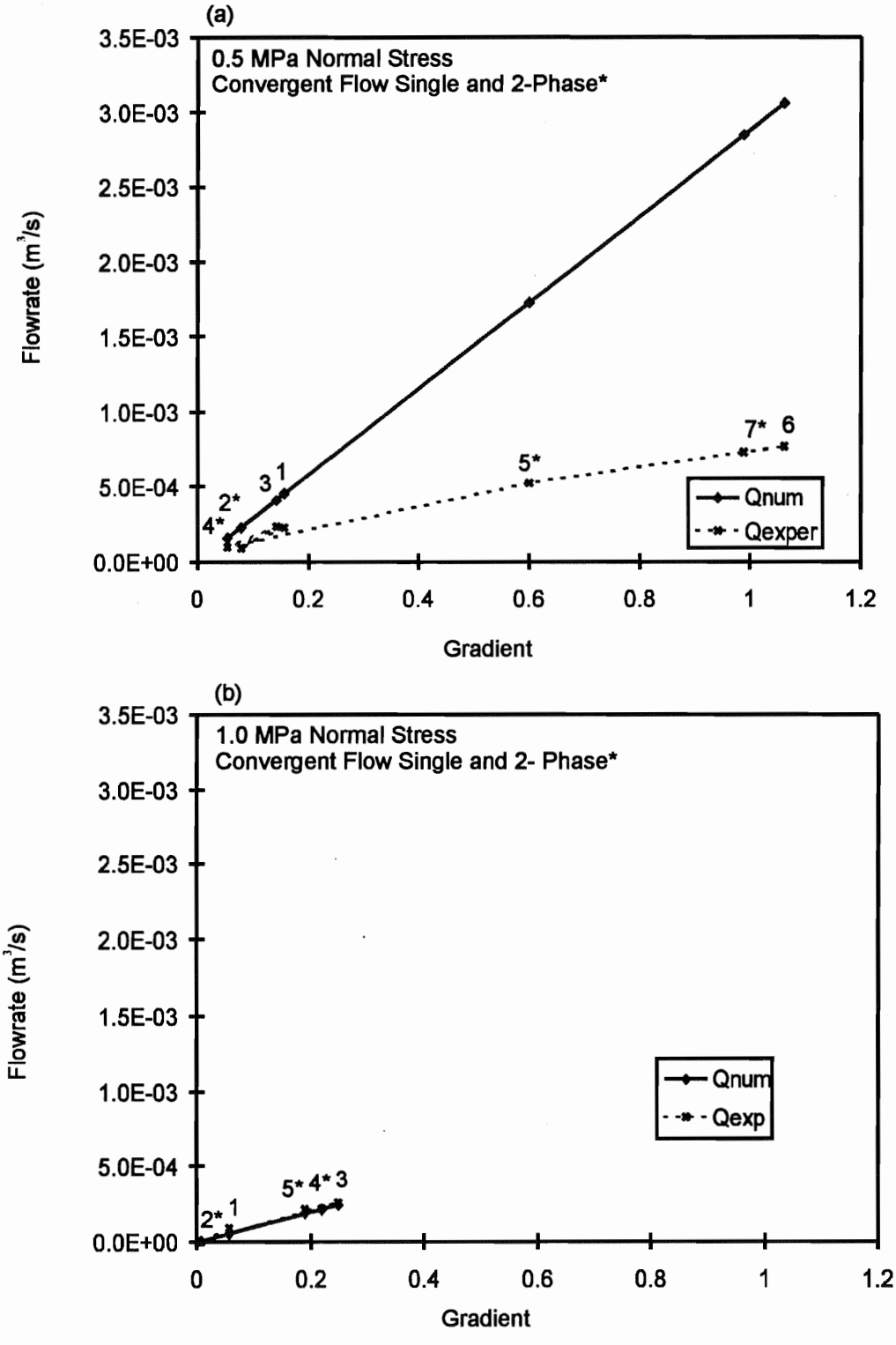

Figure 2-23. Comparison of model flowrates with experimentally measured flowrates for single and two-phase convergent flow at (a) 0.5 MPa normal stress and (b) 1.0 MPa normal stress. Large scale physical model (1.61 m x 1.88 m) with 50 mm borehole at an intersection angle of 42°.

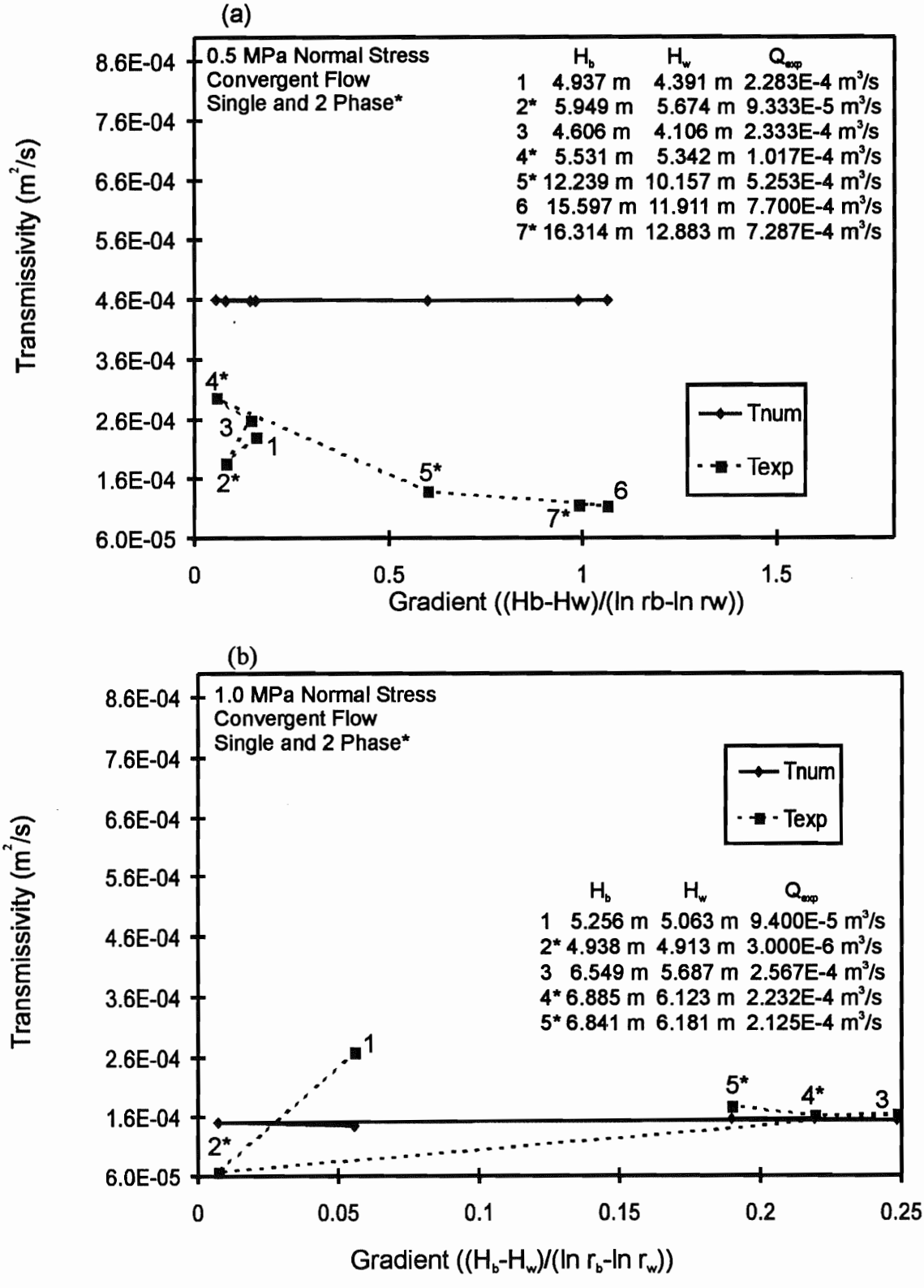

Figure 2-24. Comparison of model transmissivity with transmissivity computed from experimental data for convergent flow, single and two phase at (a) 0.5 MPa normal stress and (b) 1.0 MPa normal stress, large scale physical model (1.61 m X 1.88 m) with 50 mm diameter borehole at an intersection angle of 42°.

3 Small Scale Laboratory Experiments

3.1 Introduction

The small scale laboratory flow studies consisted of single and two phase flow experiments on four fracture plane samples. Two of the samples contained fabricated fracture surfaces and the two other samples contained natural fracture planes that were recovered from the pilot resin site at Äspö; Äspö No. 1 and Äspö No. 2. The two fabricated samples included a relatively planar, sandblasted, sawcut surface in a limestone sample (LST-1) and a fabricated surface (C1) in a concrete sample. The fabricated fracture planes in the limestone and concrete samples provided surfaces with a relatively uniform and small scale surface roughness. The two Äspö samples were typical of the small scale roughness and highly variable apertures of most rough natural fracture surfaces.

The objectives of this part of the laboratory study were;

- To determine experimentally the effects of air invasion and two-phase flow on the permeability of discrete fracture planes as a function of roughness, aperture distribution, contact area, stress and sample size.

- To determine the time required to recover the original permeabilities after air had invaded fracture planes and when fully developed two phase flow conditions had been established as a function of roughness, aperture distribution, contact area, stress and sample size.

A full suite of preliminary experiments were conducted on the sandblasted sawcut surface in the limestone sample and the concrete sample to assess and refine the two-phase flow and degassing test procedures. Test procedures ranged from determining how much water was expelled from a saturated fracture plane due to the injection of a gas at low pressure (gas injection) or determining how much water would be expelled from the fracture plane with the application of a low gas pressure across the end of the fracture plane with the opposite end sealed (gas invasion) to the injection of water that was saturated with gas at the injection pressure and observing the changes in fracture transmissivity with decrease in fluid pressure.

Test results from this series of preliminary tests on the limestone and concrete samples indicated the need to modify the test procedures and the boundary conditions for the small samples to provide for higher pressures on the boundaries during both the air invasion and the proposed degassing experiments on the two natural fracture planes in the Äspö samples. Similarly, the sequence for the gas/air-invasion experiments was reversed, to allow for the removal of increasing amounts of water, to avoid having the

results biased by accumulation of gas in the fracture planes. The experimental procedures are described below.

3.2 Description of Experimental Approach

Both fabricated samples, the limestone sample (LST-1) and the concrete sample (C1) had an overall planar geometry but in the LST-1 sample the sandblasting produced a small scale roughness on the fracture surface. For the concrete sample (C1), a high strength concrete mixture was poured into a mould for the bottom half of the sample and a woven geotextile (Miraffi™ 600) was placed on the wet concrete to create a uniform small scale roughness averaging approximately 1 mm in height. An aluminum plate was used to press the geotextile firmly into the concrete, forming one side of the simulated rough fracture. After curing 4 to 5 days, the aluminum plate was removed and the upper half of the sample was poured into a mould on top of the geotextile to form the opposing side of the fracture plane.

After curing a minimum of 28 days, both moulds were removed from the concrete model and the upper and lower halves of the model were separated. The geotextile was removed and the two halves were carefully reassembled. The resulting fracture was not correlated at the small scale due to the offset nature of the texture of the geotextile fabric. Three gear clamps were then strapped around the model to hold it firmly together and prevent damage to the fracture surface. A 3 mm deep groove was ground into the sample along the outside trace of the fracture and the sides were then ground back to form 45 bevels.This bevelled groove provided a smooth seat for an inflatable packer that was seated against the fracture trace on the sample surface and sealed the fracture during the permeability tests and subsequent resin impregnation.

In the LST-1 sample, manometer ports to monitor fluid pressure changes and fluid injection ports were drilled into the sample. In the C1 sample, the manometer tubes and the fluid injection tubes were cast into the concrete sample. The two cores from the Äspö pilot resin site were supplied as nominal 200 mm cores. These cores were cut to a specified length and the pressure monitoring ports and the fluid injection ports were drilled in each sample. The final fracture planes in these samples were nominally about 200 mm wide and 300 mm in length. The actual dimensions of each sample and the location and numbering of each manometer port is given in latter figures.

Each sample was cast into one half of the steel sample box using a mixture of high strength epoxy resin, fine and coarse silica sand and 4 mm to 8 mm diameter granite aggregate. After curing two days, the upper half of the steel sample box was bolted to the lower half using machined aluminum plates. This assembly was then turned over and the remaining half of each model was cast into the other side of the sample box. The sample box was then placed into the biaxial loading frame using a small crane, the aluminum plates removed and the gear clamps were cut. The sample was then ready for testing.

The circular, biaxial, loading frame (Figure 3-1), designed and developed at Memorial University of Newfoundland, was used to load the samples. For a sample 300 mm by 200 mm in cross-section, this load frame will produce about 30 MPa of normal stress. Applying the full load to smaller samples will result in stresses of 50 to 70 MPa.

In-situ fracture planes are small in comparison to the rock mass making up the fractured reservoir. While the local stress conditions on the asperities in the fracture plane can vary significantly, each planar/smooth fracture plane that is located in the rock mass outside the zone of influence of a borehole or drift experiences an evenly distributed load/average stress in its natural state. In a classical direct shear apparatus, the resultant force moves away from the centroid of the sample with increase in shear stress. This uneven loading produces a rotation in the plane of the applied forces that causes the fracture plane to wedge open. This wedging results in a very flat hydraulic gradient over much of the sample with most of the hydraulic head being dissipated over a very small section of the fracture plane. Therefore, the shear-permeability apparatus in Figure 3-1 was designed in order to simulate in situ conditions and to ensure a fairly uniform loading over the fracture plane such that the resultant load vector always acts through the fracture centroid.

This shear-permeability apparatus (Gale et al., 1990) was used to apply a range of normal and shear stresses to the discrete fracture planes. At selected stresses or loads, permeability tests were conducted using both single and/or two phase liquids with the flow boundary conditions (Figure 3-2) configured to produce flow parallel to the length of the sample.

Figures 3-3, 3-4, 3-5 and 3-6 show the loading and testing sequence for each of the four samples. At least three normal and one or more shear loading cycles were conducted with load/displacement control provided by a servo-controlled hydraulic system. Displacement control was provided using a PC based control program which modified the displacements produced by each actuator to maintain the desired normal and shear stress conditions (Butt, 1994). These loading controls maintained the desired normal stress on the fracture plane and did not restrict the normal displacement of the fracture. Hence, the fracture plane was free to either close or dilate in response to any applied normal and shear loads.

Eight linear variable displacement transducers (LVDTs) were mounted on the sample, two on each of the four corners, to measure average normal and shear fracture displacements as each model or sample was subjected to the loading cycles. Additional electronic sensors were used to record loads, displacements and temperatures during testing. Data from this instrumentation were collected using a microcomputer interfaced to a Keithley 500A Data Acquisition and Control unit. Data acquisition was accomplished using software written in a multitasking software environment (ViewDAC developed specifically for the Keithley system; Keithley Asyst, 1992).

At selected stress levels (Figures 3-3 to 3-6), deionized and partially degassed water was injected at a constant rate into the fracture plane using a PC controlled, constant displacement pump driven by a linear stepper motor. The fracture transmissivity was calculated from outflow and hydraulic gradient measurements at the selected stress levels. For each stress level, at least three measurements of flow rate were made. Fluid

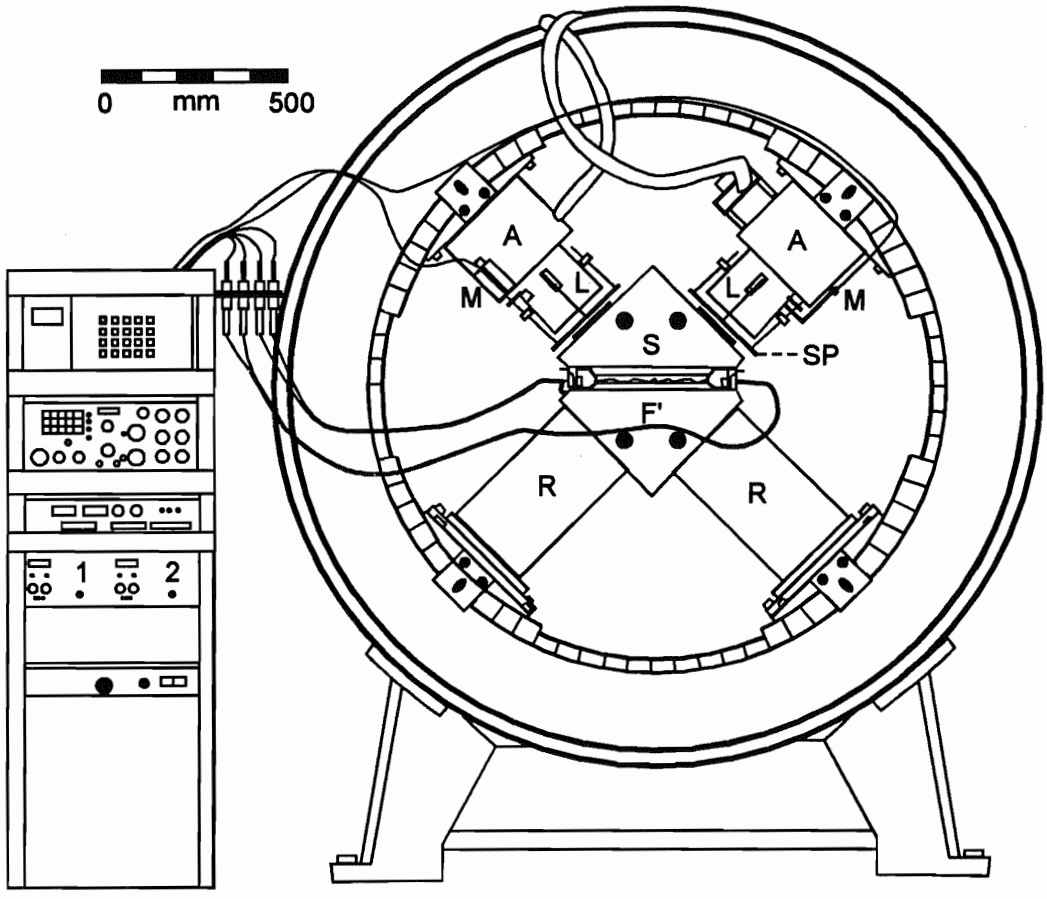

Figure 3-1. Biaxial shear permeability apparatus; A: Actuator, R: reaction member, L: load cell, M: LVDT, S: sample box, SP: swivel plate, F: fracture trace.

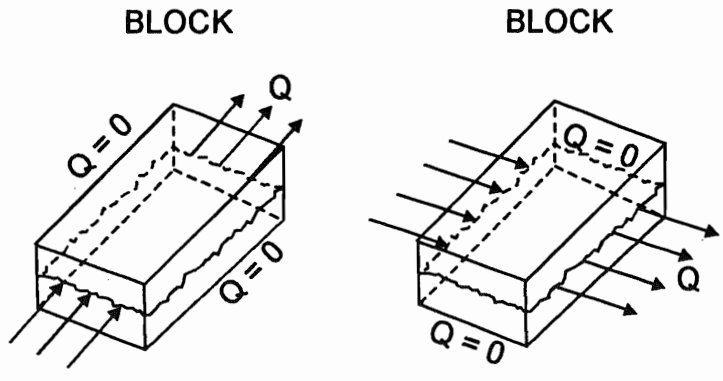

Figure 3-2. Schematic of bi-directional flow measurements.

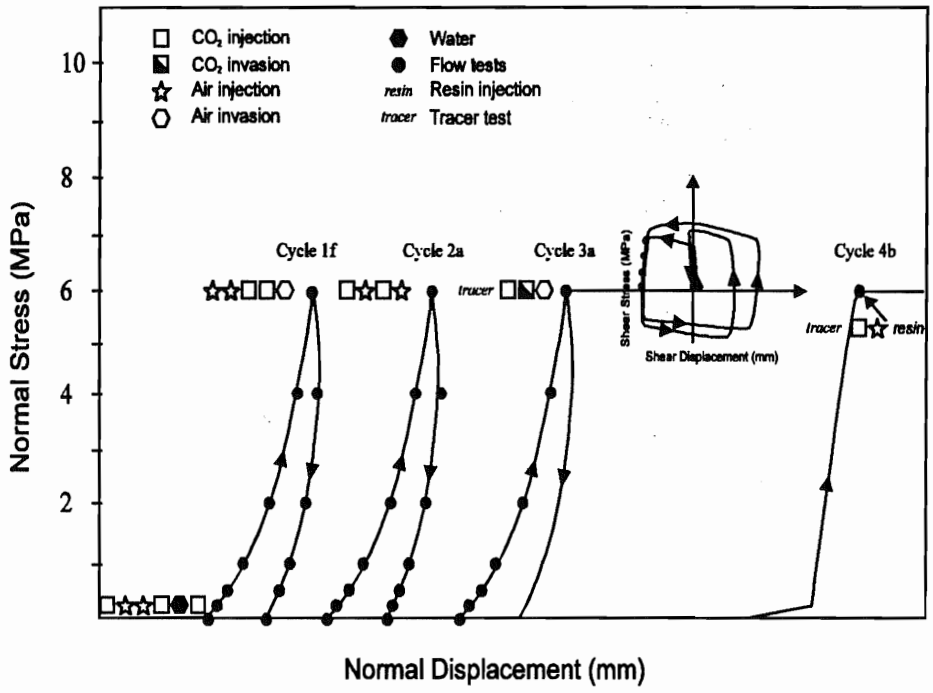

Figure 3-3. Schematic showing loading and test sequences for Limestone sample.

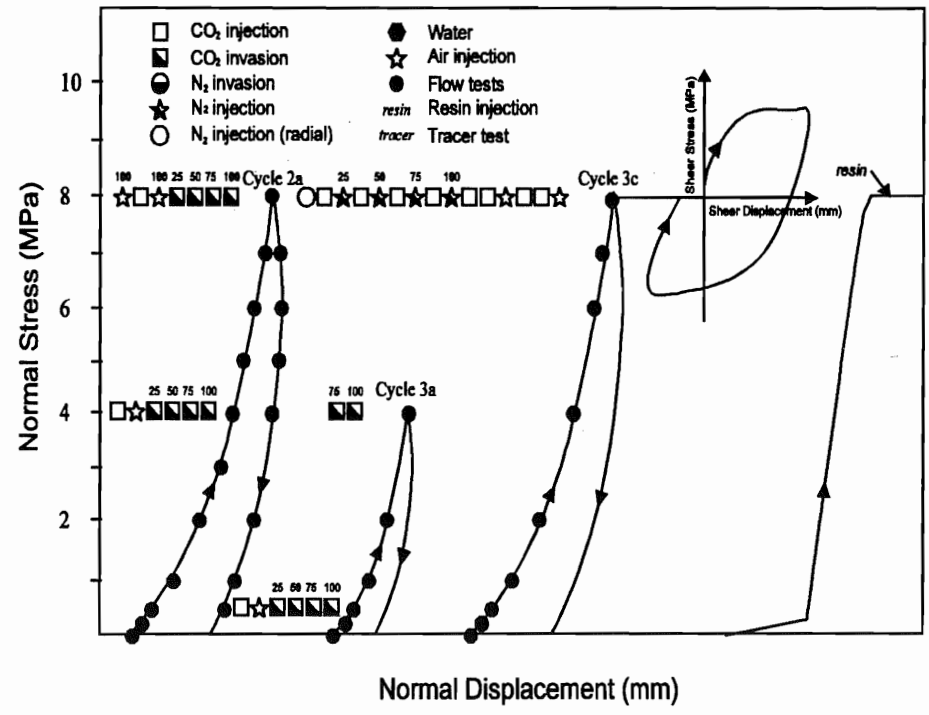

Figure 3-4. Schematic showing loading and test sequences for Concrete sample. The numbers indicate the percentage of the fracture pore water that was removed in each test.

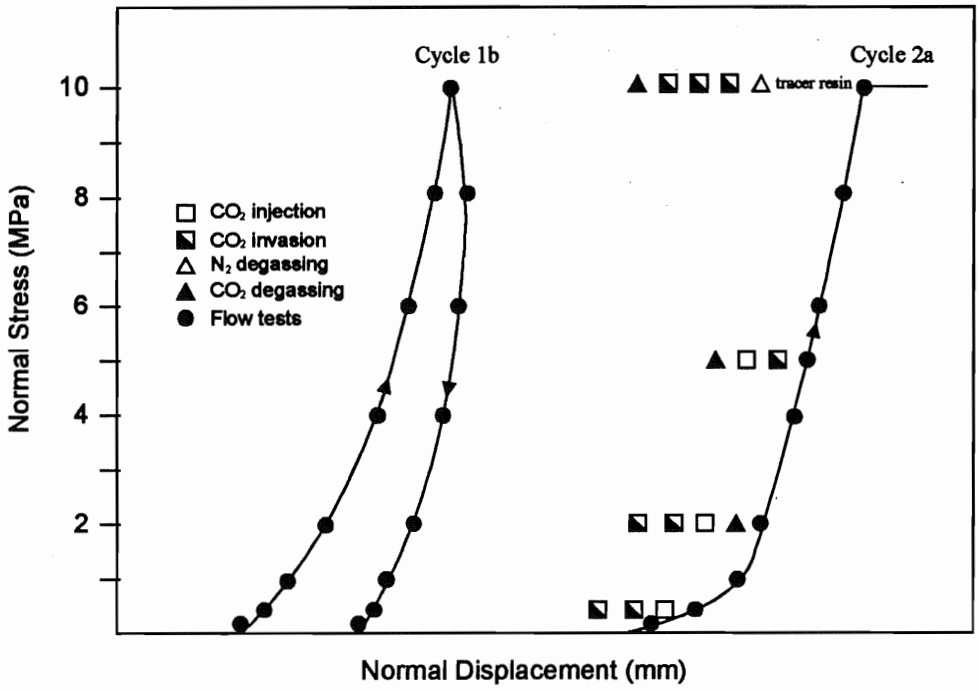

Figure 3-5. Schematic showing loading and test sequences for Äspö *Sample No. 1.*

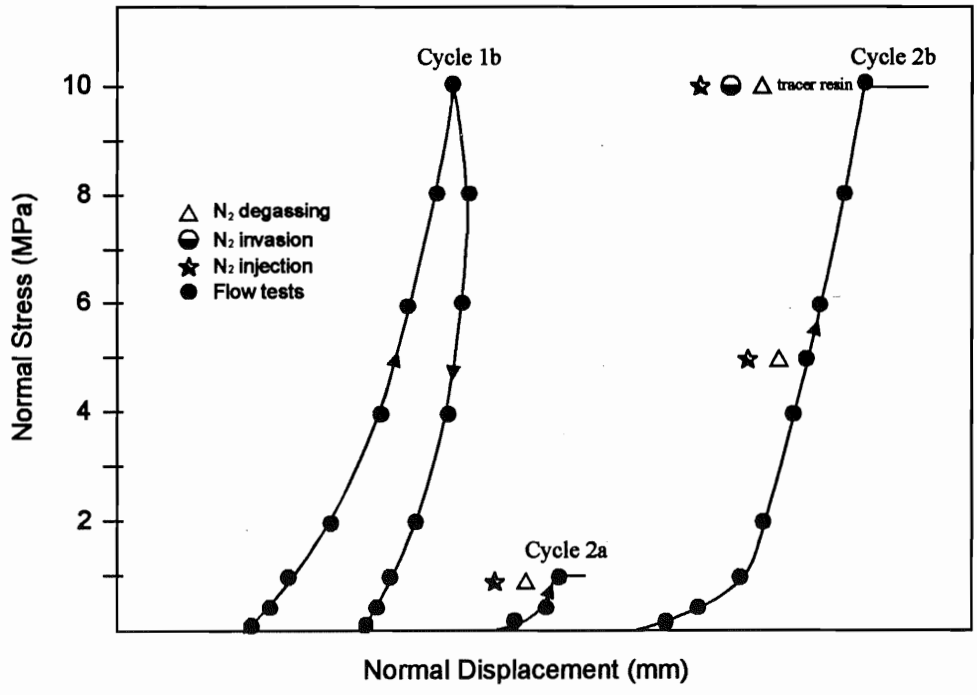

Figure 3-6. Schematic showing loading and test sequences for Äspö *Sample No.2.*

pressures were measured in up to 13 manometer ports distributed over each fracture plane, at least three times for each flow rate measurement, using pressure transducers that were connected through a series of hand operated valves. Each valve had 4 ports, two of which were connected to a set of constant head reference tanks to provide a check on the transducer readings and the other two ports were connected to individual manometers.

At the end of the test sequence, water was evacuated from the fracture plane, the fracture plane was flushed with alcohol, and a coloured epoxy was injected to preserve the pore structure and the geometry of the fracture porespace. Each fracture plane was sectioned, the resin filled pore space was photographed under a microscope to produce photographs of the fracture pore space on a 1:10 to 1:15 scale. These photographs were assembled to create a series of profiles through the fracture plane. The edges of the fracture plane were outlined, digitized and the data analyzed to provide a statistical description of the spatial distribution of the fracture pore space and contact areas.

Three types of two-phase flow tests; air/gas injection, air/gas invasion and degassing were carried out as part of this series of laboratory experiments. Figure 3-7a shows the experimental configuration for the gas injection and gas invasion experiments and Figure 3-7b shows a schematic of the flow boundary conditions that were applied for the air/gas injection, air/gas invasion and degassing experiments.

3.3 Coupled Stress-Flow Measurements

The loading sequence for the limestone sample is shown in Figure 3-3. Each loading cycle is labelled with a number and a letter. For example, the letter f in Cycle 1f for the limestone sample indicates that five attempts were made by loading to self-weight conditions before a successful loading cycle was completed. Likewise, Cycle 2a indicates that the full loading cycle was completed on the first attempt. Figure 3-3 shows that at the top of loading cycle 3a, under a normal stress of 6 MPa, the limestone sample was sheared through two full shear cycles, with approximately 3 mm of shear displacement in each of the two shear directions. This sample was then unloaded to zero normal stress and subsequently reloaded, Cycle 4b, to 6 MPa of normal stress, followed by a sequence of single phase flow tests, air invasion and gas injection tests, and a tracer test to determine the fluid velocity breakthrough curve. After the tracer test, the water was evacuated from the fracture plane, the fracture plane was flushed with alcohol, the alcohol was evacuated and an epoxy resin was injected into the fracture plane. The resin was allowed to cure for 24 hours and then the sample was unloaded, removed from the test frame and sectioned to determine the structure of the fracture pore space.

The test sequence for the concrete sample is given in Figure 3-4. The first loading cycle was stopped at 0.5 MPa of normal stress, Cycle 2a reached a peak normal stress of 8 MPa, Cycle 3a had to be unloaded at 4 MPa of normal stress, Cycle 3c reached a peak normal stress of 8 MPa and at this normal stress the sample was sheared for approximately 0.5 mm in both directions. The sample was then unloaded, followed by reloading to 8 MPa and then resin injection. The two Äspö samples (Figure 3-5 and 3-

(a)

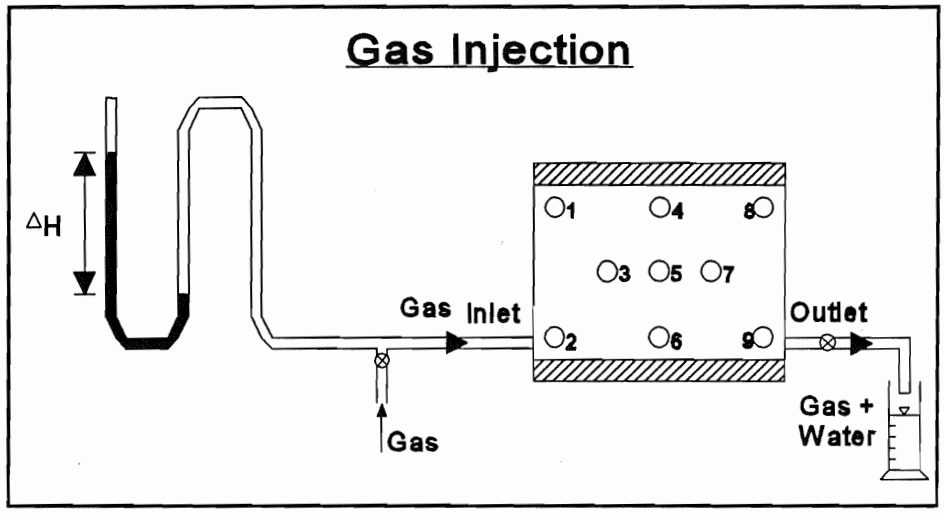

(b)

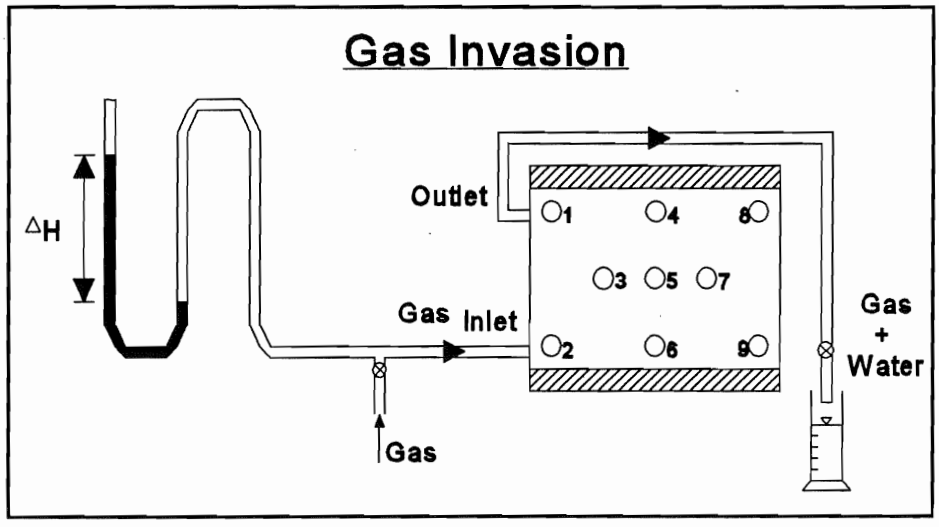

Figure 3-7a. Schematic of flow boundary conditions for both single and and two phase flow experiments.

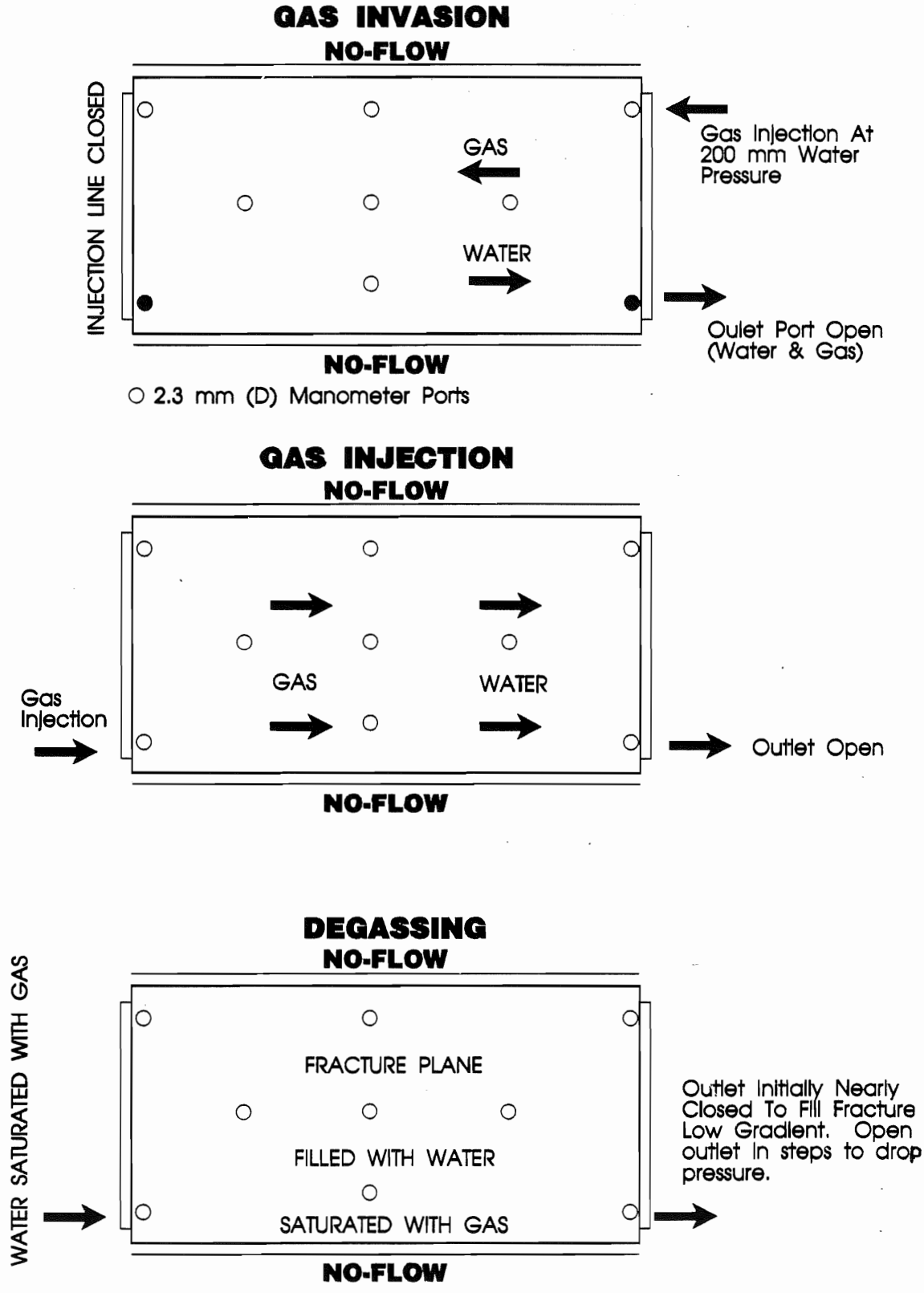

Figure 3-7b. Schematic of the flow boundary conditions that were applied for the gas/air injection, gas/air invasion and degassing experiments.

6) were subjected to one full loading-unloading cycle to 10 MPa of normal stress, Cycle 1b for each sample, with flow tests at selected stress levels during both loading and unloading. Cycle 2a for Äspö No. 2 had to be terminated at 1 MPa. During the second full loading cycle for each sample, the flow tests were followed at selected stress levels by gas invasion, gas injection and degassing experiments. At the peak normal stress of 10 MPa for both samples, a tracer test was completed followed by resin injection with the normal alcohol injection and removal sequence. Both of the two Äspö samples were subjected to normal stress loading only.

Figures 3-8, 3-9, 3-10 and 3-11 show the normal displacement or fracture closure as a function of normal stress. All four samples show some degree of hysteresis or permanent fracture deformation/closure between the loading and the unloading parts of the cycle. This hysteresis generally decreases with increase in the number of loading cycles. While the single and two-phase flow tests were being conducted at selected stress levels, the normal stress was held constant for a considerable period of time. As a result of maintaining the normal load constant for different periods of time, the fractures tended to creep or close. Creep effects are more noticeable in the limestone and concrete samples. However, part of the fracture closure at the top of Cycle 3a in the limestone sample and in Cycle 3c in the concrete sample was produced by the contractant behaviour of the fracture plane during shear cycles on these two samples.

The maximum fracture closure, including hysteresis between loading and unloading parts of the cycle, was much less in the two fabricated fracture samples than in the two Äspö samples. In addition, the natural fracture samples show a more non-linear stress versus displacement curve than the fabricated fracture planes. Both the loading and unloading parts of the test cycles for the fabricated fracture planes can be closely approximated by a straight line. The two natural fractures show a strong stiffening effect with increasing load or stress.

Figures 3-12 and 3-13 show the shear stress versus shear displacement for the shear tests on the limestone and concrete samples. Using the measured shear stress and the applied normal stress, the computed sliding friction angle for the limestone sample increases from approximately 23 degrees at the beginning of shear displacement to a maximum of 35 degrees when the peak shear is generated during the second shear loop for shear displacements of approximately 3 mm in each direction. This limestone sample does not show any pronounced reduction in shear strength with increasing shear displacement or shear history. This shear stress versus shear displacement behaviour confirms that the fracture surface is relatively planar and is characterized by small scale roughness. The peak shear stress generated in shearing the concrete sample under a normal stress of 8 MPa, over a distance of about 0.14 mm, indicates a residual friction angle of about 32 degrees. The shape of the initial part of the shear stress versus shear displacement curve for the concrete sample, and the magnitude of the peak shear stress that was generated, suggests that the fracture surface is characterized by small scale roughness with no evidence of any dilation due to large scale roughness for this small magnitude of shear displacement.

Figures 3-14, 3-15, 3-16 and 3-17 show how the fracture transmissivity changes as a function of normal stress for each sample under both loading and unloading conditions.

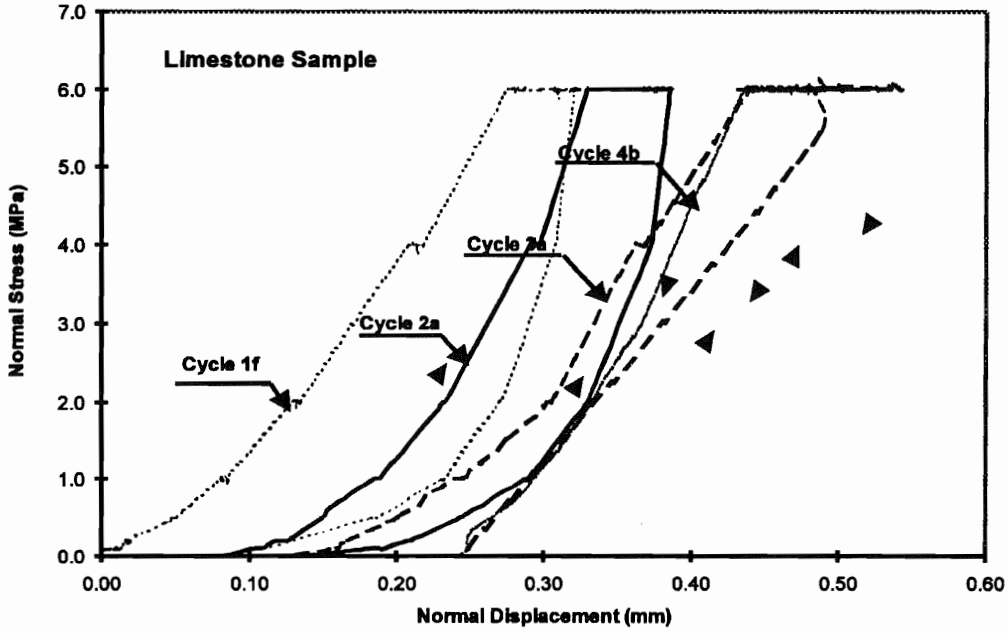

Figure 3-8. Average fracture closure as a function of normal stress for the main loading cycles. This natural fracture plane sample measures192 mm by 285 mm and was fabricated by sand-blasting a sawcut in a limestone sample.

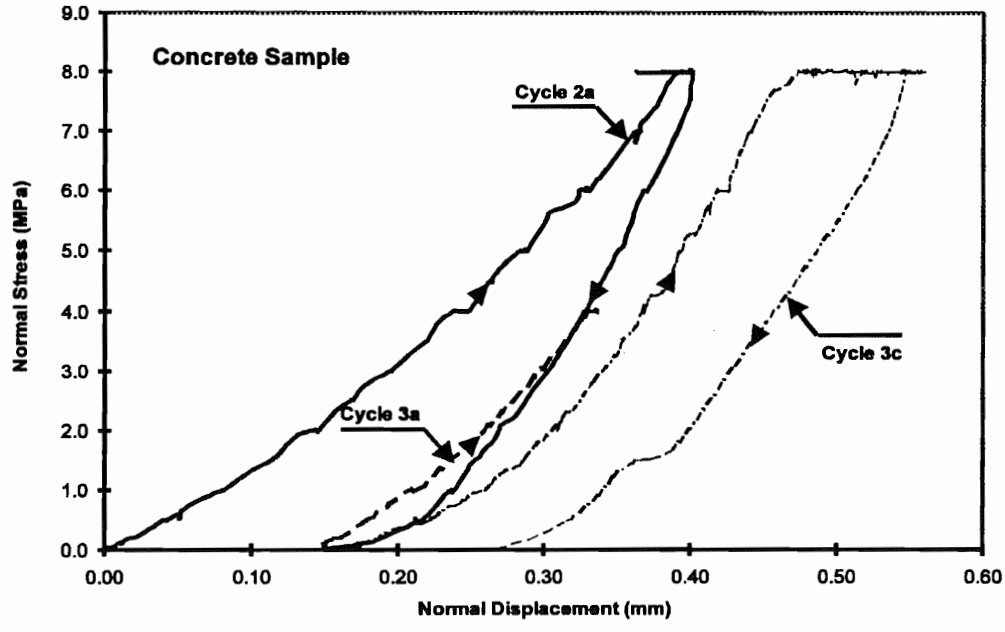

Figure 3-9. Average fracture closure as a function of normal stress for the main loading cycles. This natural fracture plane sample measures 200 mm by 280 mm and was fabricated using high strength concrete.

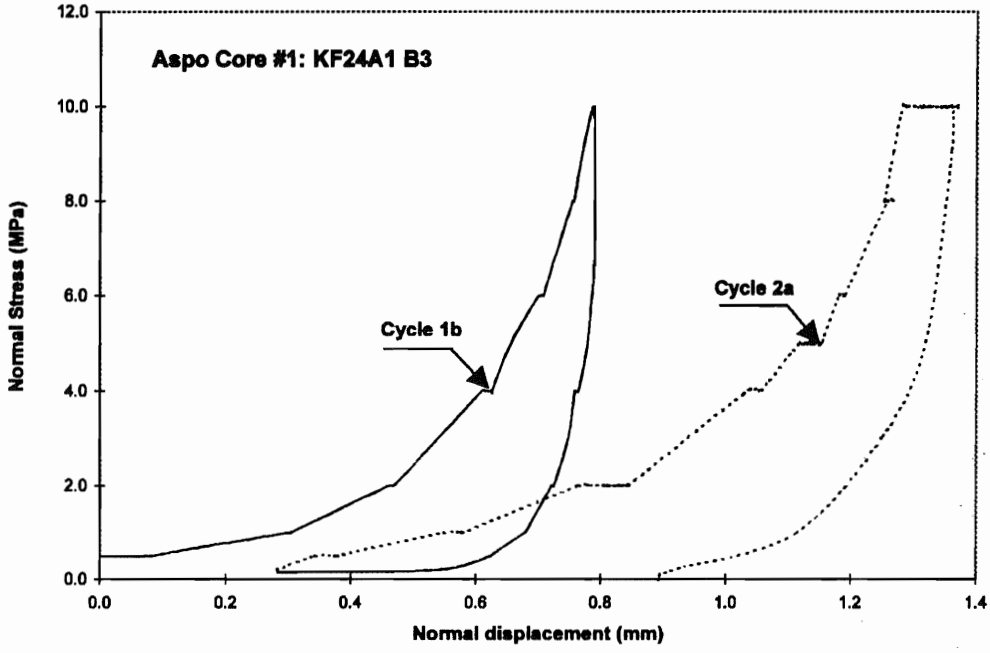

Figure 3-10. Average fracture closure as a function of normal stress for the main loading cycles. This natural fracture plane sample measures 240 mm by 290 mm.

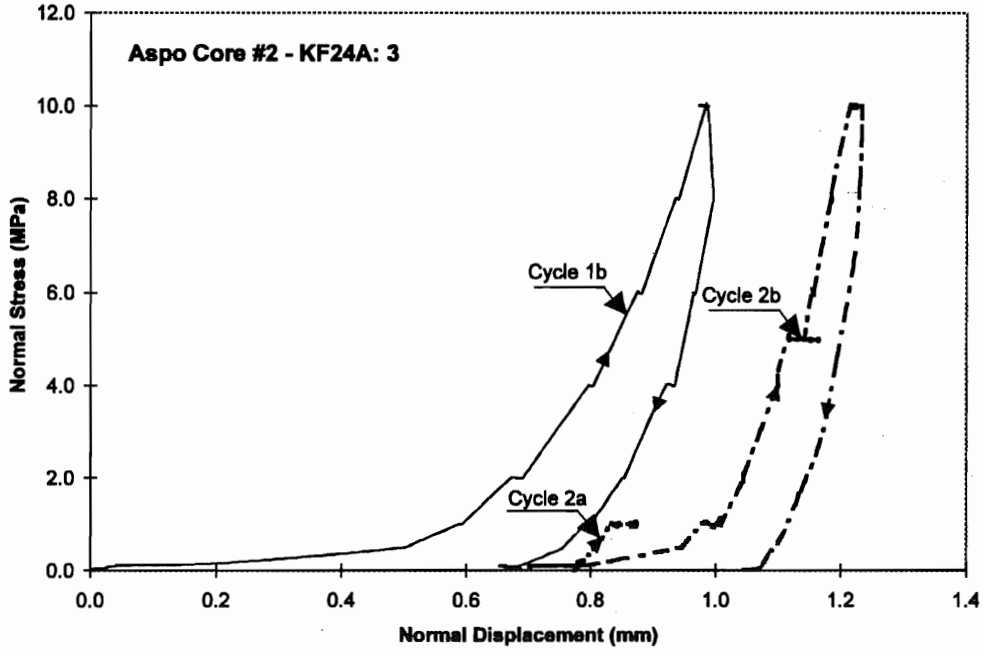

Figure 3-11. Average fracture closure as a function of normal stress for the main loading cycles. This natural fracture plane sample measures 240 mm by 290 mm.

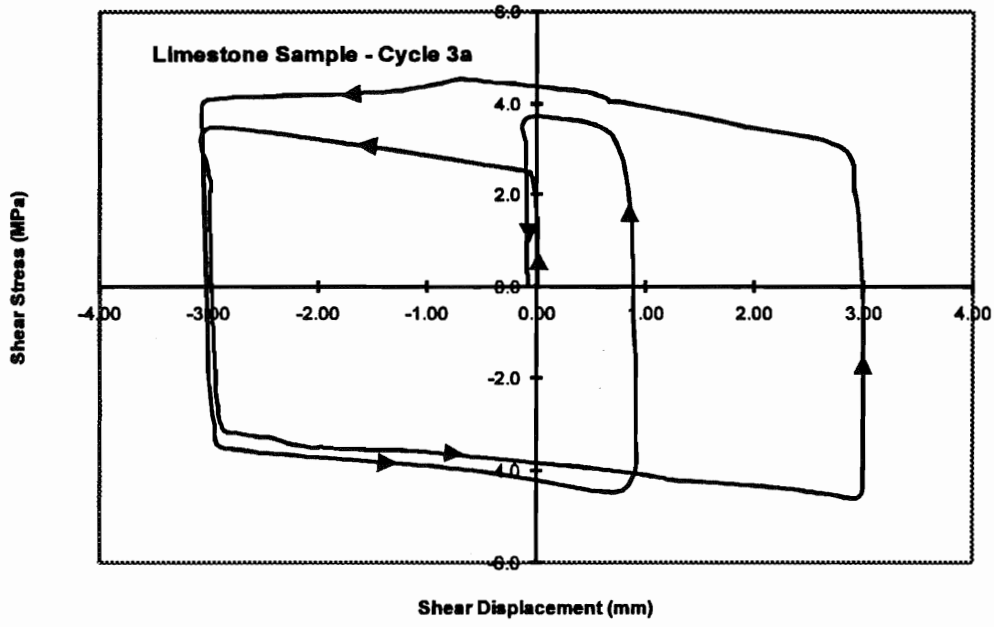

Figure 3-12. Average shear displacement at the top of loading cycle 3a for the limestone sample as a function of shear stress, at a normal stress of 6 MPa. The arrow heads indicate the loading pathway.

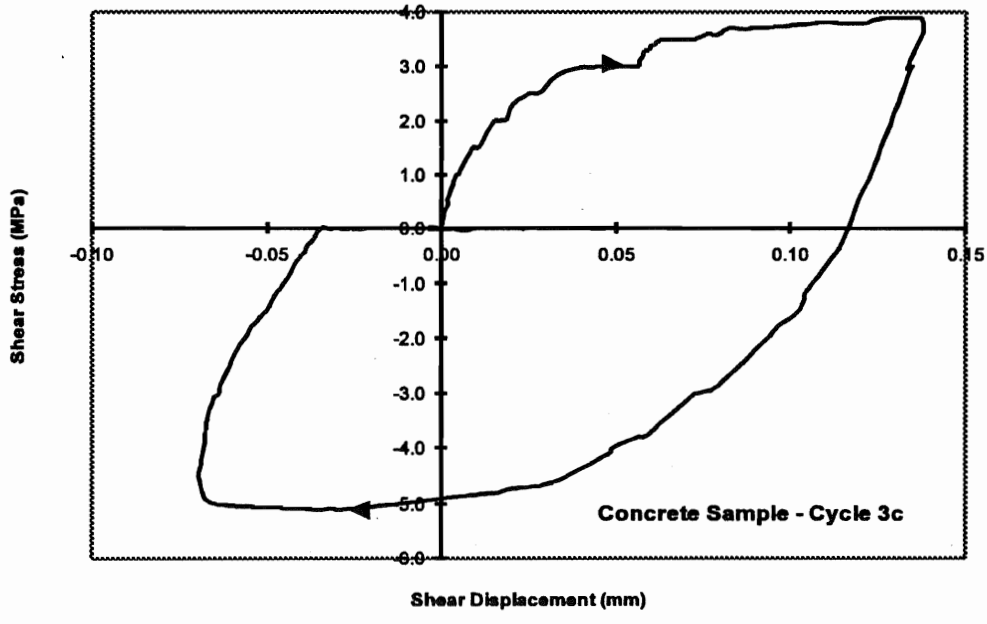

Figure 3-13. Average shear displacement at the top of loading cycle 3c for the concrete sample as a function of shear stress, at a normal stress of 8 MPa.

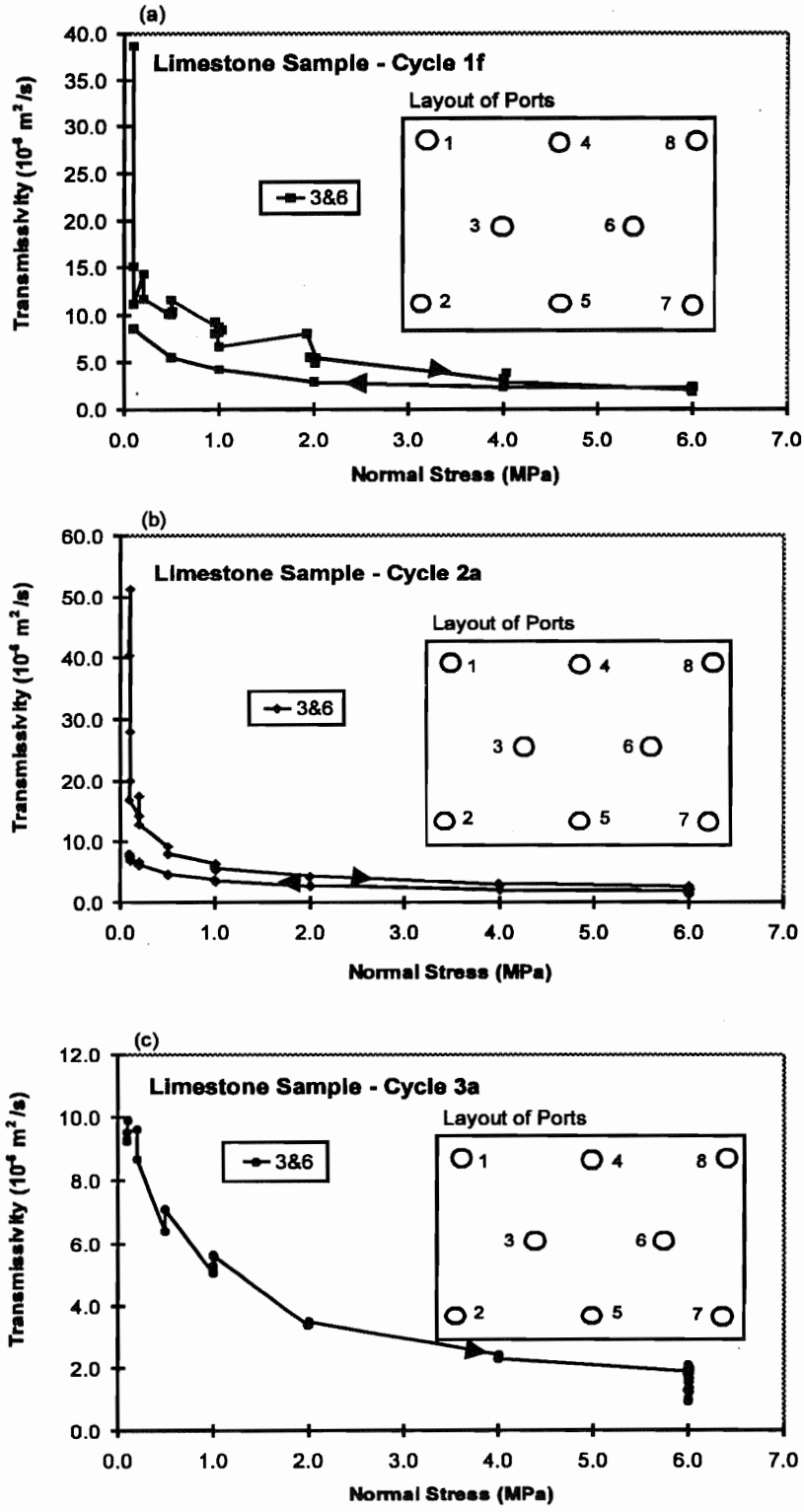

Figure 3-14. Transmissivity changes as a function of normal stress for the limestone sample, during (a) loading-unloading cycle 1f, (b) loading-unloading cycle 2a, and (c) loading cycle 3a, based on the hydraulic gradients between manometers 3 and 6.

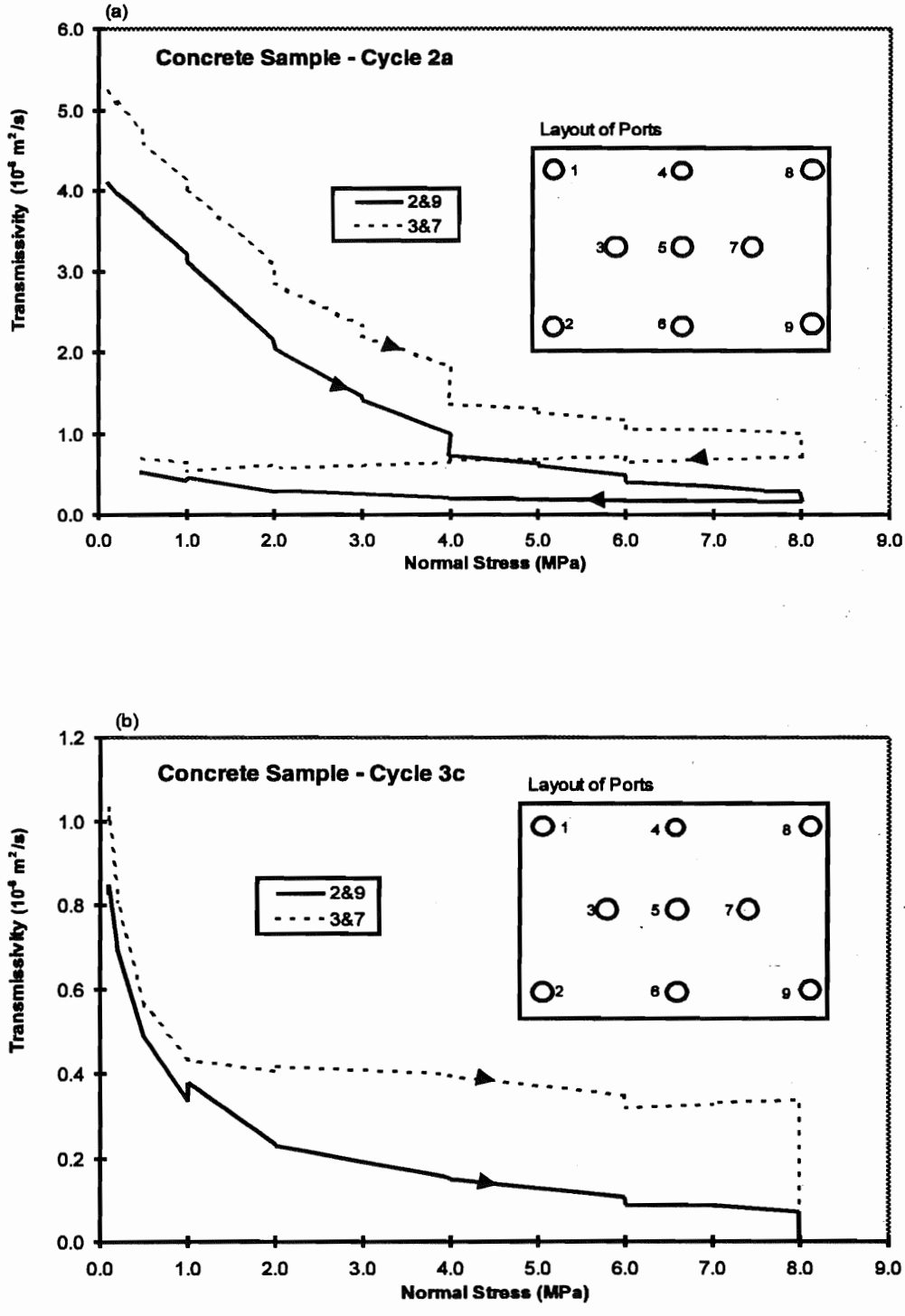

Figure 3-15. Transmissivity changes as a function of normal stress for Concrete sample, during (a) loading-unloading cycle 2a and (b) loading cycle 3c, based on the hydraulic gradients between two different sets of manometers; between 2 and 9 and between 3 and 7.

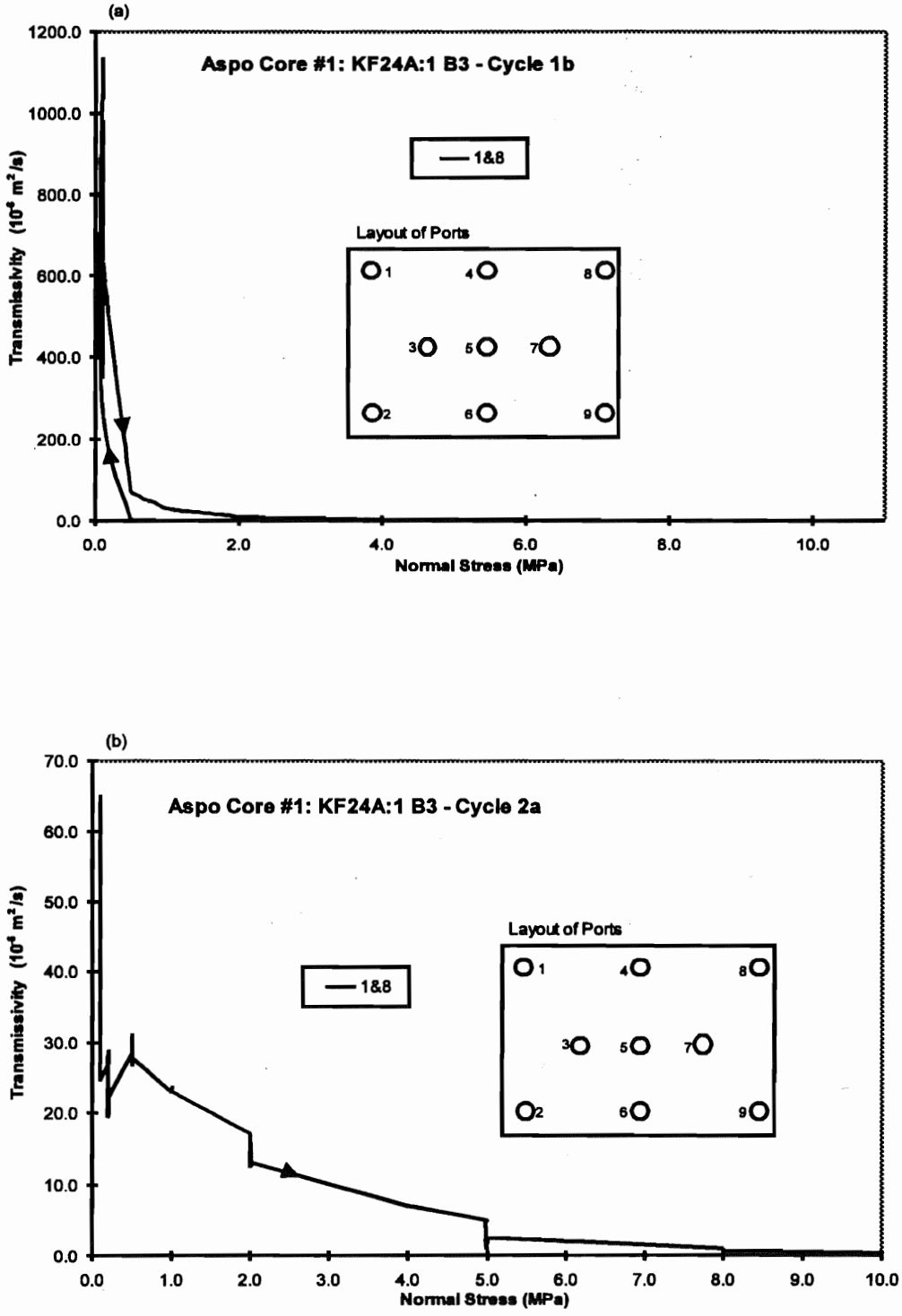

Figure 3-16. Transmissivity changes as a function of normal stress for Äspö No. 1 sample, during (a) loading -unloading cycle 1b and (b) loading cycle 2a, based on the hydraulic gradients between manometers 1 and 8.

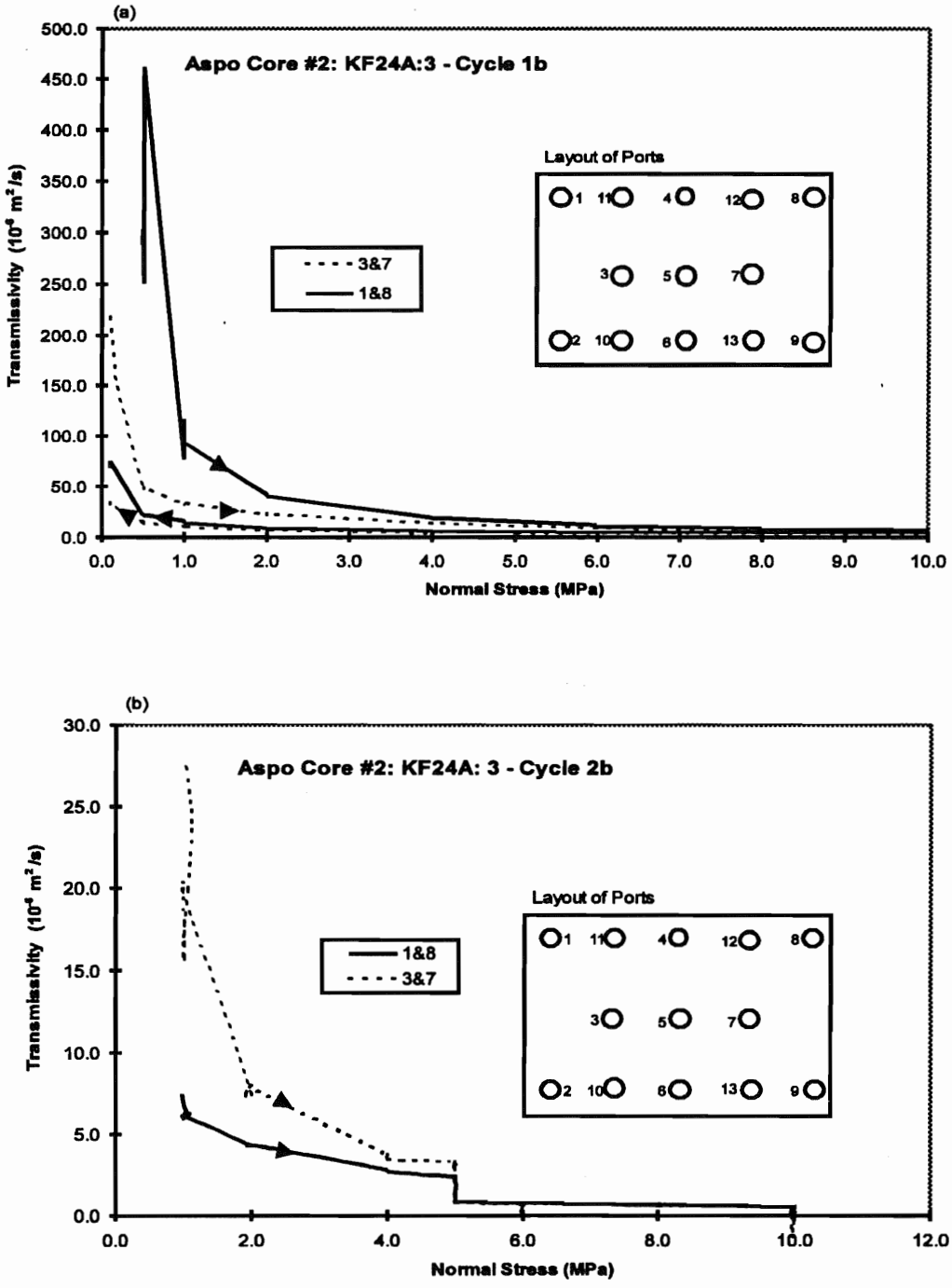

Figure 3-17. Transmissivity changes as a function of normal stress for Äspö No. 2 sample, during (a) loading-unloading cycle 1b and (b) loading cycle 2b, based on the hydraulic gradients between two different sets of manometers; between 1 and 8,and between 3 and 7.

The location and number of each manometer port for each sample is shown in each figure. The fracture transmissivities have been calculated using the measured flowrates and one or more gradients that were measured between selected manometers. For comparison, it should be noted that the transmissivity measured during the Cycle 3a loading cycle for the limestone sample is about a factor of 10 greater, at both low normal stress as well as at peak normal stress, than the measured fracture transmissivities for Cycle 3c of the concrete sample. By contrast, the two Äspö natural fracture plane samples have fracture transmissivities at low normal stress in the first loading cycle that are approximately 500 to 1000 times greater than those measured for Cycle 2a of the concrete sample and about 30 to 60 times greater for the corresponding final loading cycles. However, the fracture transmissivities at peak normal stress in the final loading cycle are very similar for the concrete sample and the two Äspö samples The irregular nature of the measured transmissivities in the last loading cycle of the two Äspö samples, as a function of normal stress, is due to the transient changes in transmissivity that were produced by changes in the gas content within the fracture planes.

Figures 3-18 and 3-19 show the tracer breakthrough curves for Äspö 1 and Äspö 2, respectively, for constant source tracer tests at the peak normal stress of 10 MPa. The average travel time, based on the 50% of peak concentration arrival times, for these two samples ranges from 3 to 4 minutes. The tracer tests were conducted by using a back flushing technique to recover the effluent water and part of the fluctuation in concentrations is due to small variations in the flowrate of both the tracer and the distilled water that was used for back flushing. The abrupt rise in the first part of the breakthrough curve for the Äspö 1 sample suggests that the pore space is much better connected in this sample than it is in the Äspö 2 sample. The more gradual curve for the Äspö 2 sample and relatively slow build-up to the peak concentration, which was not reached in this sample until the tracer had been flowing through the sample for approximately 12 to 14 minutes, suggests that the fracture pore space in the Äspö 2 is much more heterogeneous and less well connected.

3.4 Description of Fracture Roughness

Figures 3-20, 3-21, 3-22 and 3-23 are photographs of selected resin filled cross sections, approximately 10 mm in length, through the sandblasted sawcut fracture in the limestone sample, the fracture plane created with the geotextile fabricate in the concrete sample, and the two natural fracture plane Äspö samples, respectively. Figure 3-20 shows the long, tabular, nature of the fracture pore space, in the limestone sample. The walls of the open tabular pore space are relatively smooth. This pore space structure is typical of that exhibited by natural shear fractures. Areas that have been labelled "voids' are thought to represent sections that were either filled with water or alcohol or, in some cases, isolated pores that the resin could not penetrate. The section labelled "shattered crystal" is thought to represent a piece or wafer of loose rock that was present in the fracture plane or was dislodged or generated (gouge) by the loading process. Generally, these rock fragments show some degree of resin impregnation but they usually have a well defined fracture trace on both sides of the fragment.

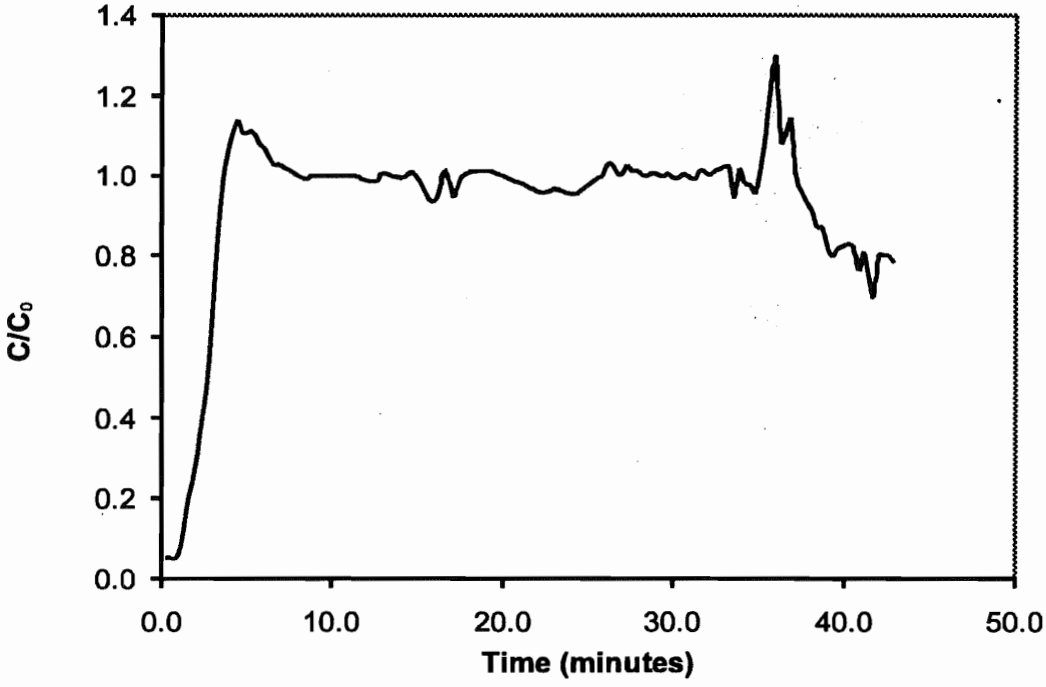

Figure 3-18. Tracer breakthrough curve for Äspö 1. Test conducted at normal stress equal to 10 MPa.

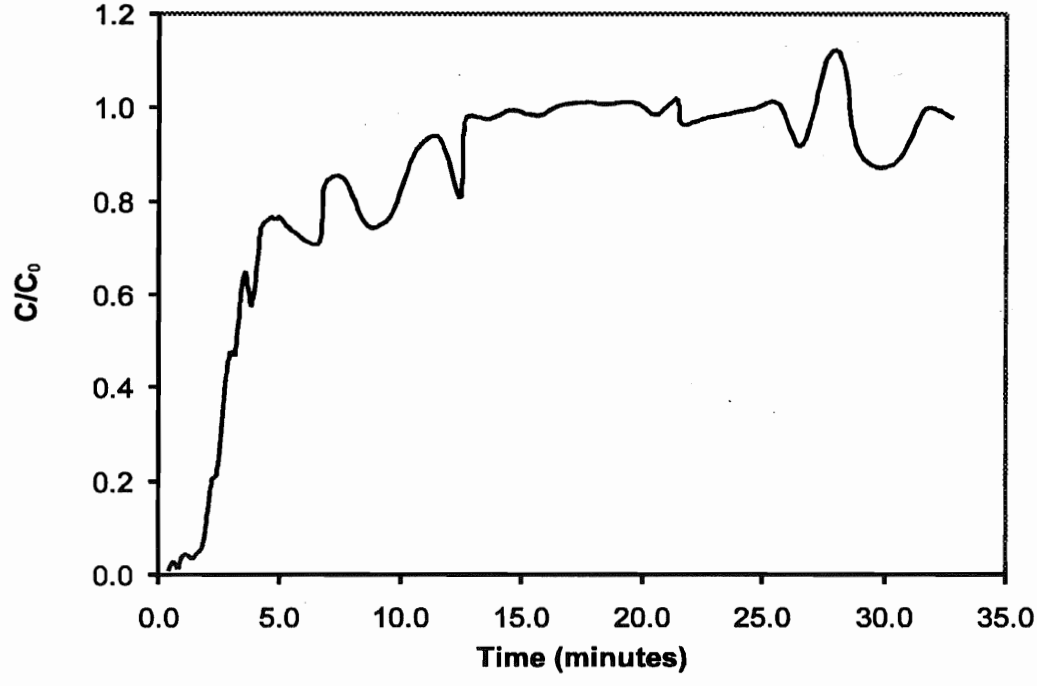

Figure 3-19. Tracer breakthrough curve for Äspö 2. Test conducted at normal stress equal to 10 MPa.

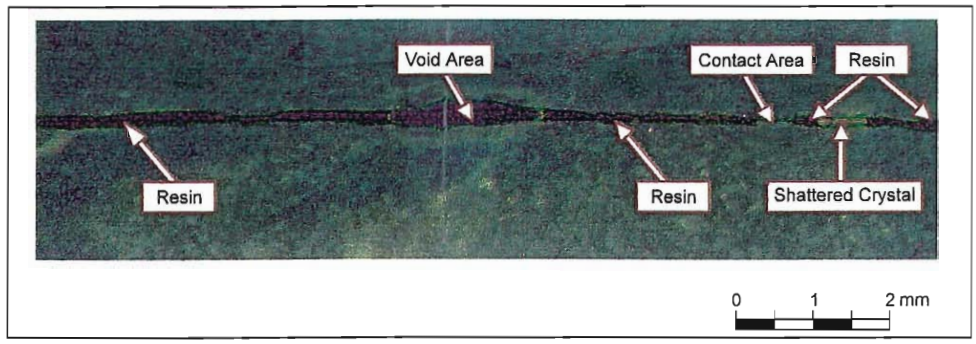

Figure 3-20. Cross section through Limestone sample.

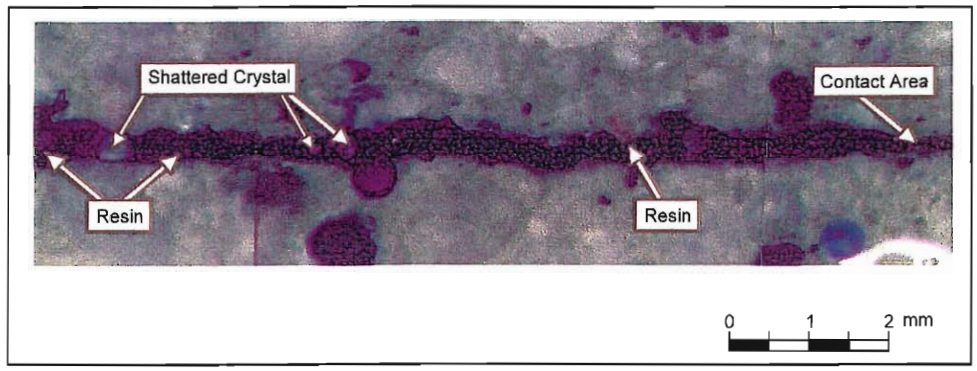

Figure 3-21. Cross section through Concrete sample.

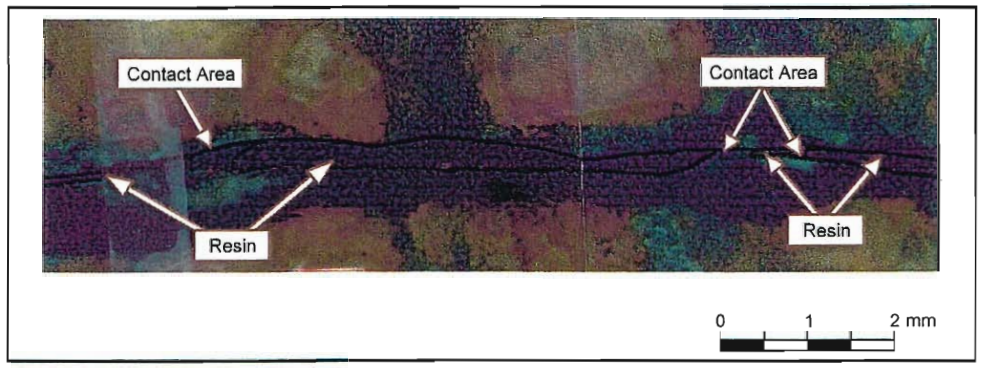

Figure 3-22. Cross section through Äspö No. 1 sample.

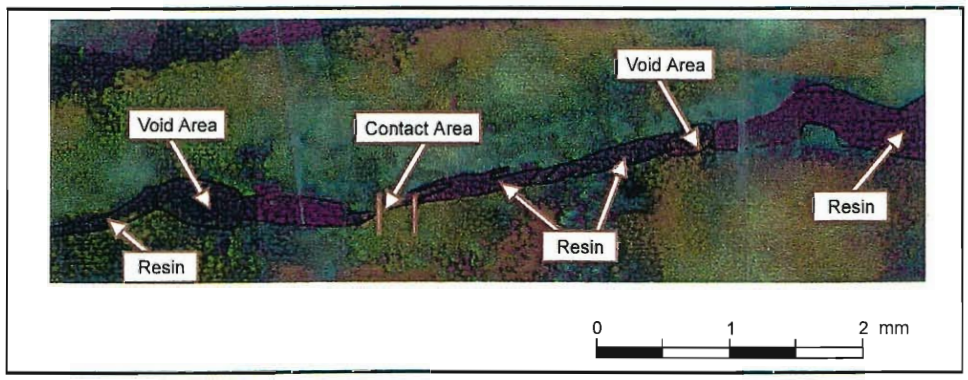

Figure 3-23. Cross section through Äspö No. 2 sample.

The fabricated fracture in the concrete sample (Figure 3-21) exhibits a relatively uniform aperture, with rough walls. In places, the concrete was vuggy or porous and the resin has generally filled the small vugs adjacent to the main fracture. Contact areas are not evenly distributed over the fracture plane.

The cross sections through the two Äspö samples (Figures 3-22 and 3-23), show the more irregular shape of the pore space in these samples of the natural fracture plane samples. Because of the rough and non-planar nature of the fracture trace, these fractures are assumed to have formed by extensional fracturing along an existing vein or old welded fracture surface. The current fracture walls are bounded by a vein-like material (assumed to be primarily epidote) that is more brittle and finer than the host rock, especially in the Äspö No. 1 sample. Examination of the fracture walls showed that, in some places, new fractures or cracks had formed, parallel and criss-crossing the resin filled fracture, in this vein like material. The walls of the fracture pore space are relatively smooth, on the small scale, compared to the concrete sample. However, the section (Figure 3-23) through the Äspö No. 2 sample shows a much more segmented or pocketed pore structure than that shown in the Äspö No. 1 cross section.

3.5 Design and Operation of Degassing Flow System

Figure 3-7b shows the boundary conditions that were used in the degassing experiments. The flow geometry was designed to be essentially linear so that the average fluid velocity would be similar over the fracture plane. However, within the fracture plane the local fluid velocities are expected to vary due to variations in the fracture aperture.

The volume of gas that can be dissolved in water is determined primarily by the fluid pressure, fluid temperature and the gas chemistry or type of gas. For a volume of water that is fully saturated and in equilibrium with a specific gas at a specific pressure, a reduction in fluid pressure will initiate the creation of a separate gas phase which is normally referred to as the gas will begin to evolve. The pressure at which the gas begins to evolve is referred to as the bubble pressure. Developing and maintaining the appropriate gas contents in the fracture pore water and accurately measuring these gas contents at the working pressures is a major challenge in degassing studies. Wahlberg (1995) presented a manual on the design and operation of a tank and pump system for use in injecting gas saturated water into a borehole. Klingberg (1996) discussed the problems and procedures for determining the gas contents and the composition of gas dissolved in waters. The work of both Wahlberg (1995) and Klingberg (1996) have been used in designing the experimental system for saturating the water with gas and determining the gas content at selected pressures (Figure 3-24).

Figure 3-24 shows the basic system that was fabricated to ensure that the water would be well saturated with ether CO_2 or N_2 and that the water could be maintained at pressures above the bubble pressure for that particular gas concentration. This system consists of a 120 litre galvanized tank in which the selected gas was bubbled through a bed of brass shot and marbles, a fluidized bed concept, while a gas cap was maintained at the top of the tank. Saturation at the required percentages of gas normally required about 24 hours.

Percentages of gas, by volume, that would evolve at different pressure steps were determined by flowing the gas saturated water through a clear Plexiglass test unit (Figure 3-24), at different pressure gradients, and measuring the volume of gas that evolved at each pressure step.

Figure 3-25 shows a schematic of the degassing apparatus, the location of the pressure ports/manometers in the fracture plane and an example of the average inlet and outlet water pressures for each part of one of the degassing experiments. In the first step, ie Step 0, the outlet pressure was decreased by only 5 to 10 kPa below the inlet pressure, but still above the bubble pressure, and approximately 10 pore and system volumes of gas saturated water were allowed to flow through the fracture plane to ensure that the fracture plane was completed filled with the gas saturated water. Then the outlet pressure was decreased to three different levels and approximately 15 to 20 litres of gas saturated water were allowed to flow through the fracture plane at each pressure step. Fluid pressures were monitored in each of the manometers and the flowrate was measured at frequent intervals. The temperature of the effluent water was measured using a standard thermometer immersed in the measuring cylinder.

3.6 Effects of Degassing on Measured Fracture Transmissivities

The main thrust of this experimental program was to develop procedures to determine what impact the introduction of a gas phase, into a discrete fracture plane, has on the fracture transmissivity. While gas can be introduced as a separate phase, this applied research program was designed to determine how gas evolving within the fracture plane from a gas saturated water would reduce the fracture transmissivities. In addition, this study examined how fracture roughness or aperture variation changed the observed response of the fracture transmissivity to the gas phase.

Figure 3-26 shows the change in transmissivity as a function of time for the limestone sample for the three main loading cycles (1f, 2a, and 3a). These changes in transmissivity are primarily due to changes in normal stress for cycles 1f and 2a, since the air injection and air invasion tests were conducted at low normal stress and at peak normal stress in cycle 1f and only at peak normal stress in cycle 2a. The erratic changes in measured transmissivity in cycle 1f are due to problems with air bubbles forming in the manometer tubes. The capillary pressure effects of these air bubbles produced fluctuations in the measured pressures and hence in the gradients that were used to calculate transmissivities. In cycles 2a and 3a, the air bubbles were removed from the manometer tubes and only minor perturbations in transmissivity were recorded due to the two-phase flow tests. Even in cycle 3a, when the aperture and the transmissivity had been reduced by the two previous cycles of loading, no major or long term impacts can be detected in the transmissivity versus time curve due to two-phase flow. This observation is consistent with the low trapping capacity that is assumed to be associated with the tabular pore space that is characteristic of the sandblasted sawcut that forms the fracture in this limestone sample.

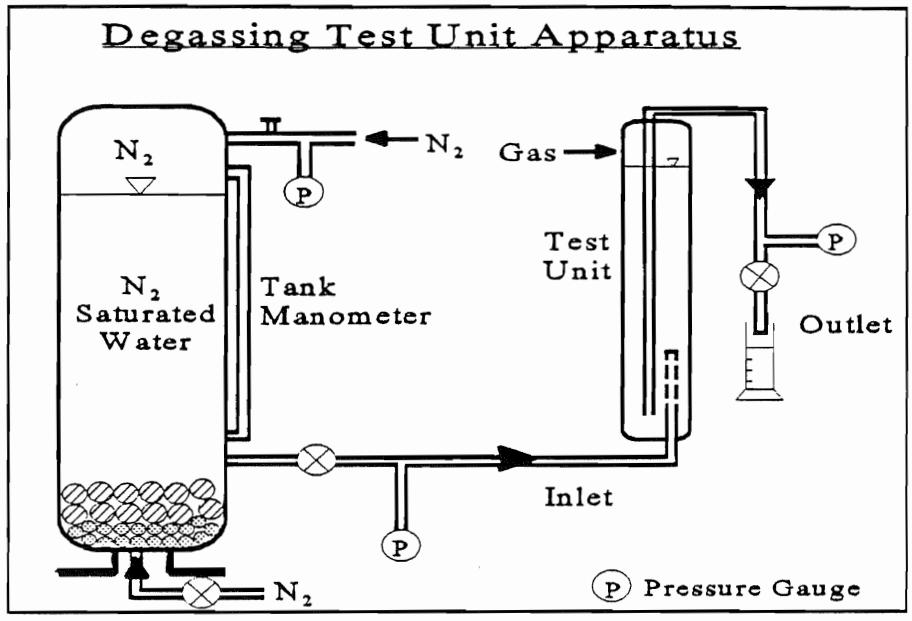

Figure 3-24. Schematic of degassing apparatus used to saturate the water with the selected gas and measure the volume of evolved gas at different pressure gradients.

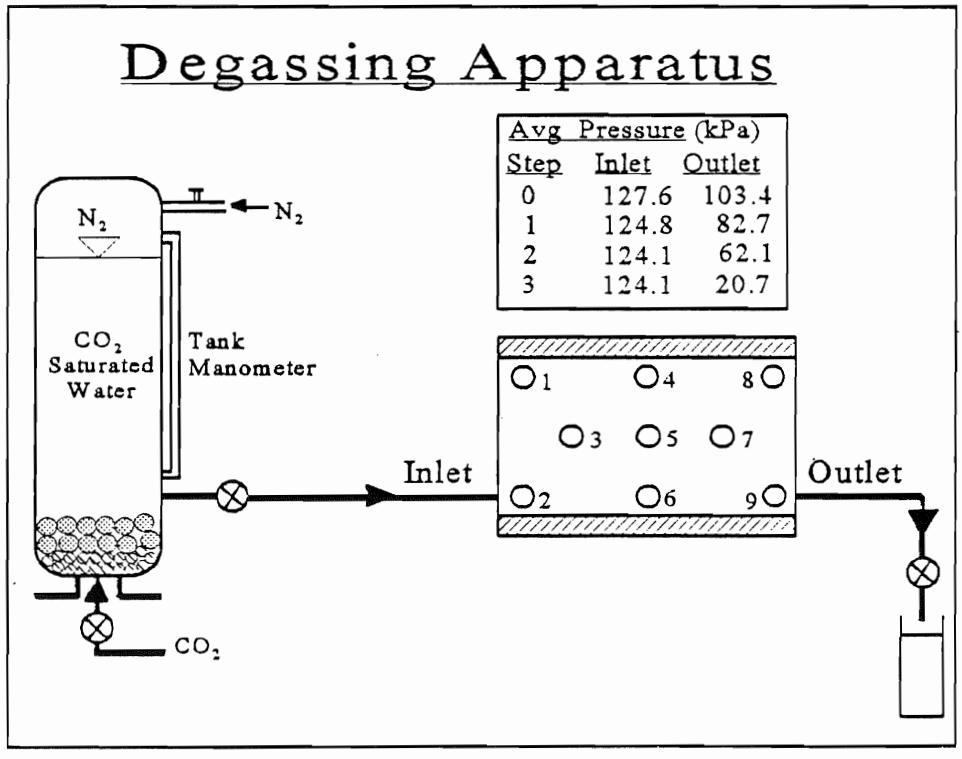

Figure 3-25. Schematic of degassing apparatus and the distribution of manometer ports within the fracture plane, including the average inlet and outlet fluid pressures for each degassing step.

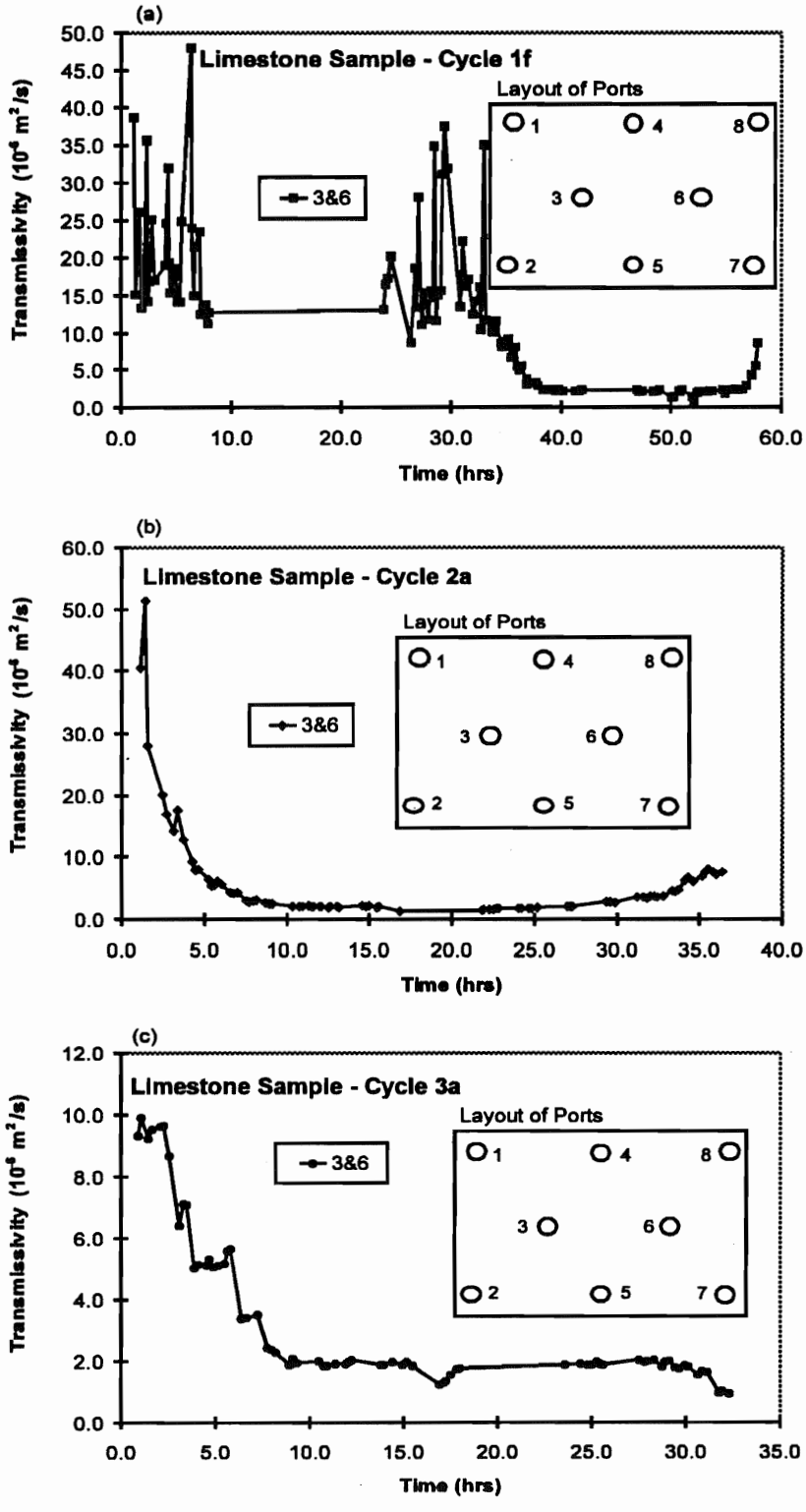

Figure 3-26. Transmissivity changes as a function of time, during normal stress loading cycle (a) 1f, (b) 2a, and (c) 3a, due to changes in normal stress and individual two-phase flow experiments, based on the hydraulic gradients between manometers 3 and 6.

The total test time for the concrete sample was approximately 160 hours for cycle 2a and about 325 hours for cycle 3c. During both of these loading cycles, a range of air invasion and air injection tests using both air, CO_2 and N_2 were completed. For cycle 2a, the fracture transmissivities have been calculated using gradients between two different sets of manometers, Figure 3-27. Since the same flowrate is used to calculate transmissivities in both cases, the variation in transmissivities with time for the various air/gas invasion and injection tests are due to local changes in the gradient. In Figure 3-27a, at approximately 25 hours, the CO_2 invasion experiments appeared to increase the fracture transmissivity. It is possible that the CO_2 flushed residual air pockets out of the fracture plane increasing the single phase fluid transmissivities.

The impact of air injection on fracture transmissivity is obvious from the test that was conducted at 4 MPa of normal stress at approximately 45 hours into the test. In this test air was injected under a low pressure until all of the water had been pushed out of most of the pores in the fracture plane, ie the flowrate versus time curve was essentially flat. Following this air injection, distilled water was injected and a significant reduction in fracture transmisivity, compared to the fracture transmissivity that was measured before the air was injected, was measured using both sets of manometers. The fracture transmissivities for fluid flow were measured at fixed intervals and it required several hours of water injection for the original transmissivities to be recovered. The same pattern was observed for the air injection test, when the sample was loaded to 8 MPa of normal stress, at approximately 93 hours into cycle 2a, (Figure 3-28). Again recovery of the original fracture transmissivities required approximately two to three hours of water injection. A similar response was noted for the air injection and air invasion tests in cycle 3c. Again, the manometer readings in the middle of the sample show that local transmissivities based on local gradients are much more variable than those determined from the more widely spaced manometers that average heads over the full sample length.

Figures 3-29 and 3-30 show the change in transmissivity with time for the two Äspö samples. Note that no air injection tests were performed during cycle 1 on the Äspö No. 1 sample. The abrupt reductions in transmissivity during cycle 2a, Äspö No. 1, correlate with the degassing tests that were conducted at 2, 5 and 10 MPa of normal stress. Figure 3-30 shows the transmissivities versus time from two sets of manometers for Äspö No. 2. On the scale used in these figures, the changes associated with the degassing experiments are not very obvious. However, the results from the degassing experiments on this sample are presented in more detailed figures at the end of this section.

Two different approaches, air/gas invasion and air/gas injection, were used to determine how much water could be removed from the water saturated fracture plane at different levels of normal stress. Air invasion (Figure 3-7b) consisted of closing the upstream injection port and applying a low gas pressure, equal to approximately 200 mm of water head, across the downstream end of the sample with the outlet port open . The volume of water discharged through the outlet or drain port was measured as a function of time. This test is essentially a form of imibibition in which the air or gas is pulled backed into the open fracture pore space by capillary forces which in turn displaces the water in the pore space. By contrast, air injection (Figure 3-7b) pushes the water out of the pore space by applying air or gas pressure, equal to approximately 200 mm of water pressure, on the upstream end of the fracture plane. The volume of water expelled from the

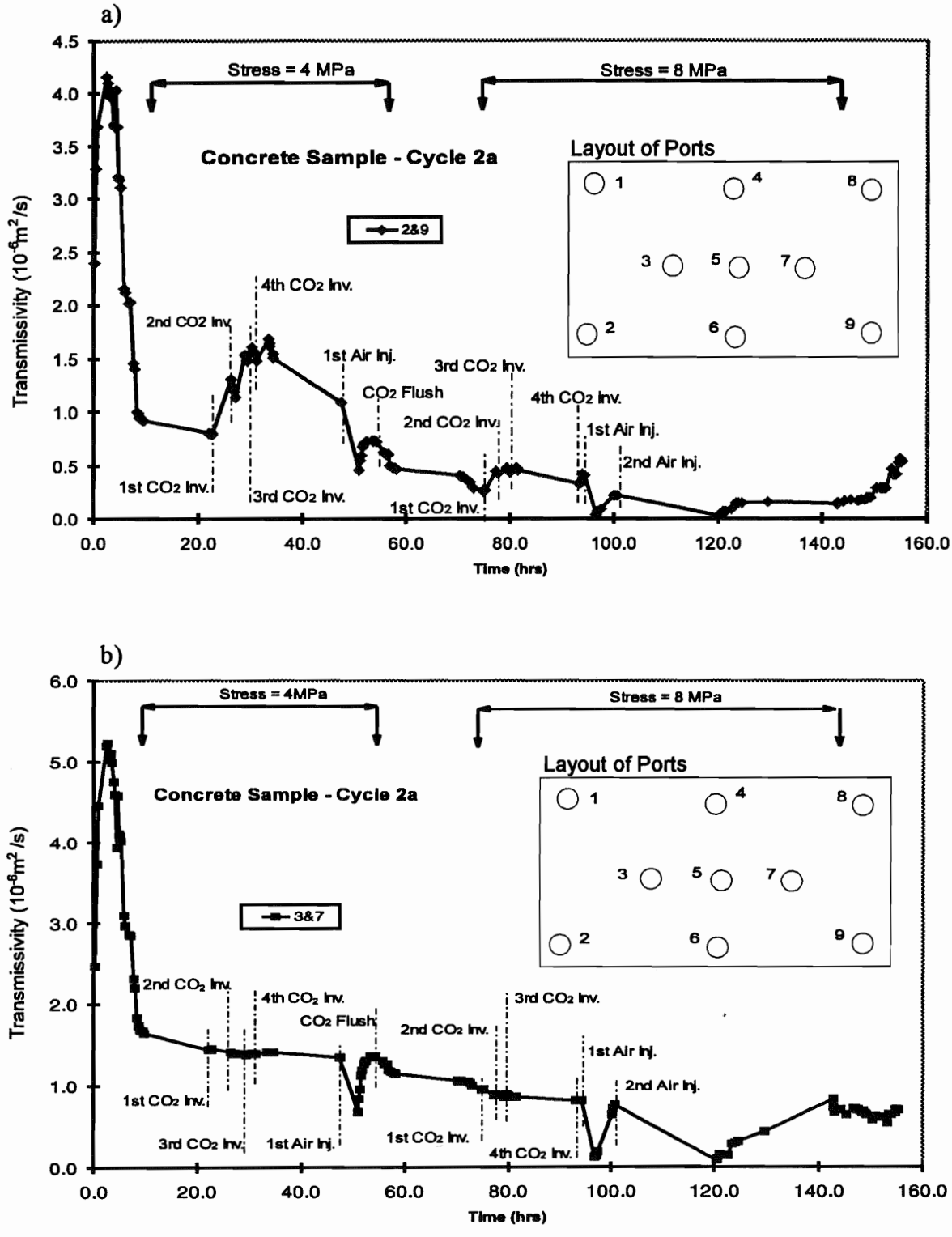

Figure 3-27. Transmissivity changes as a function of time, during normal stress loading cycle 2a, due to changes in normal stress and individual two-phase flow experiments, based on the hydraulic gradients between manometers (a) 2 and 9, and (b) between 3 and 7.

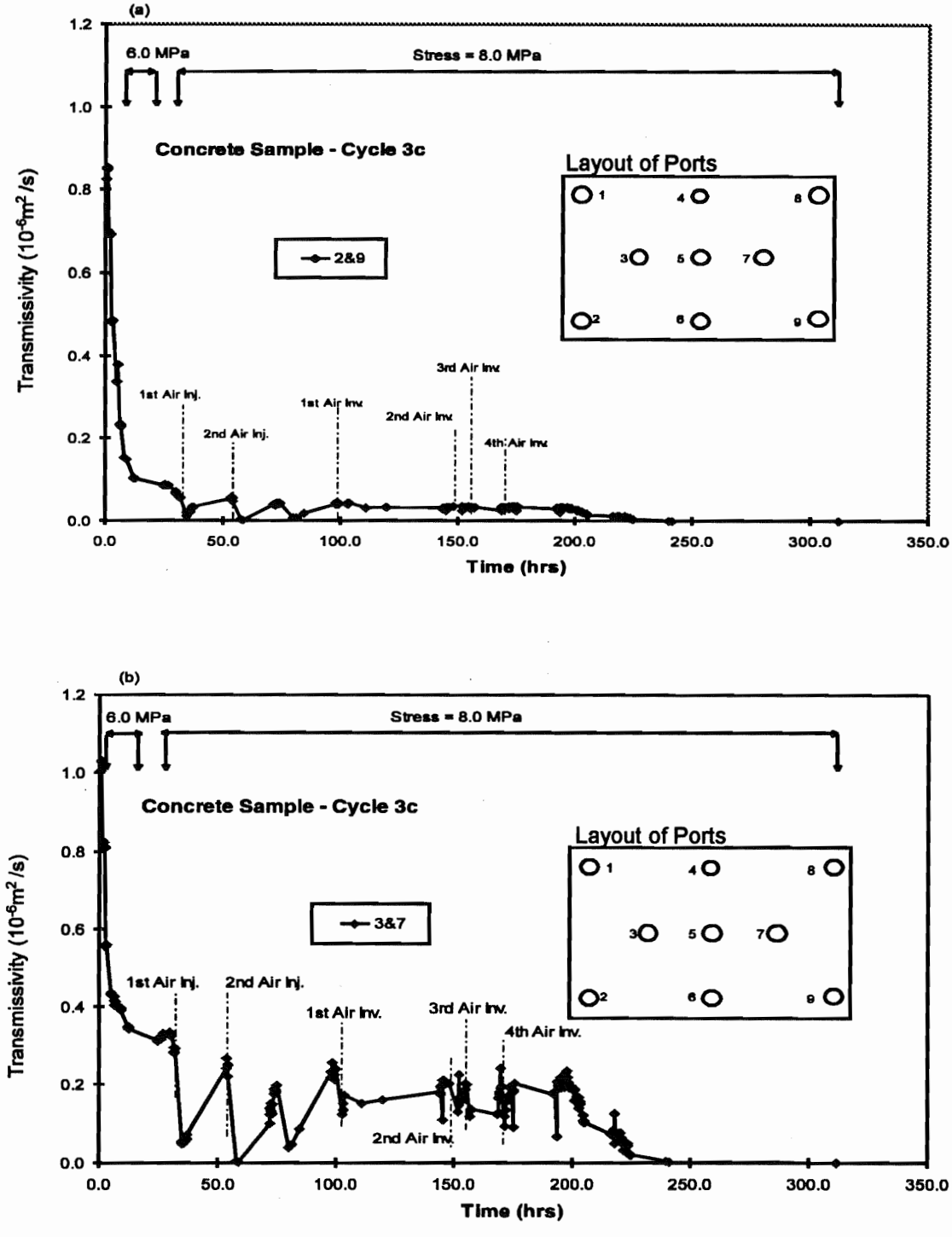

Figure 3-28. Transmissivity changes as a function of time, during normal stress loading cycle 2c, due to changes in normal stress and individual two-phase flow experiments, based on the hydraulic gradients between manometers (a) 2 and 9, and (b) between 3 and 7.

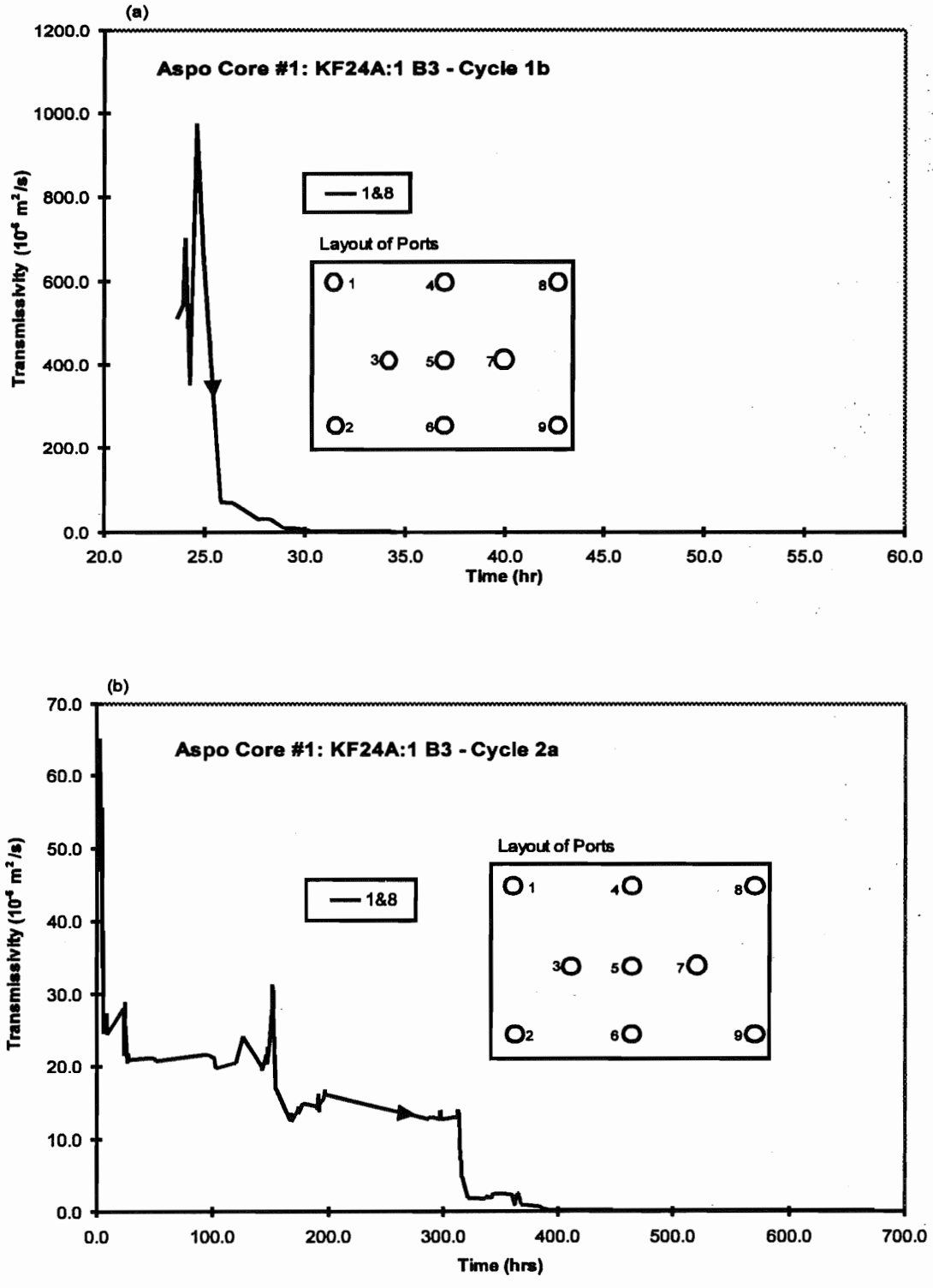

Figure 3-29. Transmissivity changes as a function of time, during (a) normal stress loading-unloading cycle 1b, (b) normal stress loading cycle 2a, due to changes in normal stress and individual two-phase flow experiments, based on the hydraulic gradients between manometers 1 and 8.

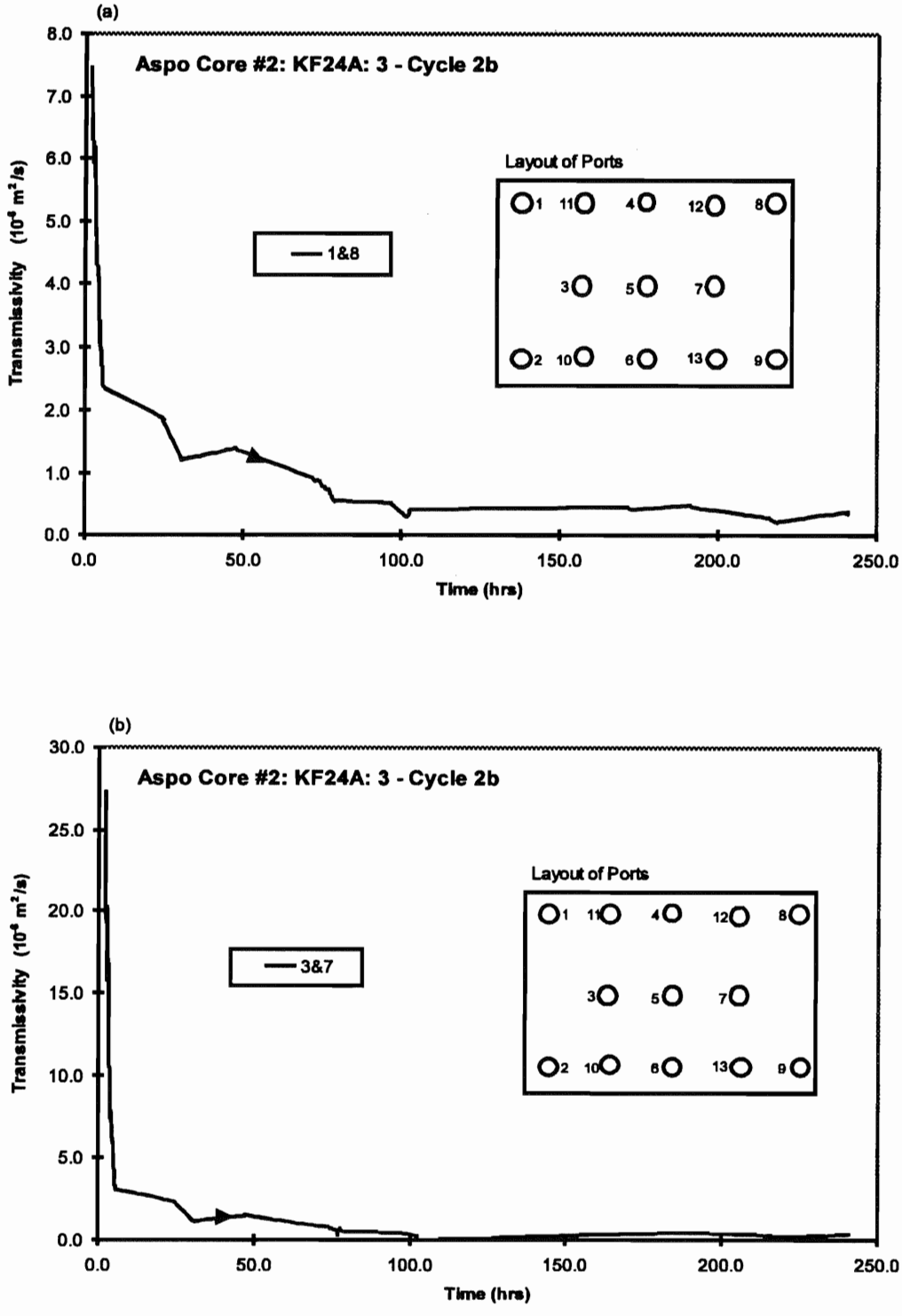

Figure 3-30. Transmissivity changes as a function of time, during normal stress loading cycle 2b, due to changes in normal stress and individual two-phase flow experiments, based on the hydraulic gradients between manometers (a) 1 and 8, and (b) between 3 and 7.

fracture plane at the downstream end of the sample is measured. In the air injection tests, one would expect the water in the small pores to be trapped and the water in the large pores to be expelled, depending on the geometry and orientation of the individual large pores. In some orientations and shapes, one would expect the air or gas to bypass part of the water in the large pores such that part of the water will remain trapped in the fracture pores. Hence the shape of the curve for the volume of water expelled as a function of time should partly reflect the trapping capacity of each fracture plane that is determined by the roughness and structure of the fracture plane.

Figure 3-31a shows the volume of water that was expelled from the limestone sample at 0.1 MPa of normal stress for two different air injections. Single phase flow tests were conducted between the air injection tests. The first part of each of these curves, the near vertical straight line part, represents the water that is displaced from the drain tubes as well as the downstream reservoir and the second part of the curve is assumed to represent the volume of water that is being expelled much more slowly from the fracture pore space. During air injection, water from the upstream reservoir is also forced through the fracture plane and contributes to the volume of water that is represented by the second part of the curve.

Figure 3-31b shows the volume of water expelled from the fracture plane during carbon dioxide invasions at 0.1 MPa. A single phase flow test was completed between the two carbon dioxide invasions. The difference in these two curves is thought to be due to the flushing, during the first test, of air that is trapped in the fracture pore space from the earlier air injection tests. This flushing of air from the large pores increases the volume of water that can be rapidly expelled from the fracture plane in the second test. Figure 3-31c shows that at 6.0 MPa the volume of water versus time curve is essentially the same for three different air injection tests that were conducted for 30 minute test periods. Again, this is consistent with the low trapping capacity of the tabular pore space in this fracture plane indicating that only a small volume of air was retained in the fracture pore space between successive air injection tests. Flushing of the fracture plane with carbon dioxide between air injection tests would have removed any residual trapped air.

Figure 3-31d shows the results of four different carbon dioxide gas invasion experiments on the concrete sample during cycle 2a at 8 MPa. For each test, the total volume of water in the reservoirs, tubes and fracture planes was estimated and used to determine when 25%, 50%, 75% and 100% of this water had been recovered for a particular test. The differences in the curves for the initial part of the curves may be influenced by the amount of gas that may have been trapped in the downstream reservoir. Hence, the slope of the volume versus time curve is assumed to contain the most pertinent information on the response of the fracture plane to the different capillary forces. In Figure 3-31d, the air invasion tests with the smallest percentages of the total volume of water being expelled have the steepest slopes. Figures 3-31e and 3-31f, show the results of air invasion tests at 0.2 MPa and 4.0 MPa for cycle 3a in the concrete sample. The slopes of the curves for the tests at 4.0 MPa are much different than those at 0.2 Mpa.

Figures 3-31g to 3-31l show examples of air/gas invasion and air/gas injection tests for the concrete sample and the two Äspö samples at different levels of normal stress. These test results show that the time required to displace selected volumes of water from a fracture plane in a rough fracture plane such as present in the concrete and Äspö Insert

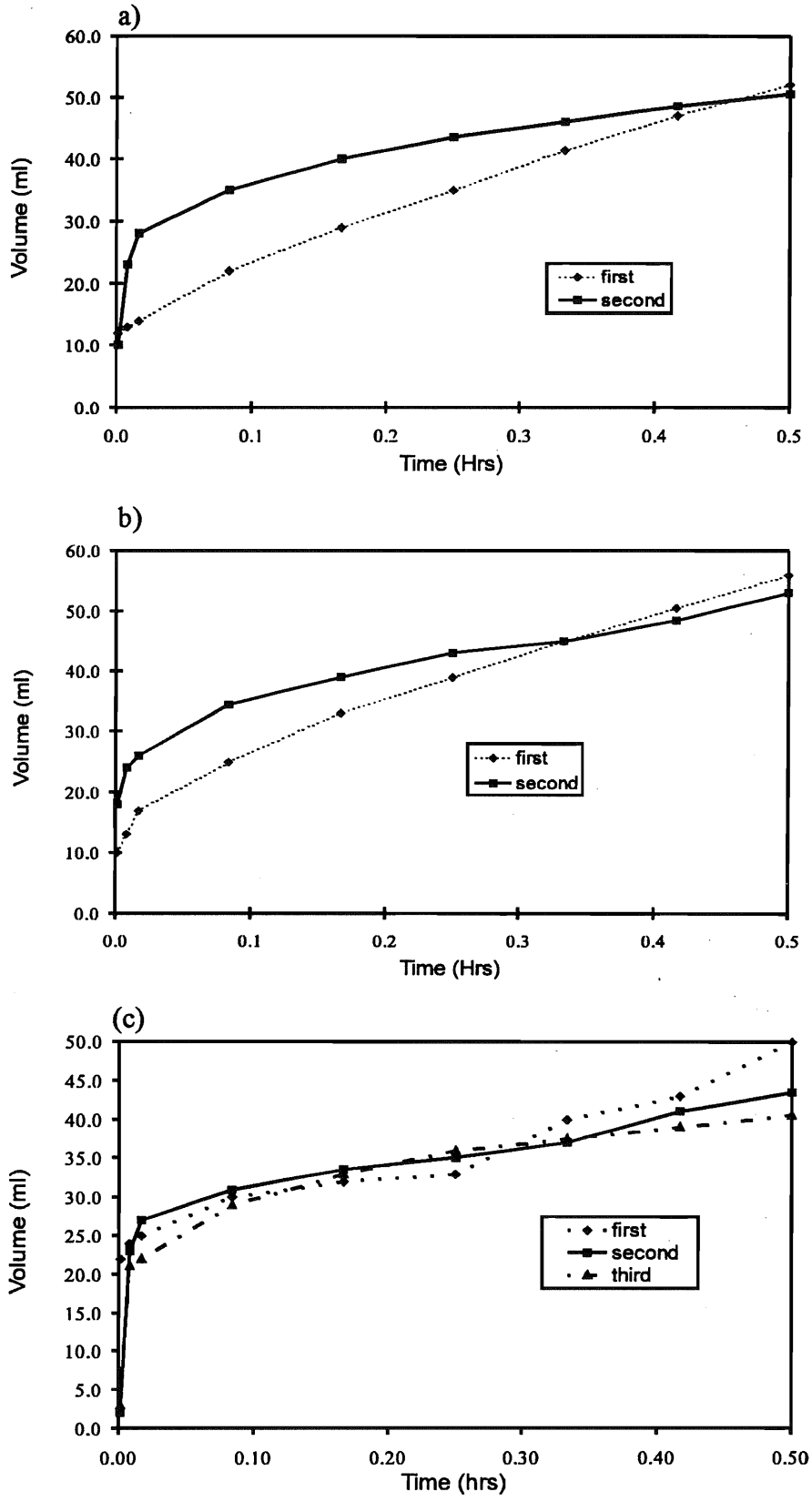

Figure 3-31. Examples of Air/Gas Injection/Invasion at varying stress levels. Limestone Sample, (a) Cycle 1f, air injection at 0.1 MPa, (b) Cycle 1f, carbon dioxide invasions at 0.1 MPa, (c) Cycle 1f, air injection at 6.0 MPa.

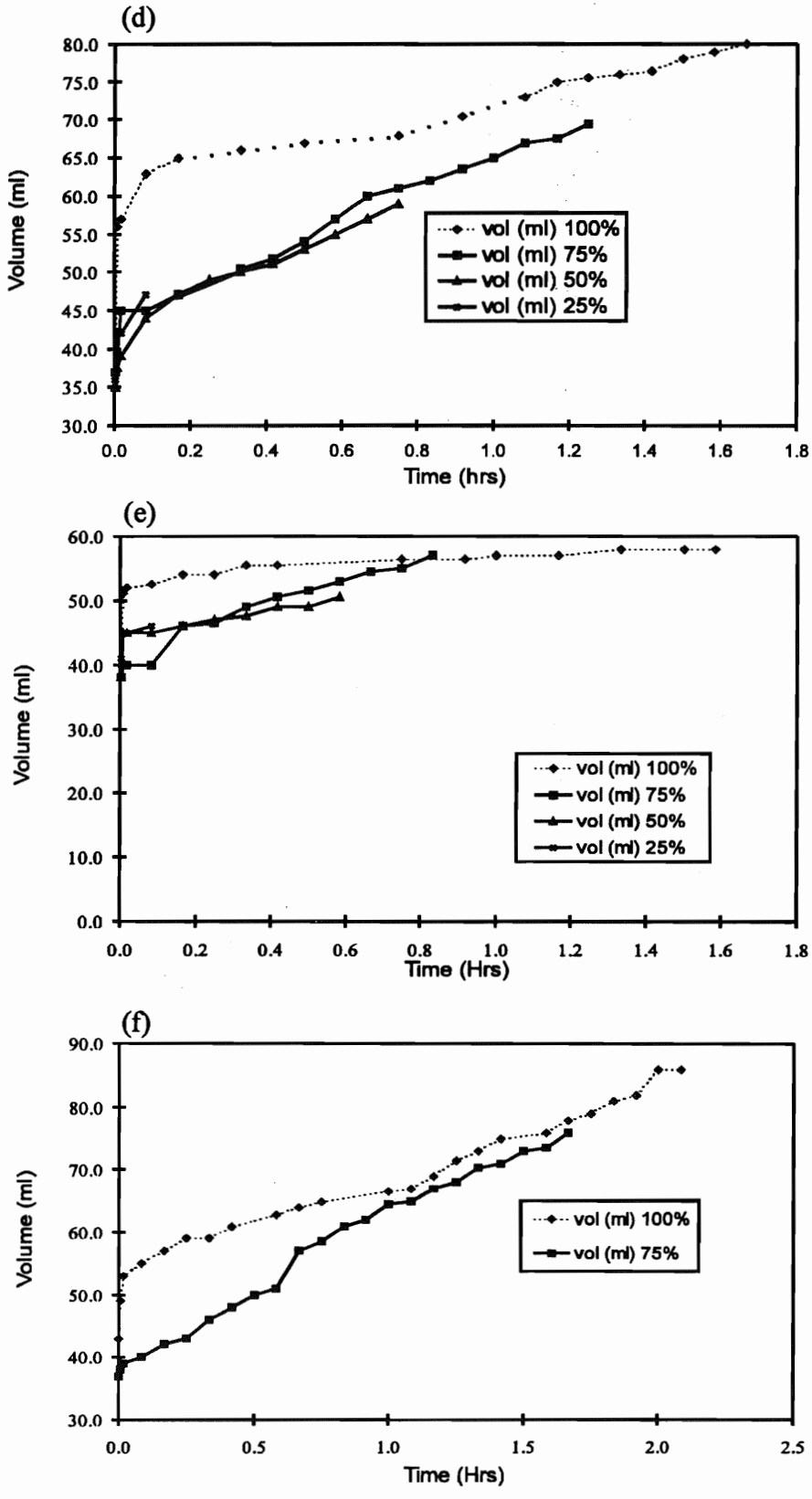

Figure 3-31 cont'd. Examples of Air/Gas Injection/Invasion at varying stress levels. Concrete Sample,(d) Cycle 2a, CO_2 invasion at 8.0 MPa, (e) Cycle 3a, CO_2 invasion at 0.2 MPa, (f) Cycle 3a, CO_2 invasion at 4.0 MPa.

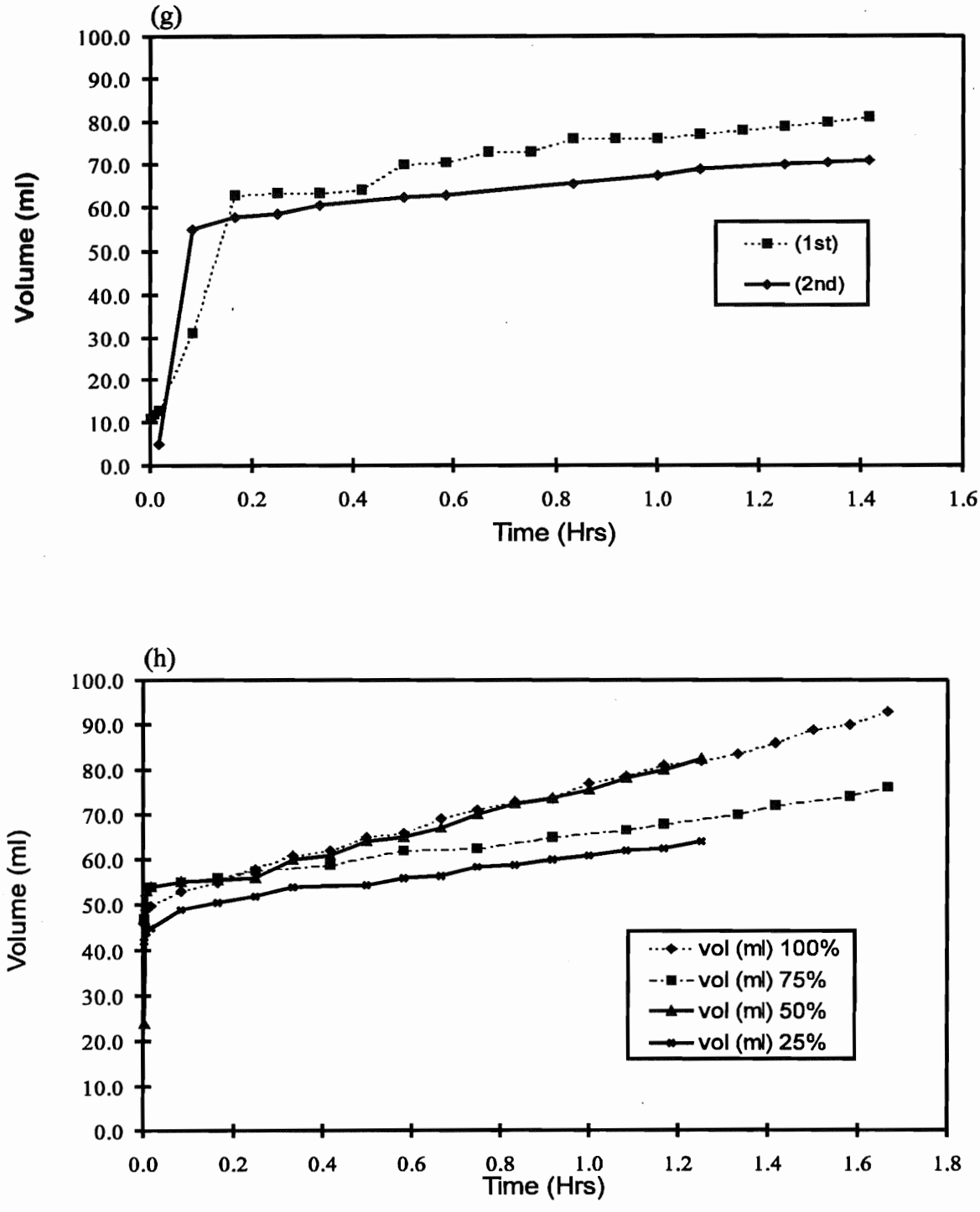

Figure 3-31 cont'd. Examples of Air/Gas Injection/Invasion at varying stress levels. Concrete Sample, Cycle 3c, (g) air injection at 8.0 MPa, (h) air invasion at 8.0 MPa.

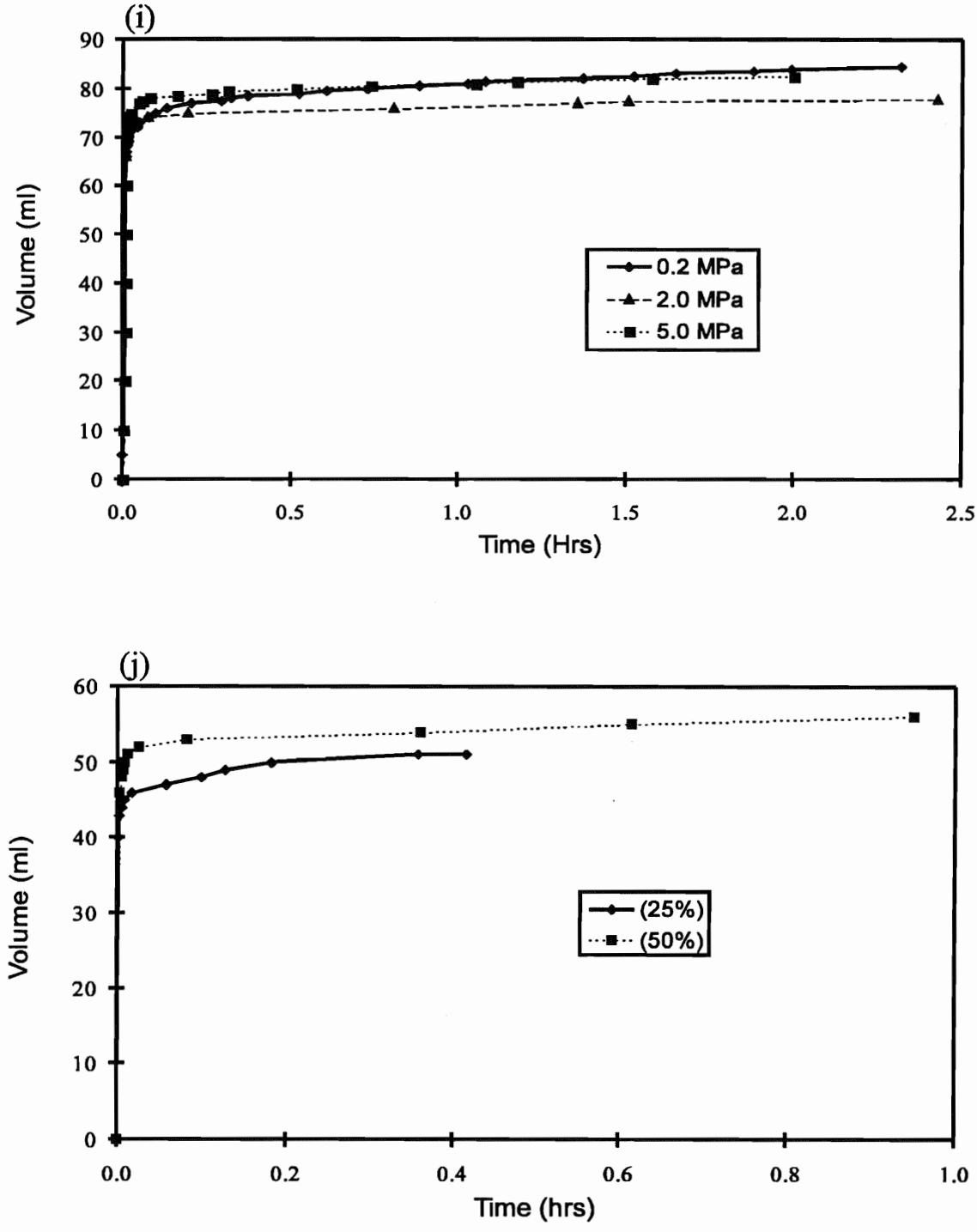

Figure 3-31 cont'd. Examples of Air/Gas Injection/Invasion at varying stress levels. Sample KF24A: 1B3, Cycle 2a, (i) 100% CO_2 Injection, (j) CO_2 Invasion at 0.2 MPa.

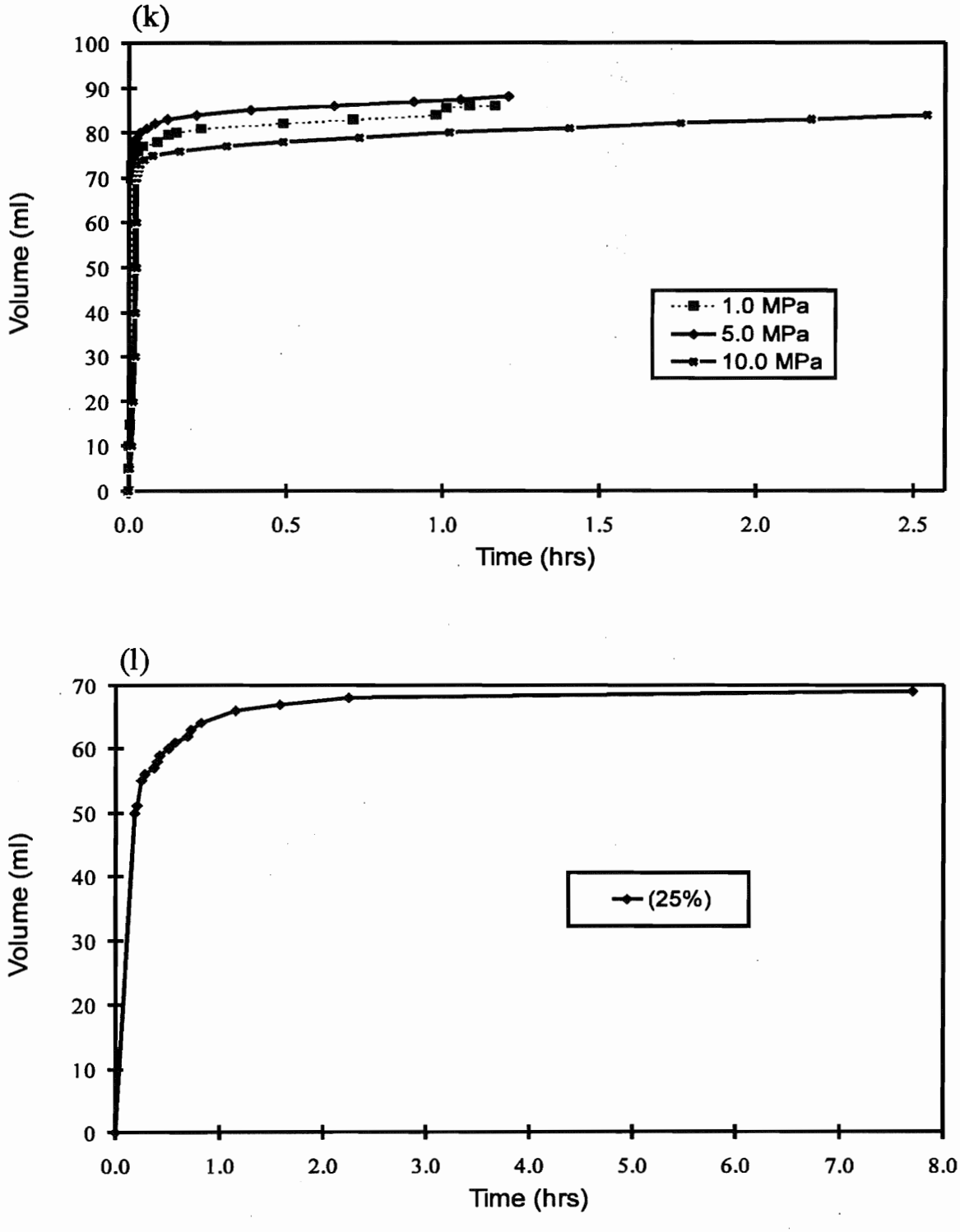

Figure 3-31 cont'd. Examples of Air/Gas Injection/Invasion at varying stress levels. Sample KF24A: 3, (k) N_2 Injection at 1.0, 5.0 and 10.0 MPa, (l) CO_2 Invasion at 2.0 MPa.

samples is approximately four times longer than the time required for similar percentages from relatively smooth and tabular fracture pore spaces such as found in the limestone sample. While the longer times are consistent with the greater trapping capacity of the rough samples versus the smooth limestone sample, it is not clear how these air invasion and air injection curves can be used to derive a relative trapping capacity parameter that could be applied to assessing the impact of degassing on the transmissivity of selected fractures.

Figures 3-32a, 3-32b and 3-32c show the changes in fracture transmissivity with time for three of the degassing experiments using water saturated with carbon dioxide gas, when the Äspö No. 1 sample fracture plane was subjected to 2 MPa, 5 MPa and 10 MPa of normal stress. Note that in all of the degassing experiments on the two Äspö samples the water was fully saturated with the specified gas at the initial background pressure. Dropping the water pressure below this saturation pressure initiated degassing within the fracture plane or within the test system. The initial or saturation pressure for each degassing test is the pressure in metres of water for Port 1 at Step 0 in each of the figures. Figures 3-33a and 3-33b show the changes in fracture transmissivity for the same sample at 10 MPa of normal stress when the injected water was saturated with nitrogen gas. Other than a sudden drop in fracture transmissivity, as suggested by the measured gradients between manometers 1 and 8, at the beginning of step 1, the carbon dioxide degassing appears to have had very little effect on the transmissivity during this test at 2 MPa. Degassing with carbon dioxide at 5 MPa showed an increase in transmissivity during the initial flooding step, followed by a general overall decrease in transmissivity of no more than 25% for both pressure steps as the pressure fell below the bubble pressure. At 10 MPa (Figure 3-32c) the degassing steps with carbon dioxide showed an overall increase at the beginning of the first degassing pressure step, followed by a very gentle decrease of about 10% for the overall three degassing pressure steps. Degassing with carbon dioxide generally showed an oscillating behaviour in the measured fracture transmissivities which might indicate periodic flushing of evolved gas from the fracture plane or capillary pressure effects on the pressure measuring manometer tubes in the sample. When nitrogen gas was used in the degassing experiments at 10 MPa normal stress, the overall gradient between manometers 1 and 8 showed a much greater decrease in fracture transmissivity than that measured for the carbon dioxide degassing, of approximately 50%, when compared to the transmissivities measured at the initial flooding step or step 0. The final pressure step (Figure 3-33b) showed a decrease in transmissivity of more than 50%. In addition, degassing with nitrogen gave much more stable and systematic changes in fracture transmissivity than was obtained with carbon dioxide.

Figures 3-34a, 3-34b and 3-34c show the results of the degassing experiments at 1 MPa, 5 MPa and 10 MPa of normal stress for the Äspö No. 2 sample. At 1.0 MPa, the gas was saturated at a bubble pressure of approximately 29 m of water pressure. The fracture plane was filled with this gas saturated water by flowing with a small gradient for approximately 35 minutes. The downstream pressure was then decreased in three steps to 26.4 m, 20.88 m and 3.146 m of pressure head. Because of the high flowrates, the upstream pressure head could not be maintained above the bubble pressure and part of the decrease in fracture transmissivity is assumed to be due to entry pressure effects from the formation of an evolved gas phase at the upstream boundary. However, the fracture

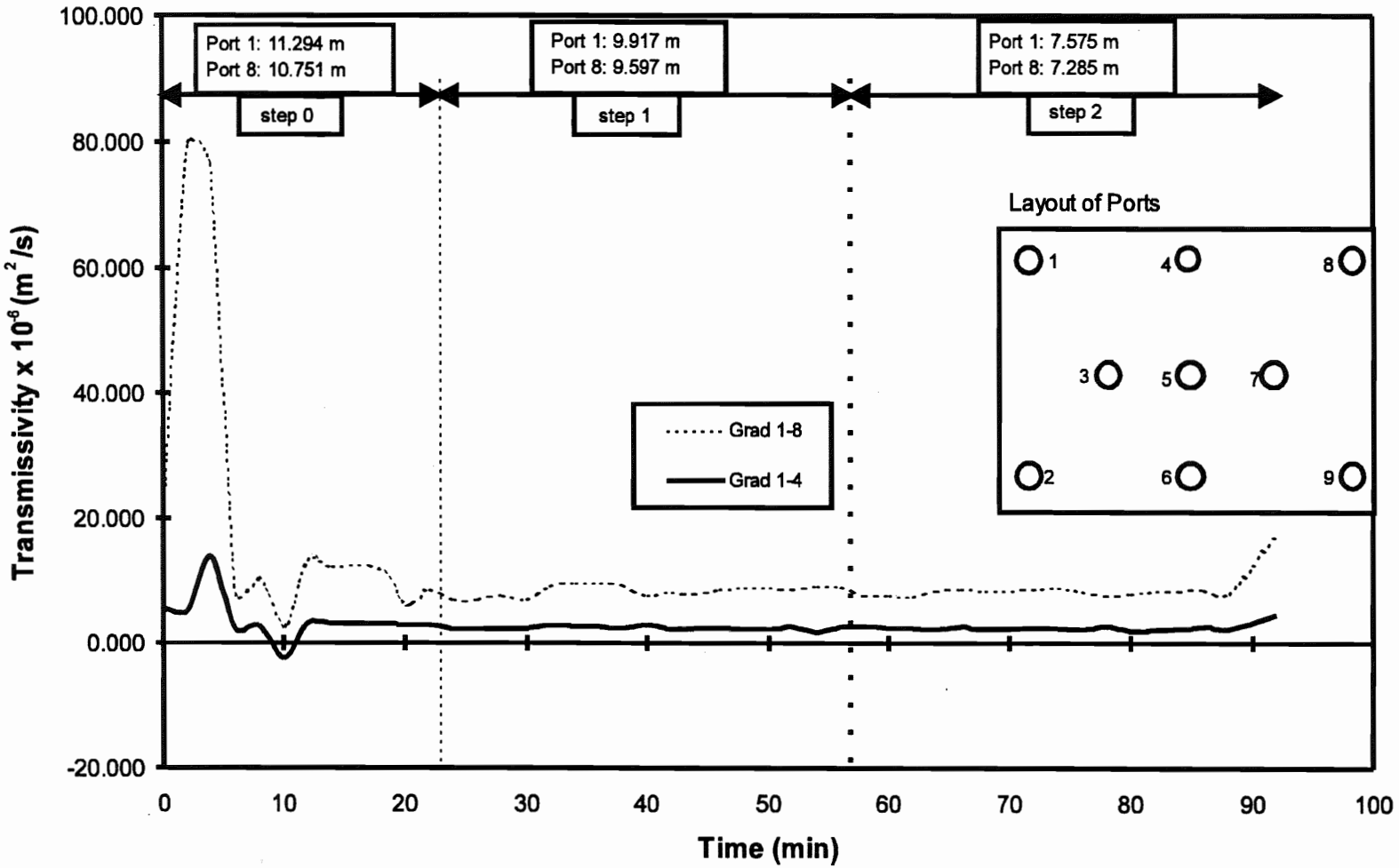

Figure 3-32a. Changes in fracture transmissivity with time for three pressure steps at 2.0 MPa for Äspö Sample #1, KF24A: 1B3, cycle 2a. (Degassing with carbon dioxide gas).

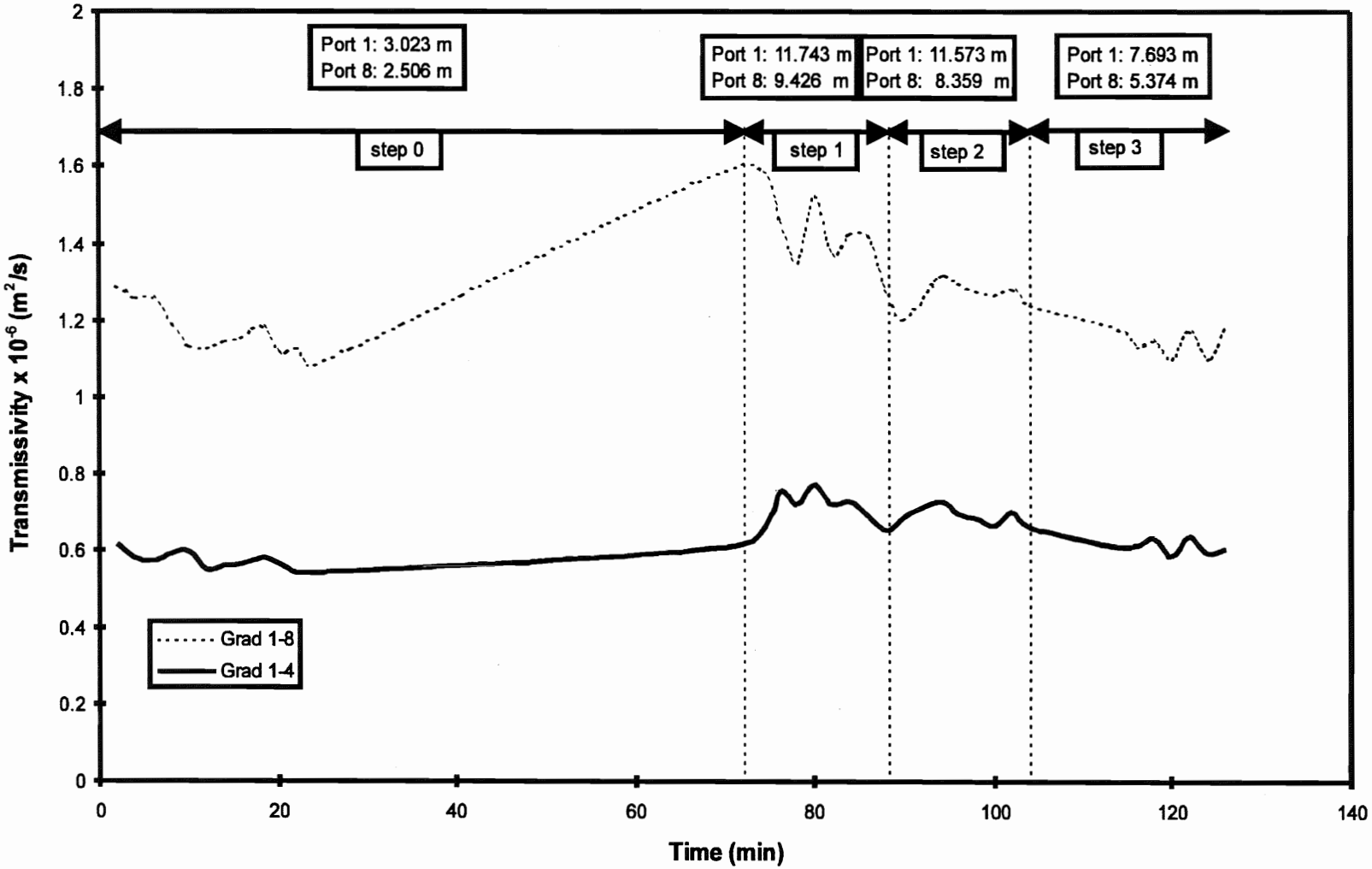

Figure 3-32b. Changes in fracture transmissivity with time for three pressure steps at 5.0 MPa for Äspö Sample #1, KF24A: 1B3, cycle 2a. (Degassing with carbon dioxide gas). See port layout on Figure 3-32a.

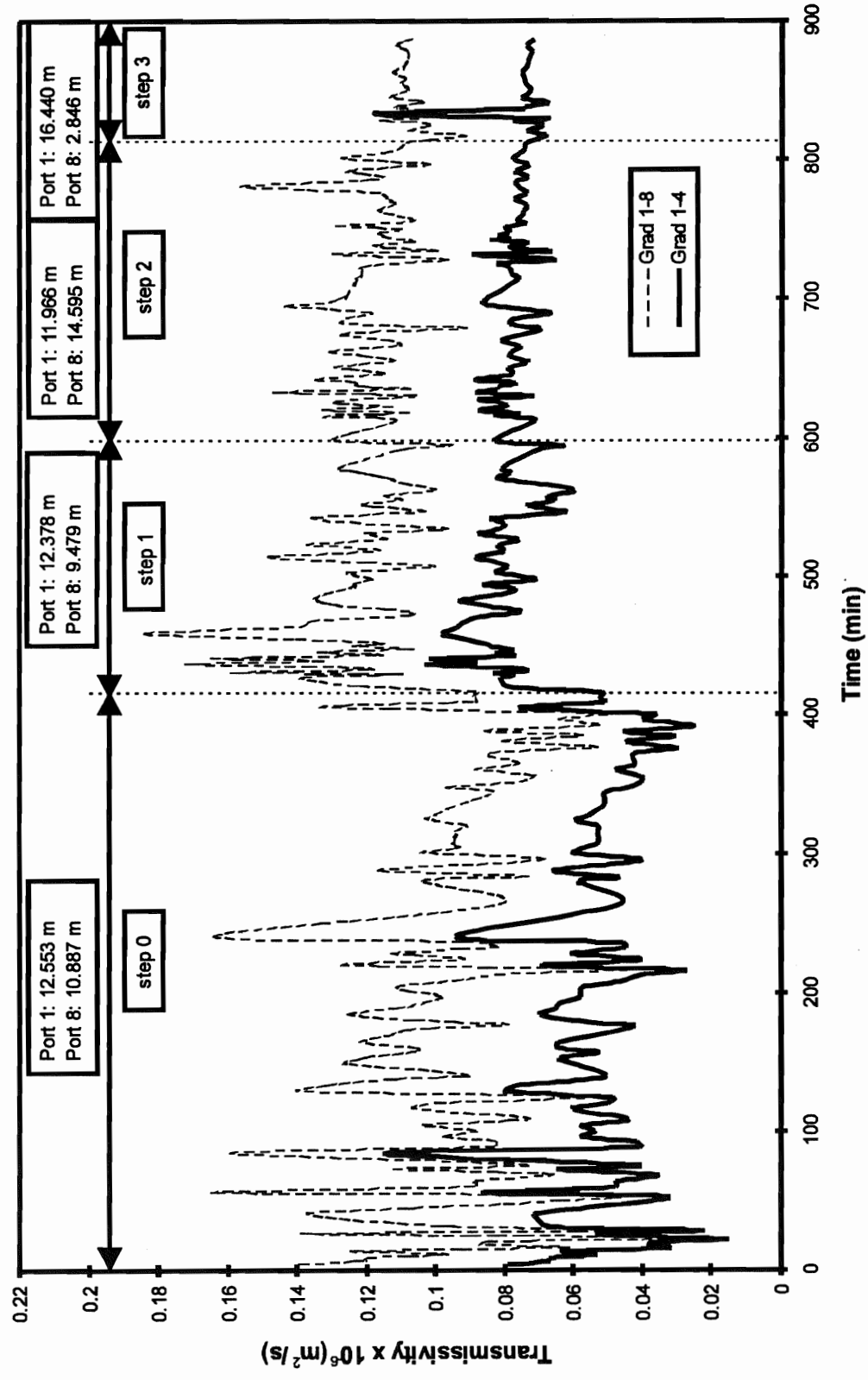

Figure 3-32c. Changes in fracture transmissivity with time for three pressure steps at 10.0 MPa for Äspö Sample #1, KF24A: IB3, cycle 2a. (Degassing with carbon dioxide gas). See port layout on figure 3.32a.

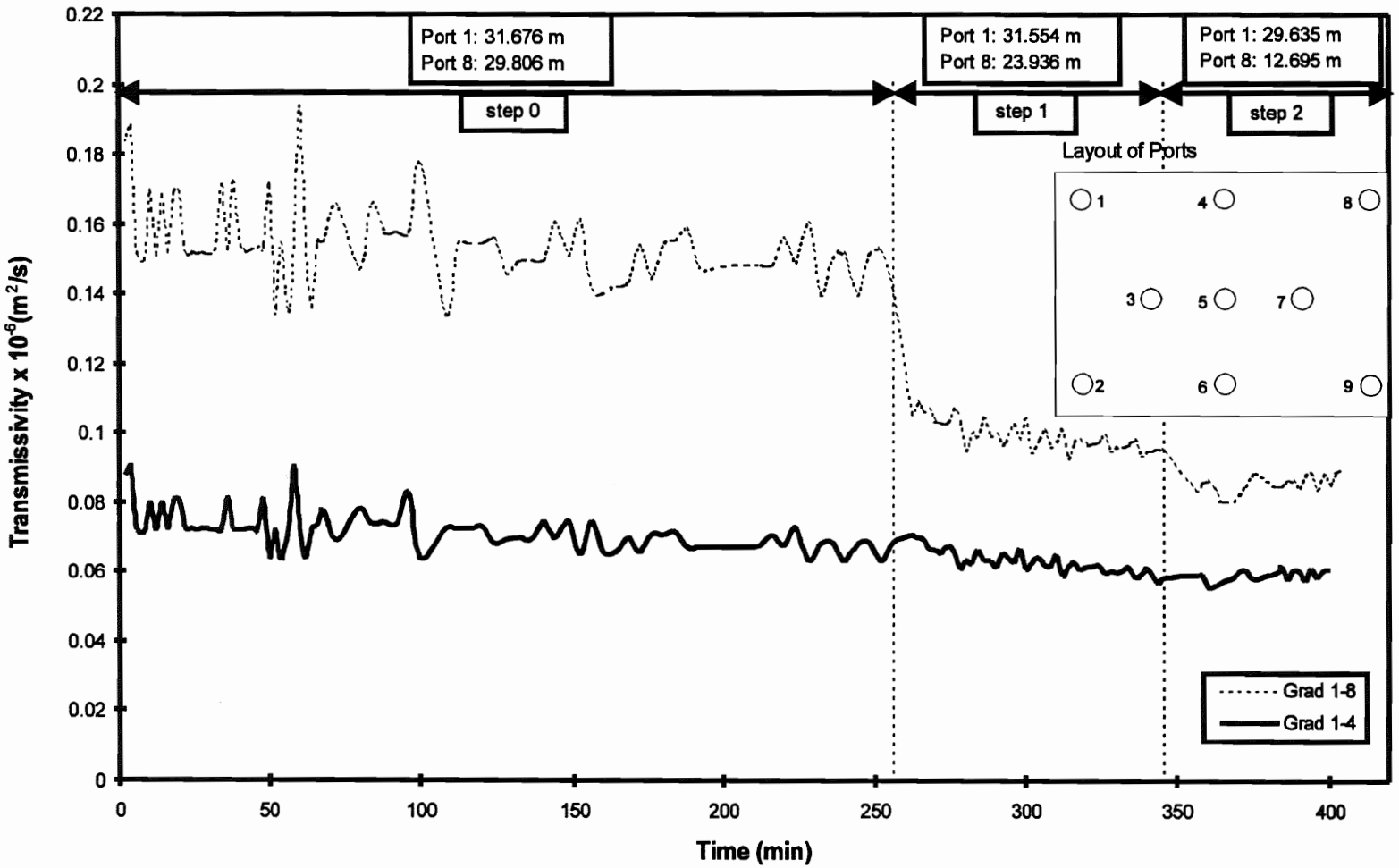

Figure 3-33a. Changes in fracture transmissivity with time for three pressure steps at 10.0 MPa for Äspö Sample #1, KF24A: 1B3, cycle 2a. (Degassing with nitrogen gas).

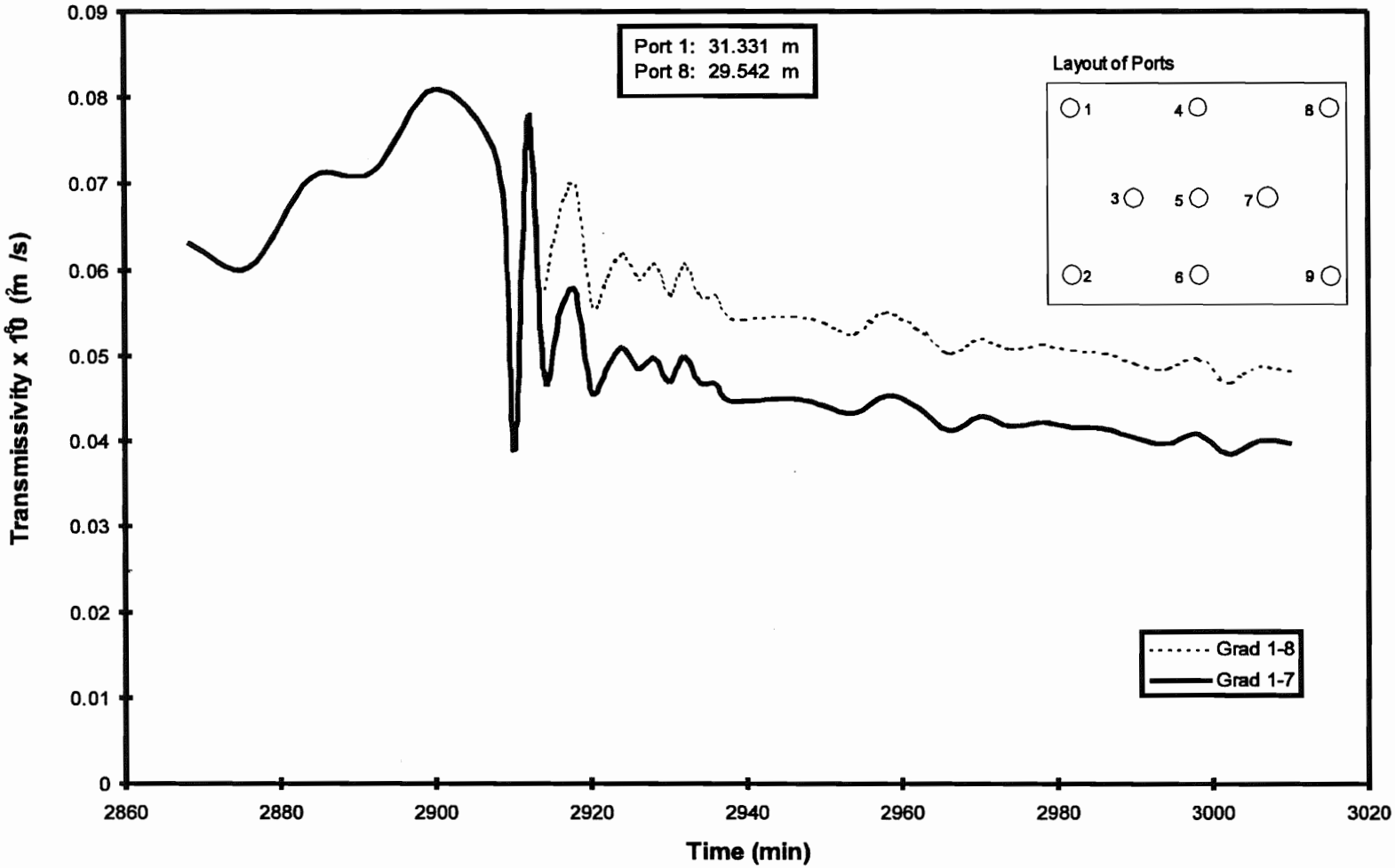

Figure 3-33b. Changes in fracture transmissivity with time for the final pressure step at 10.0 MPa for Äspö Sample #1, KF24A: 1B3, cycle 2a. (Degassing with nitrogen gas).

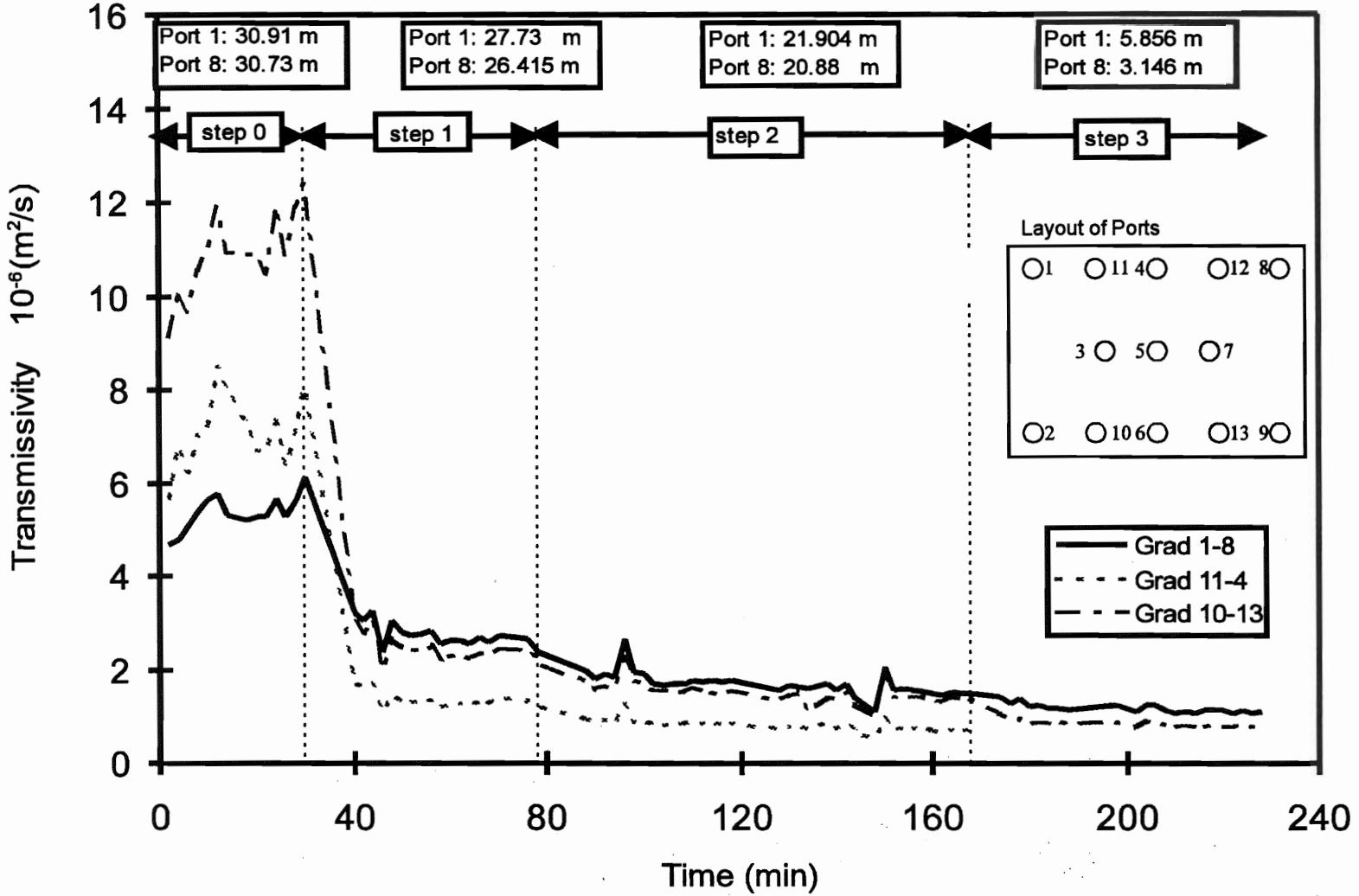

Figure 3-34a. Changes in fracture transmissivity with time for the initial flooding step and the three degassing steps at 1.0 MPa for Äspö Sample #2 KF24A:3. Pressures are shown as metres of water at each port.

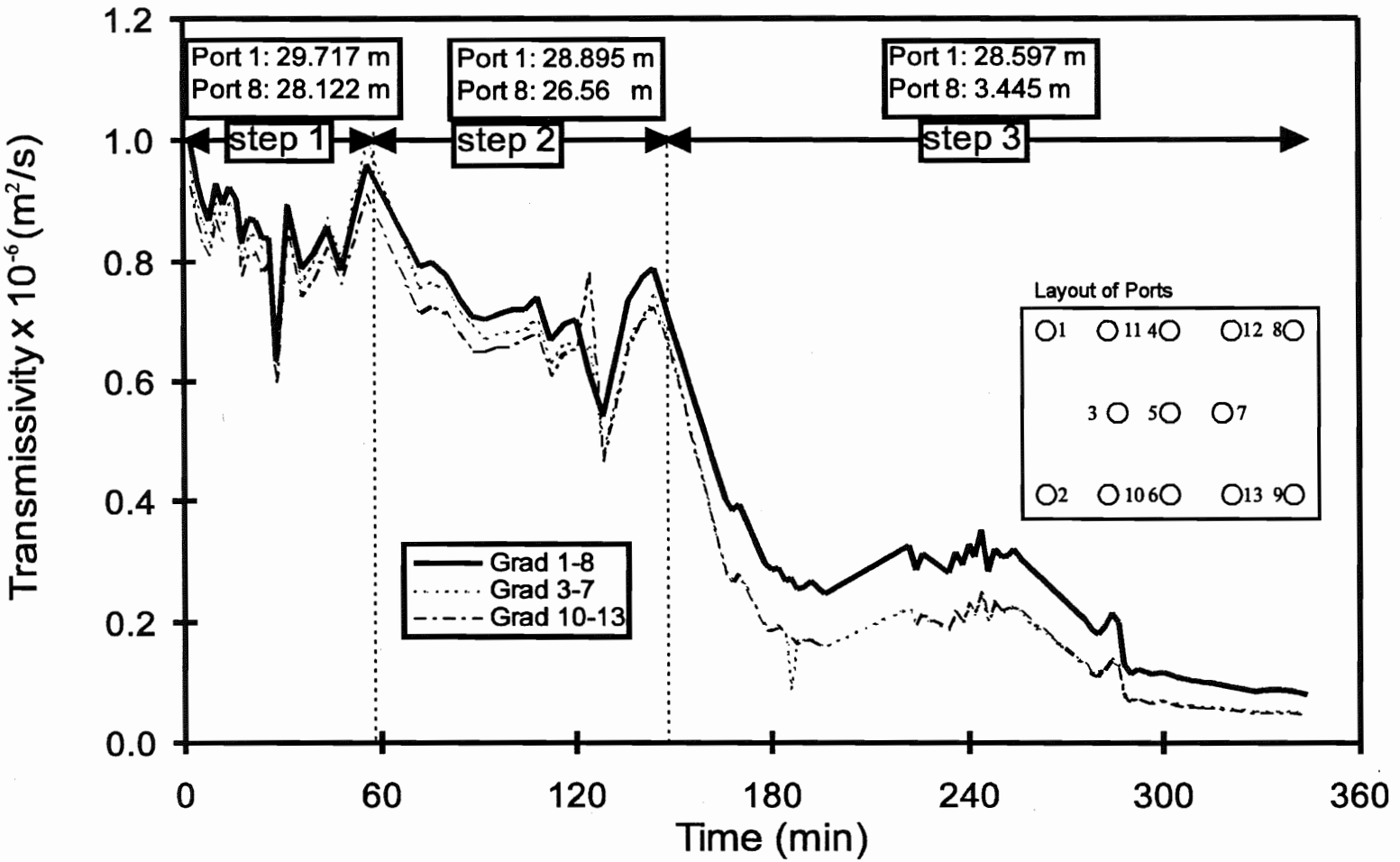

Figure 3-34b. Changes in fracture transmissivity with time for the initial flooding step and the three degassing steps at 5.0 MPa, for Äspö Sample #2, KF24A: 3. Pressures are shown as metres of water at each port.

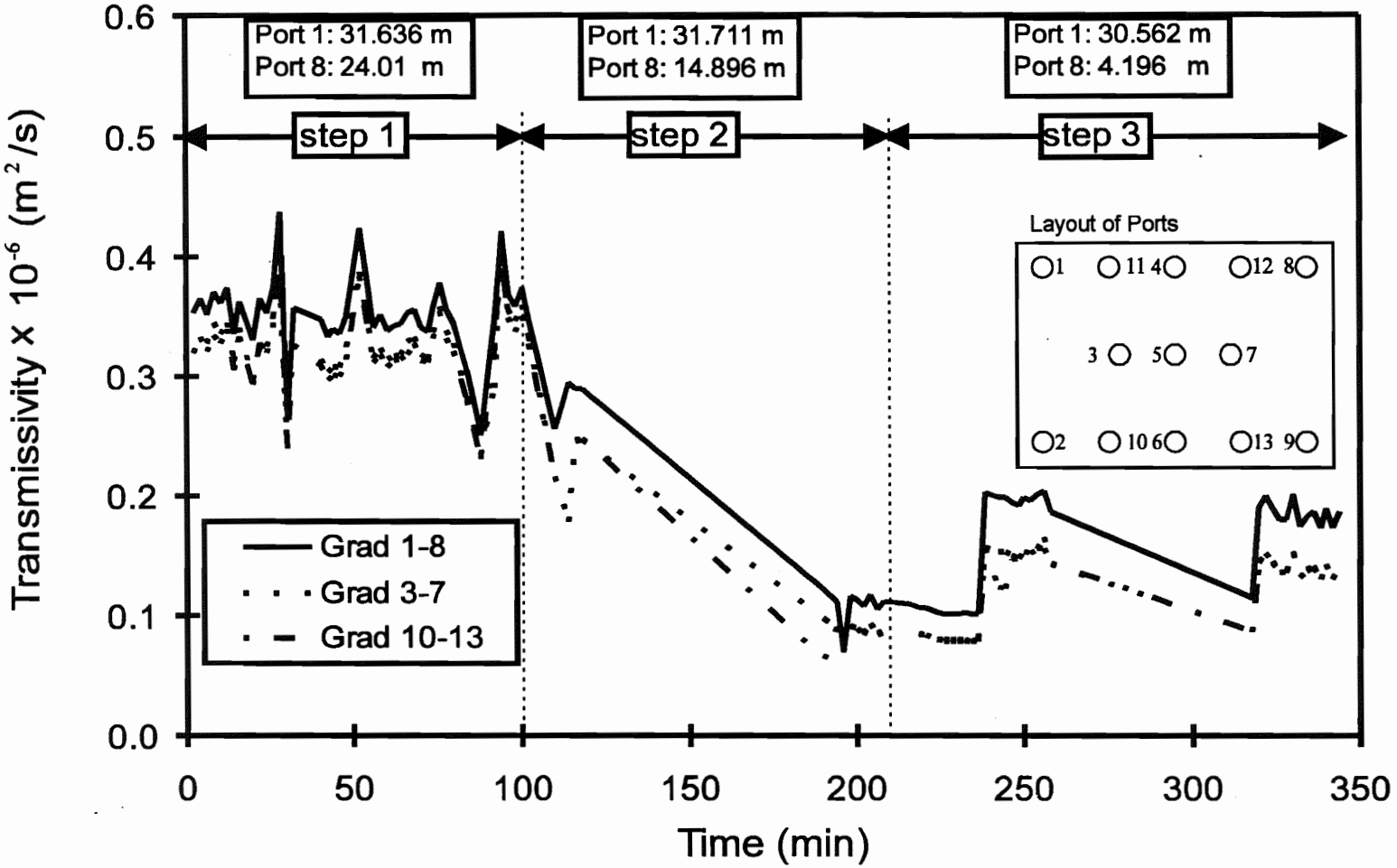

Figure 3-34c. Changes in fracture transmissivity with time for the three degassing steps at 10.0 MPa. for Äspö Sample #2, KF24A: 3. Pressures are shown as metres of water at each port.

transmissivity decreased by approximately an order of magnitude over the 230 minutes of this test.

At 5.0 MPa, the lower flowrates made it possible to maintain the fluid pressures in the upstream reservoir slightly above the bubble pressure, 27 m of pressure head, for all three steps in this experiment. While there is considerable fluctuation in the computed transmissivities, which is thought to be due to the evolved gas being partly expelled or swept from the fracture plane by the flowing water, there is clearly a step-wise decrease of approximately an order of magnitude in the computed fracture transmissivities, based on all three gradient measurements, with time. Note that the volume of the water injection tanks limited the test at these flowrates to approximately 350 minutes making it impossible to determine if the fracture transmissivities would continue to decrease with time as the last step suggests.

For 10 MPa, the bubble pressure was estimated to be approximately 25 m of pressure head. The two steps in which the downstream pressure is assumed to be below the bubble pressure show a clear decrease in fracture transmissivity with time. The sudden increases in transmissivity in the third step are assumed to be due to gas bubbles being expelled or swept from the fracture plane as the fluid velocity increased.

As noted earlier, there is a clear decrease in fracture transmissivity with increase in normal stress. Thus, the degassing experiments on both samples were conducted at different fracture transmissivities. At each normal stress level, the three main pressure steps produced degassing at different flowrates and hence at different fluid velocities. Also, at the first two stress levels for sample 2, degassing reduced fracture transmissivity by approximately and order of magnitude or to about 10% of the original measured fracture transmissivities. The reduction in transmissivity is less for the degassing at 10 MPa, with the reduction being to only about 25% of the original transmissivities. However, this may be less than the reduction that actually occurred since the downstream pressure head during the first step was at or close to the bubble pressure for this test.

Other factors, in addition to the degassing effects, may have contributed to the measured reductions in fracture transmissivity. Factors that need to be evaluated, include the head losses that may have resulted if the fluid velocities produced non-laminar flow or turbulent flow conditions. However, these results, while limited, do show degassing has a major impact on the transmissivity of the fractures used in these experiments.

3.7 Characterization of Fracture Pore Space

3.7.1 General approach

Each sample was sectioned perpendicular to the fracture plane to produce individual profiles to be photographed using a photo-microscope (Figure 3-35). Profiles were cut

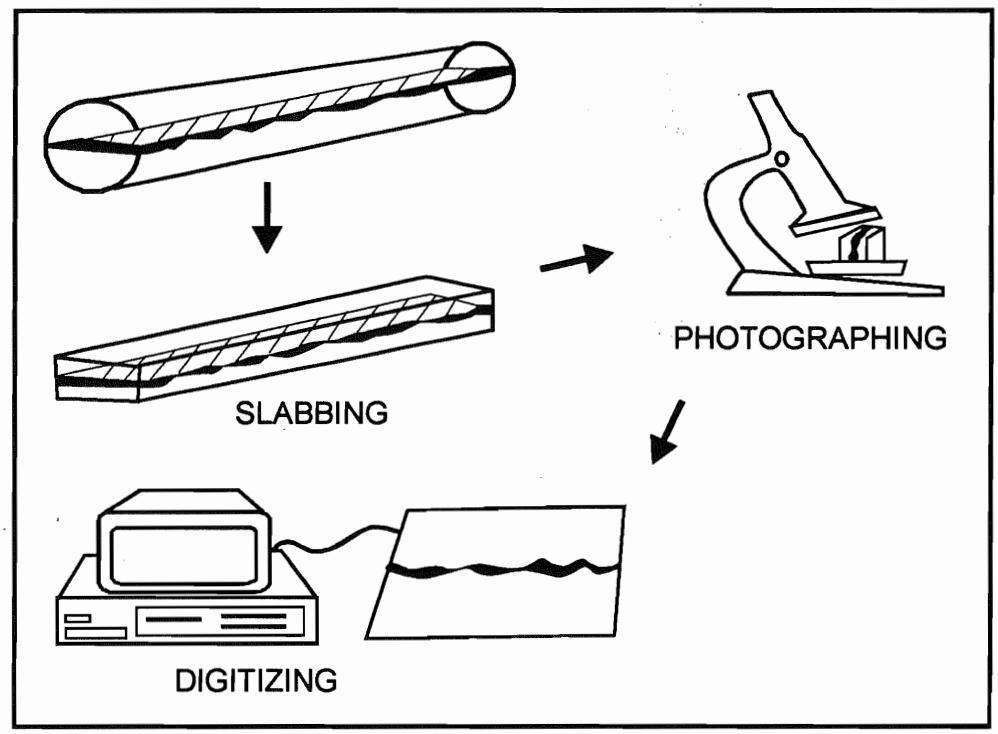

Figure 3-35. Flowchart for pore space characterization work..

perpendicular to the X and/or Y axes of the reference grid established for each sample. Epoxy was applied to the cut surfaces of the slab before additional cuts were made. The fresh side of each sawcut was ground slightly, using a surface grinder to produce a smooth surface for photographing or imaging. Each cross-section was located by reference to the arbitrary grid on the surface of the slab. Each profile was labelled with reference to the quadrant, orientation of the profile and its profile number. For example, profile 1X01 represents the first profile (ie. 01) in the X direction (ie. X) from quadrant 1 of the sample. Location maps of the profiles for the Concrete sample, Limestone sample and Äspö 1, and location map of the profiles for Äspö 2 are shown in Figures 3-36 and 3-37, respectively.

Each profile was viewed under a microscope and a series of photographs were taken along each profile. Each photograph covered about 7 to 8 mm of the fracture length and a 2 to 3 mm section on either side of the fracture plane. The combination of the magnification of the microscope and the enlargement of the area by printing the photograph produced about a 1:18 to 1:20 enlargement of the resin filled fracture plane. The photographs were joined with about a 20% overlap and taped to a paper backing. The top and bottom of each fracture trace, contact points, and areas of resin filling, voids and shattered crystals or broken rock fragments that were filled with resin were then outlined by matching the photograph image with the microscope view. The upper and lower edges of the resin filled fracture plane were digitized by tracing the outlined fracture traces with the mouse of the digitizing tablet. Contact zones, voids (zones that were not filled with resin) and zones of crushed material that were impregnated with resin were digitized and classified separately. The resin thickness and fracture aperture were calculated from the digitized data as the distance from lower edge to upper edge

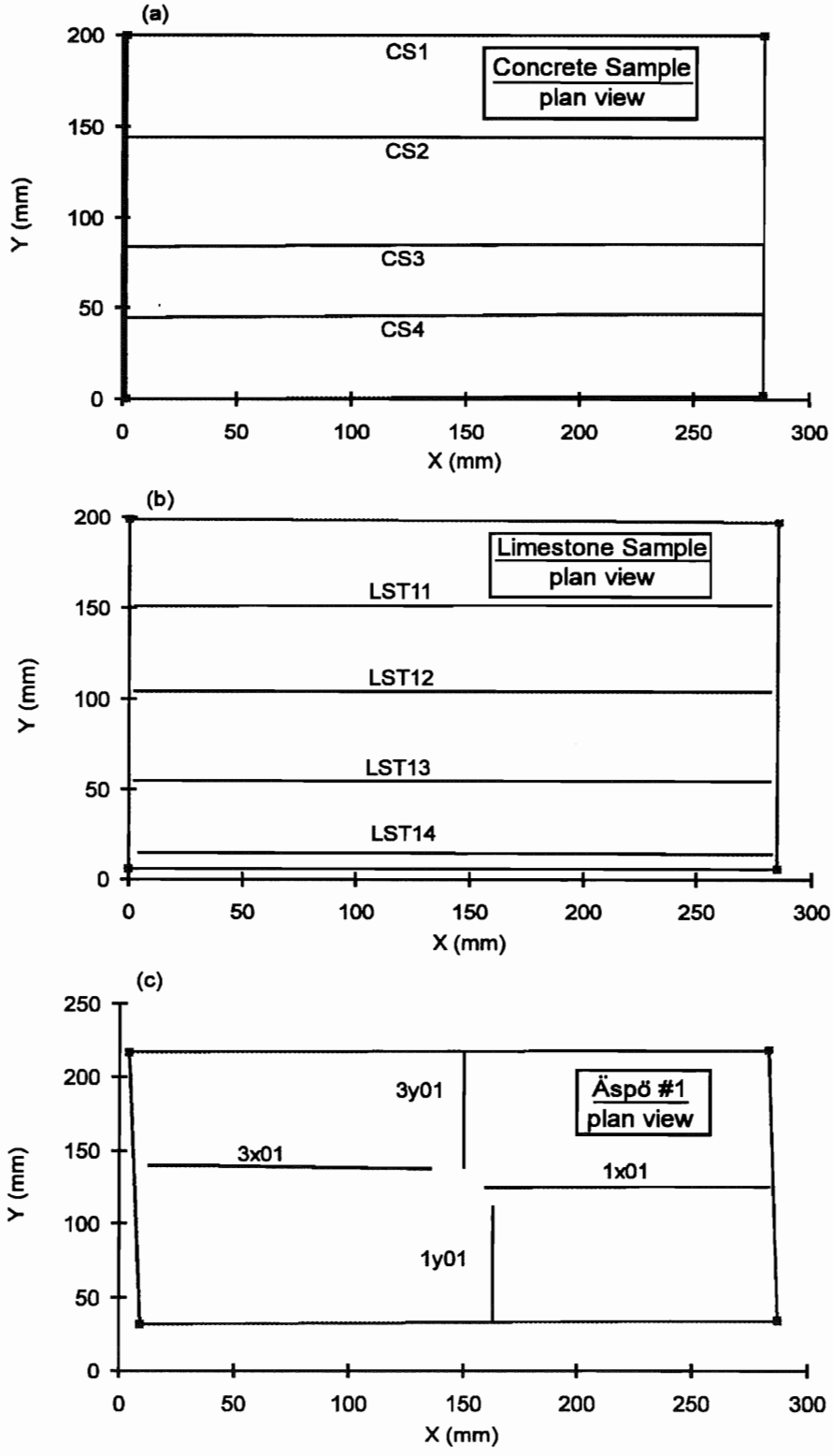

Figure 3-36. Profile location maps of (a) Concrete sample, (b) Limestone sample, and (c) Äspö sample #1.

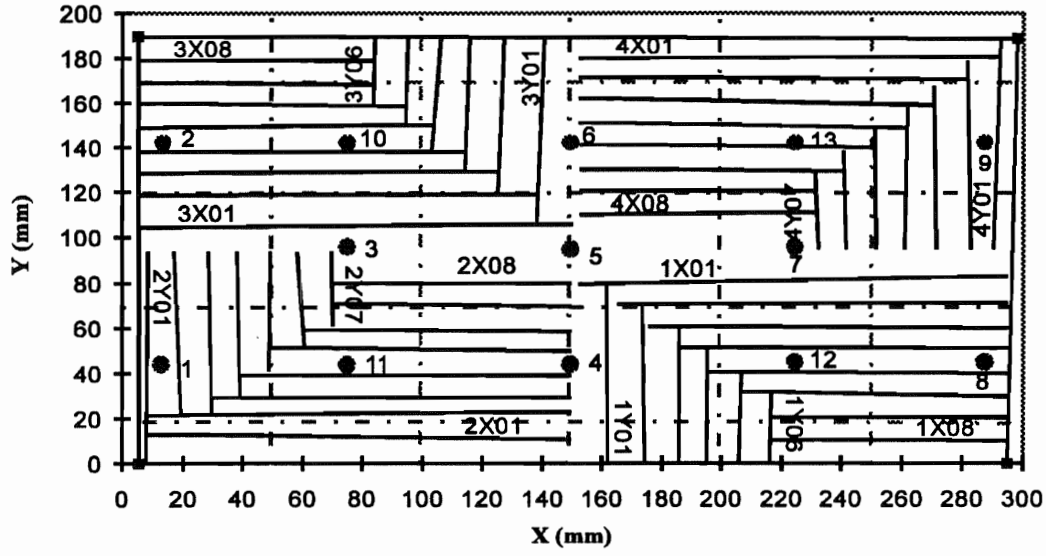

Figure 3-37. Profile location map for Äspö Sample #2.

along each profile. Measurements were calculated successively at points along each profile with a separation between the data points of approximately 0.067-0.07 mm.

3.7.2 Aperture and contact area statistics

The frequency distributions of the measured apertures (mm) of the limestone, concrete and Äspö 1 samples are shown in Figure 3-38 and the Äspö 2 distributions are shown in Figure 3-39. The total number of data points, mean and median aperture, standard deviation, coefficient of variation, maximum and minimum, aperture, and upper and lower quartiles are plotted along the sides of each histogram. The statistics on the pore space of these four samples are summarized in Table 3-1. All four samples have high percentages of contact points. Figure 3-40 shows the distribution of contact points for the Äspö 2 sample.

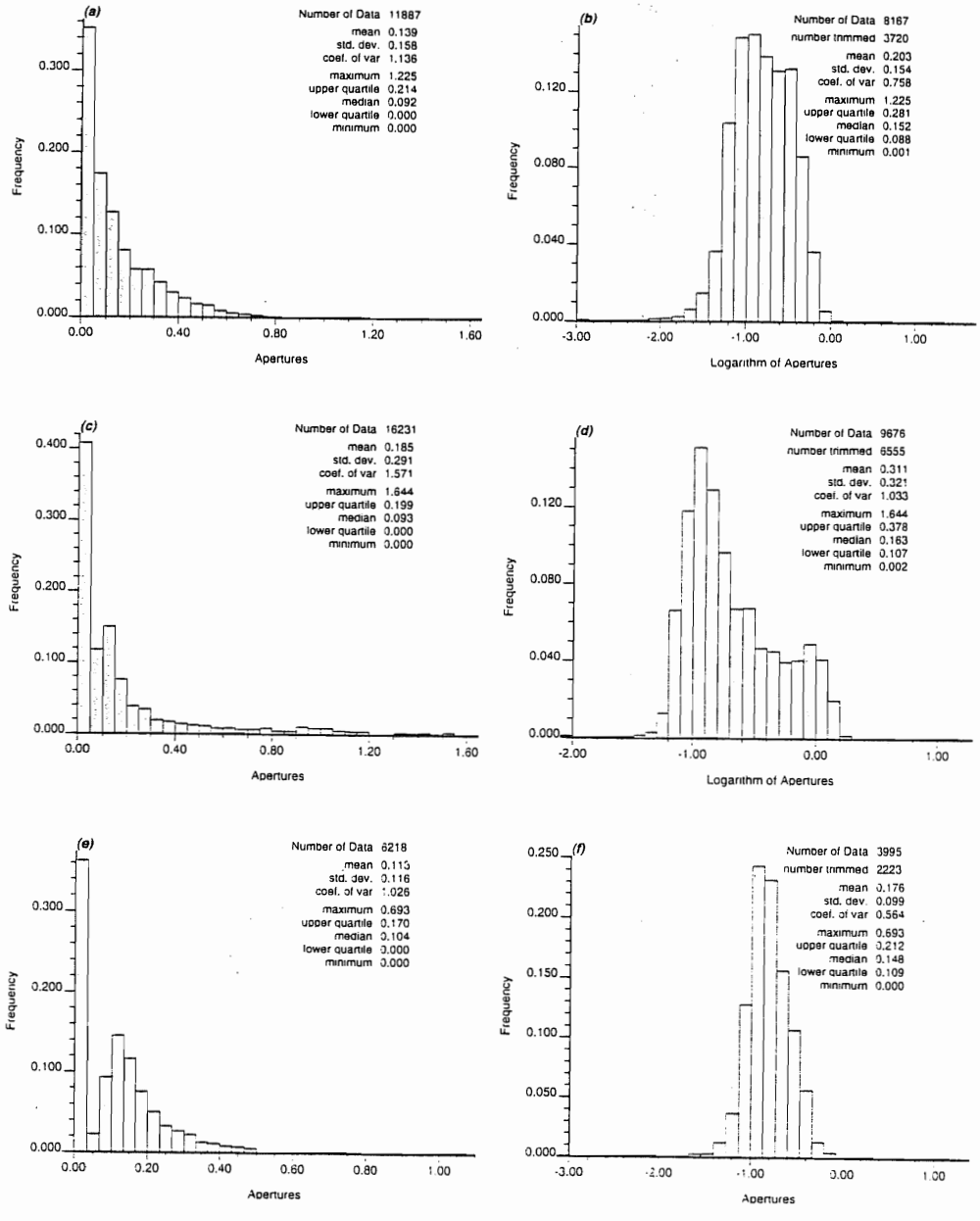

Figure 3-38. Histograms of Concrete sample showing (a) the aperture (mm) distribution and (b) logarithmic aperture distribution; Limestone sample showing (a) aperture (mm) distribution and (d) logarithmic aperture distribution; Äspö Sample #1 showing (e) aperture (mm) distribution and (f) Logarithmic aperture distribution. For aperture distributions, contact areas are included.

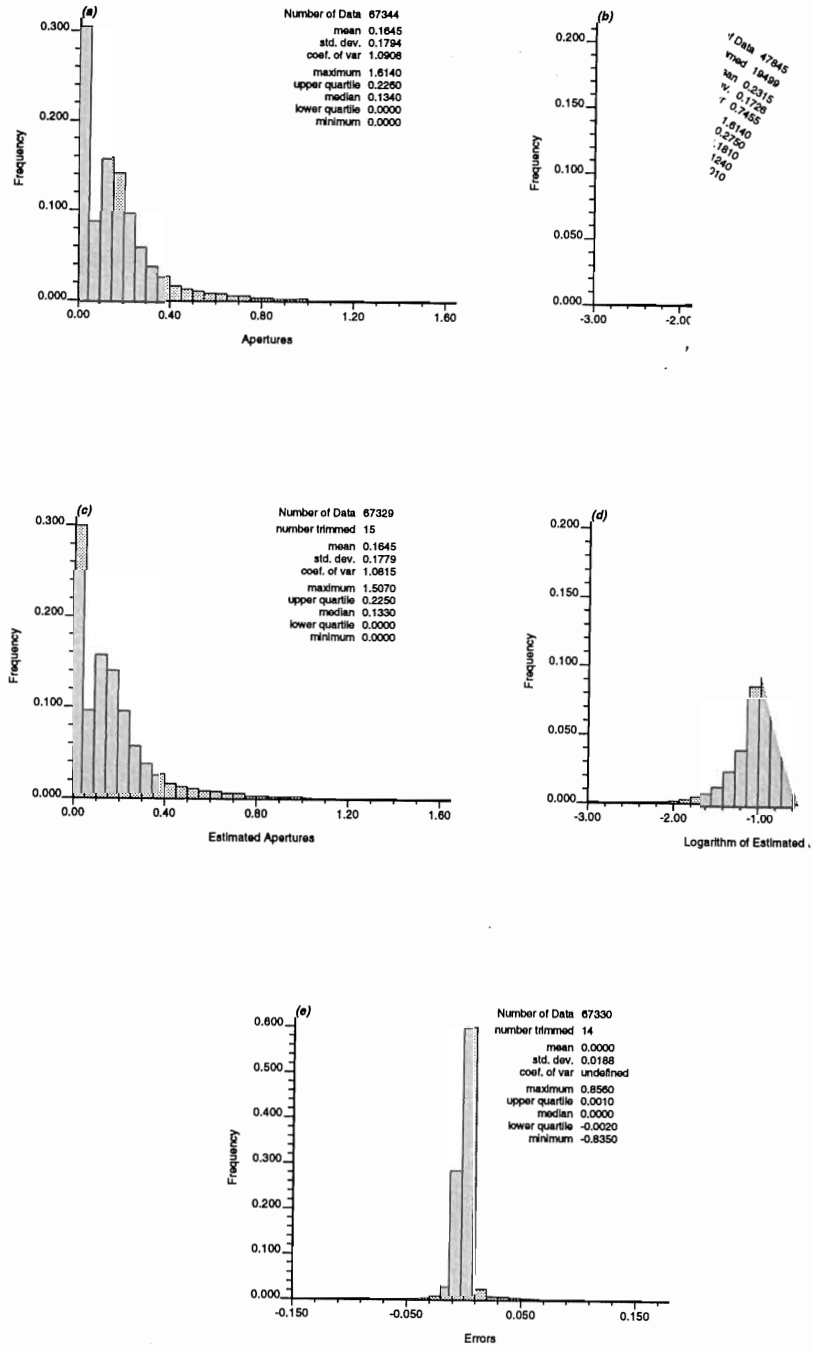

Figure 3-39. Cross validation histograms showing (a) measured apertures (mm), including contact areas, (b) logarithm of the measured apertures without contact areas, (c) apertures (mm) at the measured locations estimated by kriging, including contact areas, (d) logarithm of the estimated apertures without contact areas, and (e) the difference between estimated and measured apertures.

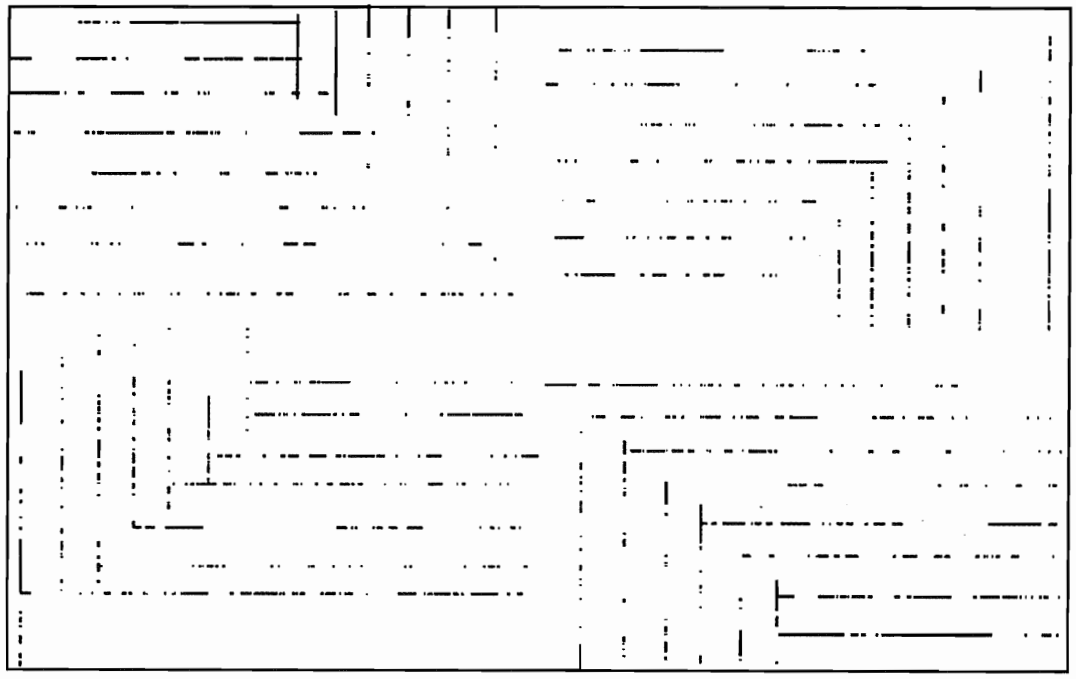

Figure 3-40. Distribution and length of contact (solid lines) along each profile in sample KF24A3. Sample size is 190 mm wide by 290 mm in length.

Table 3-1 Statistics on Äspö 2, Äspö 1, Concrete, and Limestone samples.

Sample			Äspö 2	Äspö 1	Concrete	Limestone
aperture +contact	mean	(mm	0.164	0.112	0.139	0.185
	median	(mm	0.134	0.104	0.092	0.092
	std. dev.	(mm	0.179	0.115	0.158	0.291
	coef.of var.	(%	1.090	1.025	1.136	1.570
aperture	mean	(mm	0.231	0.175	0.202	0.311
	median	(mm	0.181	0.147	0.152	0.162
	std. dev.	(mm	0.172	0.099	0.153	0.321
	coef.of var.	(%	0.745	0.564	0.757	1.033
% of contact (as data points)		(%	28.9	35.7	31.2	40.3

3.7.3 Geostatistical estimation of the fracture pore space

The fracture plane consists of open pore space and contact areas. These two fracture plane attributes can be considered as being represented by two different distributions, one for the apertures and one for the contact areas. If one samples any point in the fracture plane, one will encounter either an open part of the fracture plane or a part where the walls are in contact. Throughout the open part of the fracture plane, the aperture or gap between the adjoining walls will vary. However, in the contact areas, the aperture is assumed to be zero or set to some threshold value.

If the contact areas are completely ignored and the aperture statistics are computed from the open pore space data, the estimated aperture values will definitely be overestimated if they are assumed to be applicable to the whole fracture area. In addition, the spatial continuity of the aperture field will also be overestimated. When estimating the aperture of an unsampled point using univariate statistics, the zero apertures must be taken into account. However, if all the point measurements for the contact areas are included, a single aperture/contact area distribution will be bimodal. One approach to aperture estimation would be to separate the two populations and then estimate the areas dominated by each type separately. This approach could be quite involved.

In the sampling strategy associated with the resin injection approach, the sampling points are not evenly distributed across the fracture plane. Samples cluster along the sampling profiles, i.e., along the X and/or Y direction. By accounting both for the clustering of nearby samples and for their distances to the point being estimated, ordinary kriging handles the adverse effects of clustering much better than other methods. Therefore ordinary kriging using the whole set of data, including aperture and contact areas, has been selected as the procedure for estimating the fracture pore space. No declustering of the data was performed.

The geostatistical estimations of the fracture pore space utilized the GSLIB Software fortran programs (Deutsch and Journel, 1992). The basic approach used in analysing this set of data included the following steps:

1. Modelling the sample semivariograms by using GSLIB's ***gamv2m.for*** and its sub-program ***gamv2.for***.

2. Using Excel to plot the semivariograms, and then fitting the models to the semivariograms based on the shape of the semivariograms and the desired accuracy. The key to successful estimation is to choose a variogram or a covariance that captures the pattern of the spatial continuity that is assumed to be representative of a complete fracture aperture profile.

3. Block kriging was completed using the GSLIB program ***okb2dm.for*** and its sub-program ***okb2d.for***, a 2-D ordinary kriging program. This program performs geostatistical estimation of the pore space using ordinary kriging for non-grided samples. It calculates the aperture and variance values representing the aperture value of the point in the middle of each cell of a grid, or the average aperture value for each cell of the grid; i.e., point kriging or block kriging. The grid size can be easily define within the program

parameter file for both point and block kriging. The output can be plotted as a scaled colour map, showing the distribution of apertures in each cell, by using a GSLIB postscript plotting program ***cscale.for***.

4. Cross validation analyses were performed to evaluate whether or not the aperture estimates meet the desired accuracy. These calculations were performed using GSLIB program ***xvok2dm.for*** and its sub-program ***xvok2d.for***. These programs compare the estimated values at the sampled locations with the actual measured values and generate a table containing the X and Y location, the true value, the estimated value, estimation variance, and error at each sampled point. The output can be plotted as scatter plots using the GSLIB postscript program ***scatplt.for***.

Similarly, quantile/quantile or Q-Q plots, that compare the quantiles of the original data distribution and the distribution of the simulated data points provide an effective means of validating kriged results. GSLIB computes and plots the Q-Q diagrams using a postscript plotting program ***qpplt.for***.

In this investigation, the apertures and contact areas for the Äspö # 2 sample were mapped using a closely spaced grid of profiles in two perpendicular directions. GSLIB has been used to process these aperture and contact area data.

3.7.3.1 Fracture pore space variograms

In order to determine the spatial distribution of apertures and to investigate the effect of data density on the geostatistical estimation of apertures, semivariogram analyses were carried out based on lags equal to 0.07, 0.7, 5 and 10 mm in the X and Y directions and along the 45 degree diagonal direction. Semivariograms based on a lag of 10 mm appear to be inadequate for aperture estimations for this sample since the nugget effects due to low data density are too high to yield an acceptable accuracy. The rough estimates of the nugget effects in both X and Y directions are more than two times the value of the sills. Semivariograms based on a log of 0.7 mm show similar distributions to those based on the lag of 0.07 mm, but have less consistency. When fitting a model to the semivariograms, efforts were concentrated on the multiples of the base lag up to 10 mm, since the individual profiles were spaced about 10 mm apart. It was assumed that this would provide appropriate accuracy for kriging when sample points from the neighbouring profiles were used. The semivariograms in the X and Y directions and their fitted models are given in Figure 3-41. Semivariograms in both X and Y can be described by a nested model, each of which comprises of two exponential models. They are:

in the X direction

$$0.0211 \times [\, 1 - \exp\{\tfrac{-h}{1.7}\}\,] + 0.0152 \times [\, 1 - \exp\{\tfrac{-h}{10.5}\}\,]$$

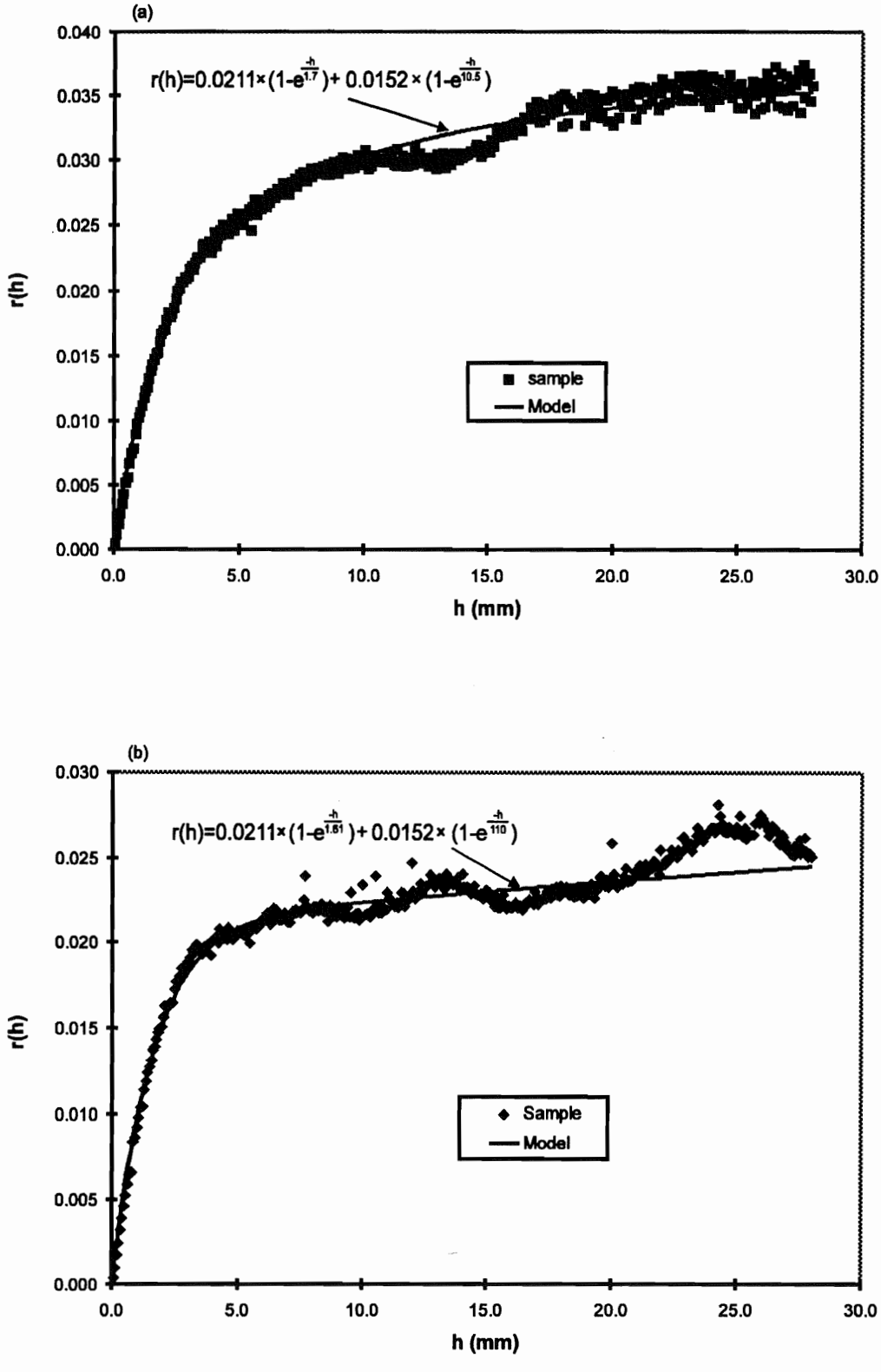

Figure 3-41. Semivariograms (lag=0.07 mm) of measured apertures and the fitted models in the X direction (a) and in the Y direction (b), for Äspö #2.

in the Y direction

$$0.0211 \text{ x } [\text{ 1- exp } \{\frac{-h}{1.61}\}] + 0.0152 \text{ x } [\text{ 1- exp } \{\frac{-h}{110} \}]$$

Given the nature of the sampling strategy that consisted of having profiles distributed along the X and Y direction (Figures 3-37), pairs of data are relatively rare in the 45 degree direction. Semivariogram in that direction are inconsistent. Therefore, for the kriging purpose, it is assumed that semivariograms in the X and Y directions have captured the maximum and minimum spatial continuity of the sample.

Kriging estimates typically have less variability than the true value, i.e., smaller standard deviation. This reduction in variability results from the smoothing effect of estimation, and is a result of the fact that our estimates are weighted linear combinations of several sample values. Since block kriging estimates the average aperture value for each cell, defined by the size of the grid or mesh, block kriging will produce a larger smoothing effect that point kriging. As the grid size increases, the variability of the kriged result decreases. For the purpose of comparison, both point and block kriging were conducted on two grid sizes: 1.5 mm and 5 mm. The map of the estimated apertures for Äspö #2 based on block kriging with a 1.5 mm grid is presented in Figure 3-42. For the block kriging with this grid size, Figure 3-43 shows the kriging variances. Figures 3-44 and 3-45, respectively, show the block kriging aperture estimates and kriging variances for Äspö 2 with using a grid of 5 mm.

In order to investigate the accuracy of the estimation, cross validations were performed. Since the input for flow simulation requires results from block kriging, only the cross-validation results for block kriging are presented here. Figure 3-46 shows the cross validation scatter plots for the measured apertures and estimated apertures based on grid size 1.5 mm. Clearly, the cloud is distributed along the 45 degree line that goes through the origin. This indicates that the kriging result closely predicts the true data. The q-q plots (Figure 3-47) shows that at very low aperture values the kriging results slightly overestimate the sample value; at high values (> 1 mm), it underestimate the sample apertures. According to the frequency distribution of the sample (Figure 3-39), apertures above 1.0 mm comprises a very low percentage of the sample. The smoothing effect of the kriging result based on grid size 5 mm is slight higher than that based on grid size 1.5 mm.

3.8 Comparison of Measured and Computed Fracture Transmissivities

The porous media model MODFLOW (McDonald and Harbaugh, 1988) was used to simulate flow and transport through the fracture plane. It is recognized that a heterogeneous porous media simulation of a discrete fracture as a single layer is at best an approximation of a discrete fracture plane with a highly variable fracture aperture. As discussed in the above section, for this fracture plane, the apertures obtained from the resin profiles were kriged, using ordinary kriging, on a block centered griding where the value at the centre of the grid block represents the average aperture for that block, based

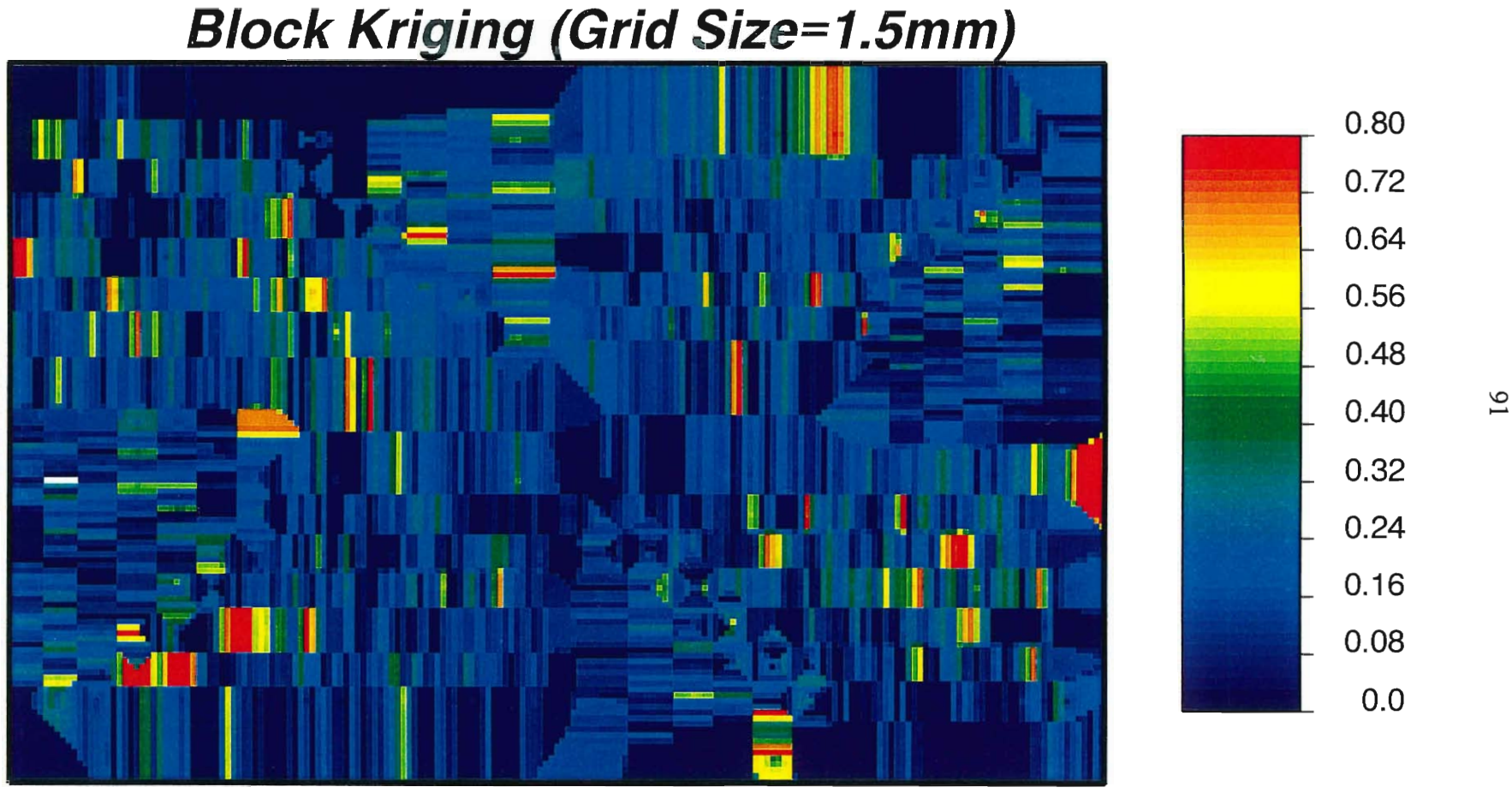

Figure 3-42. Aperture computed by block kriging for Äspö *sample #2. Grid size equals 1.5 mm. Scale on the right hand side is in millimetres.*

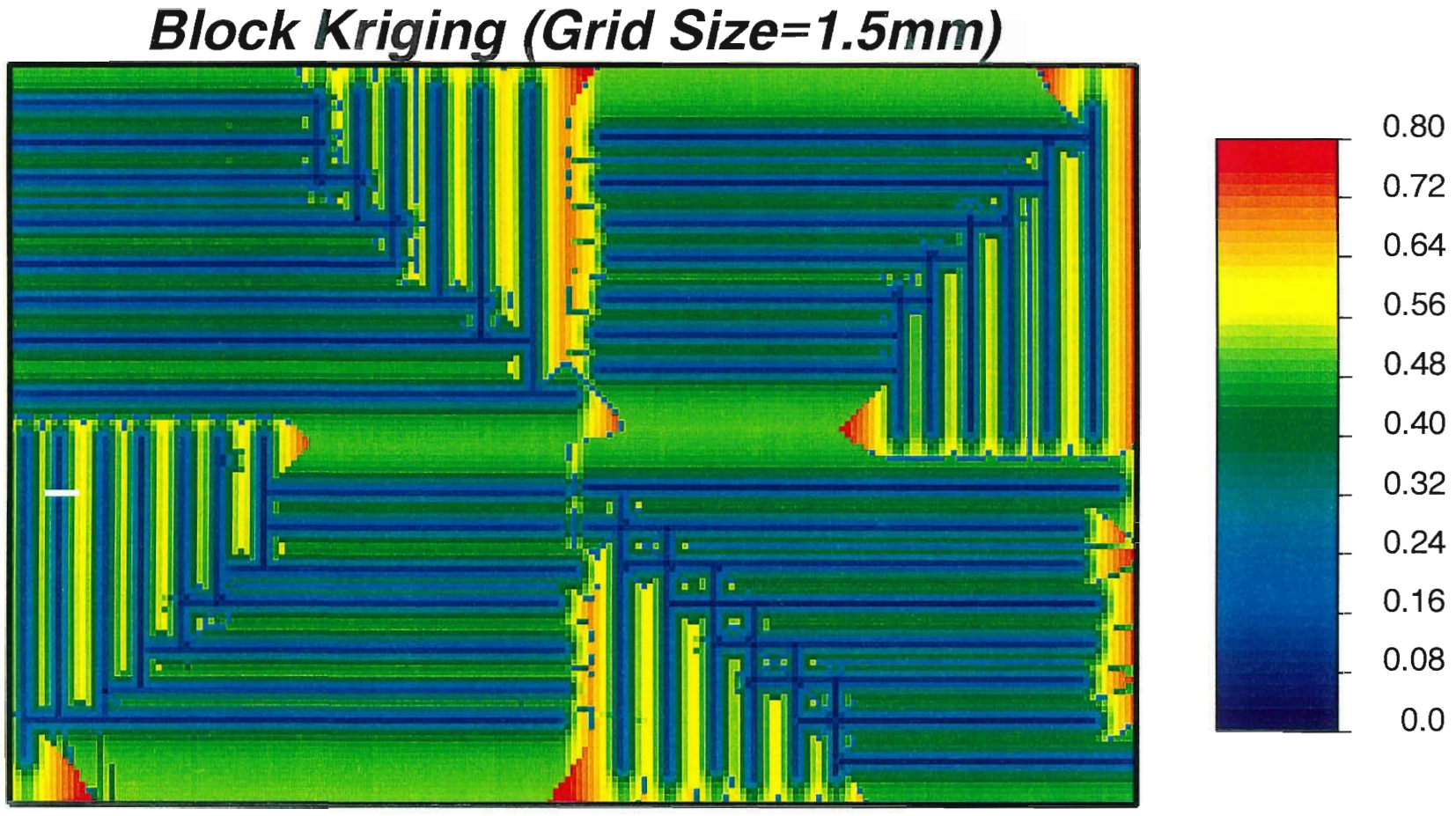

Figure 3-43. Map of aperture variances computed by block kriging for Äspö sample #2. Grid size equals 1.5 mm. Scale on the right hand side is in square millimetres.

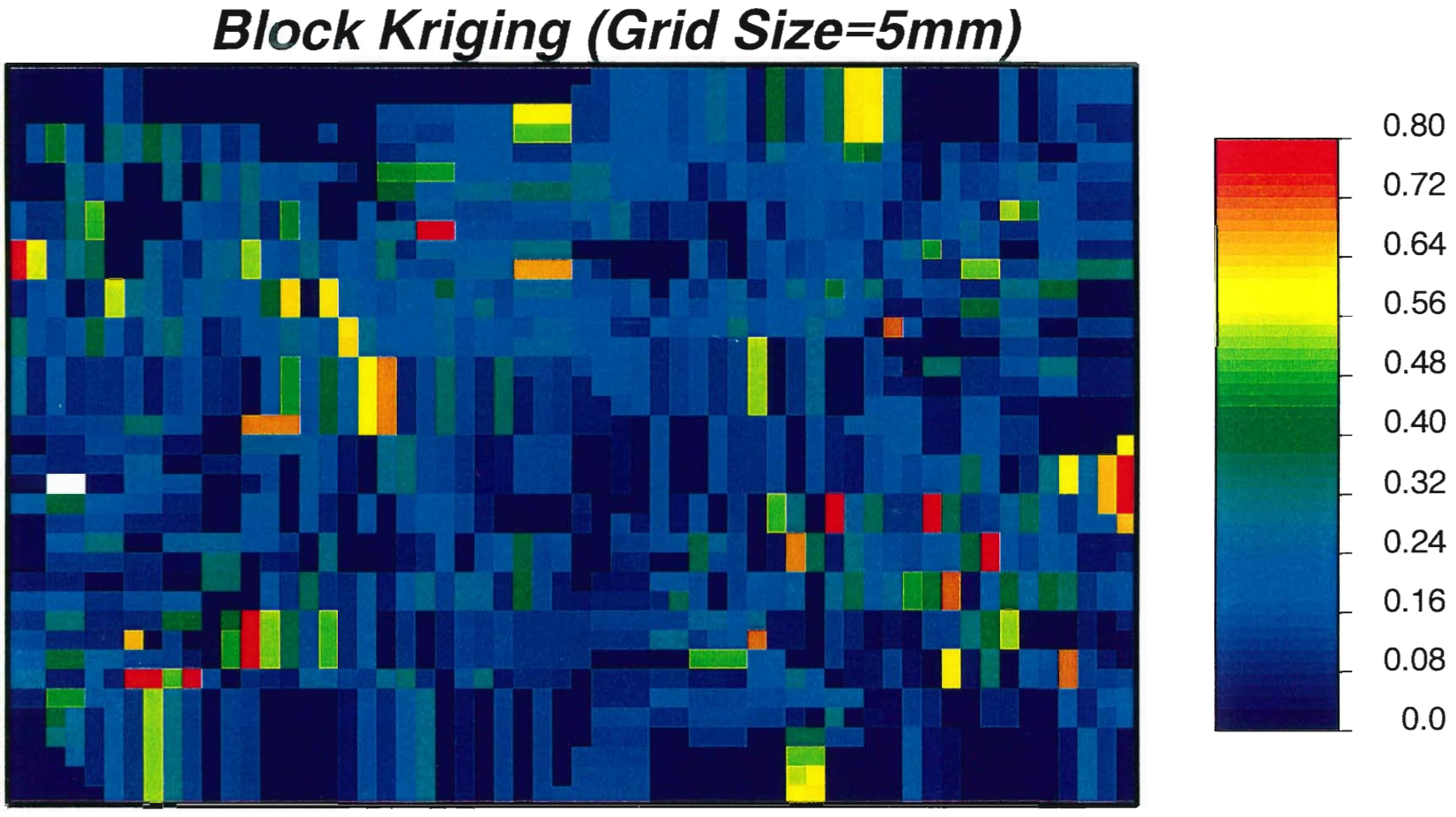

Figure 3-44. Aperture computed by block kriging for Äspö sample #2. Grid size equals 5 mm. Scale on the right hand side is in millimetres.

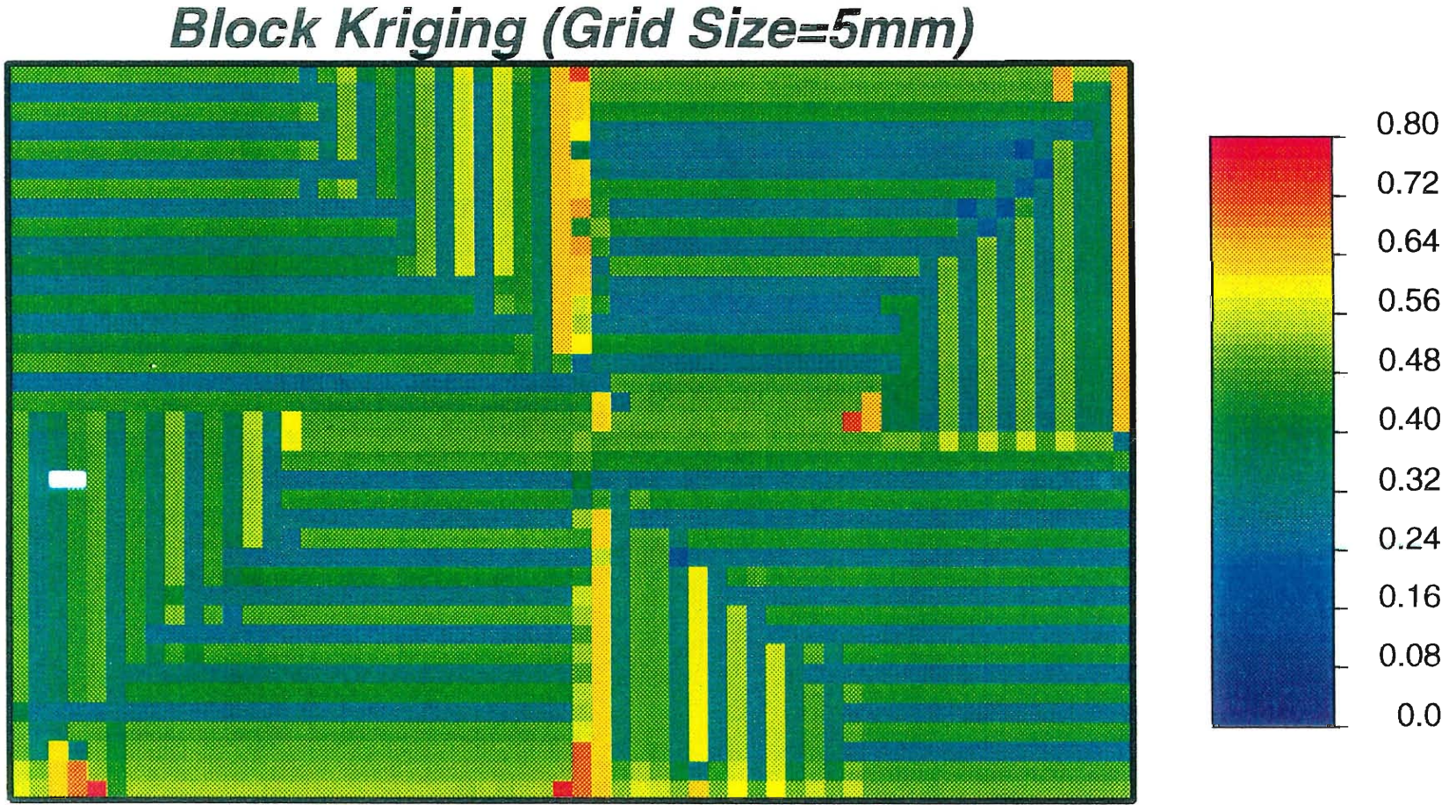

Figure 3-45. Map of aperture variances computed by block kriging for Äspö sample #2. Grid size equals 5 mm. Scale on the right hand side is in square millimetres.

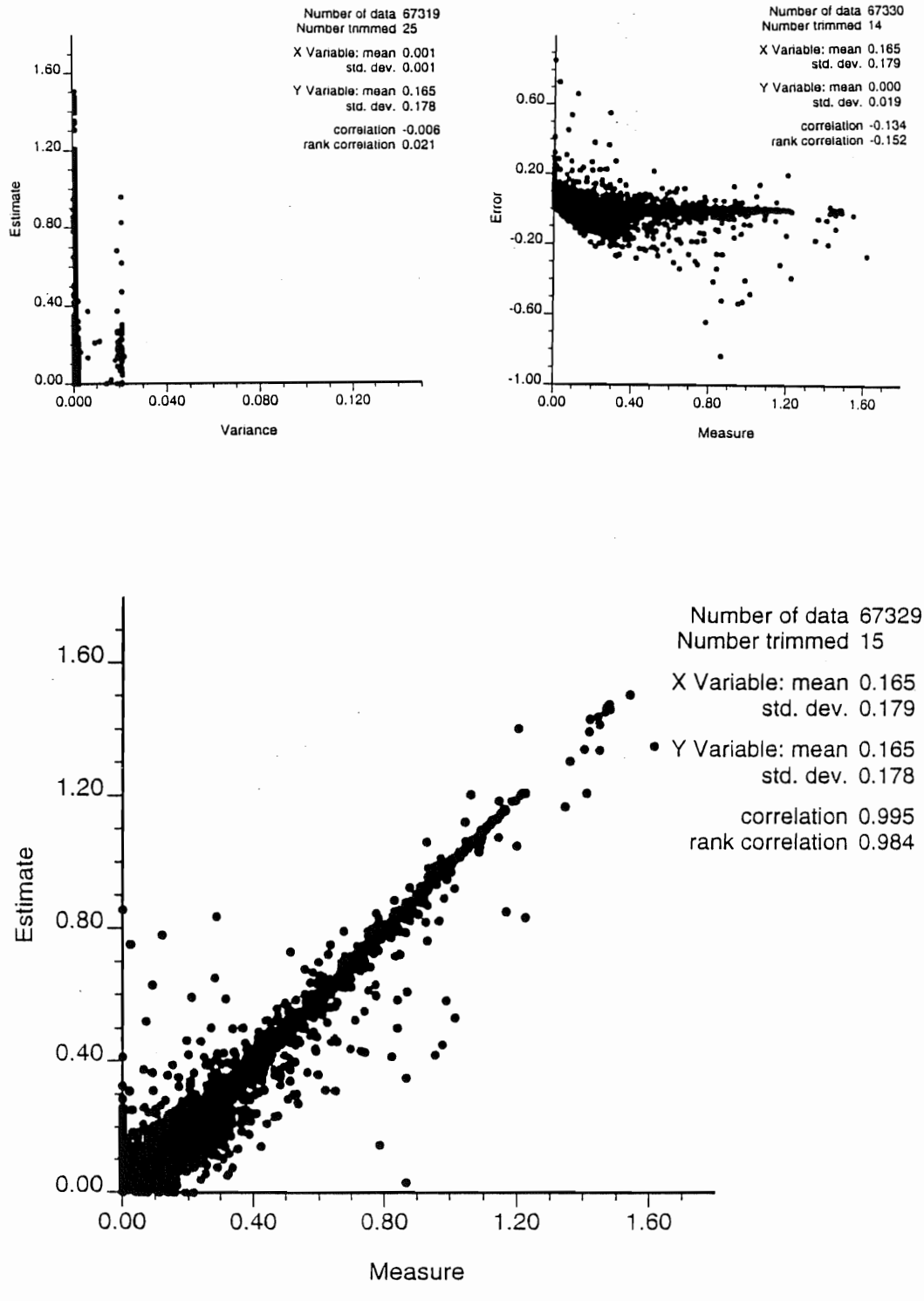

Figure 3-46. Cross validation scatterplots for the measured and estimated data sets.

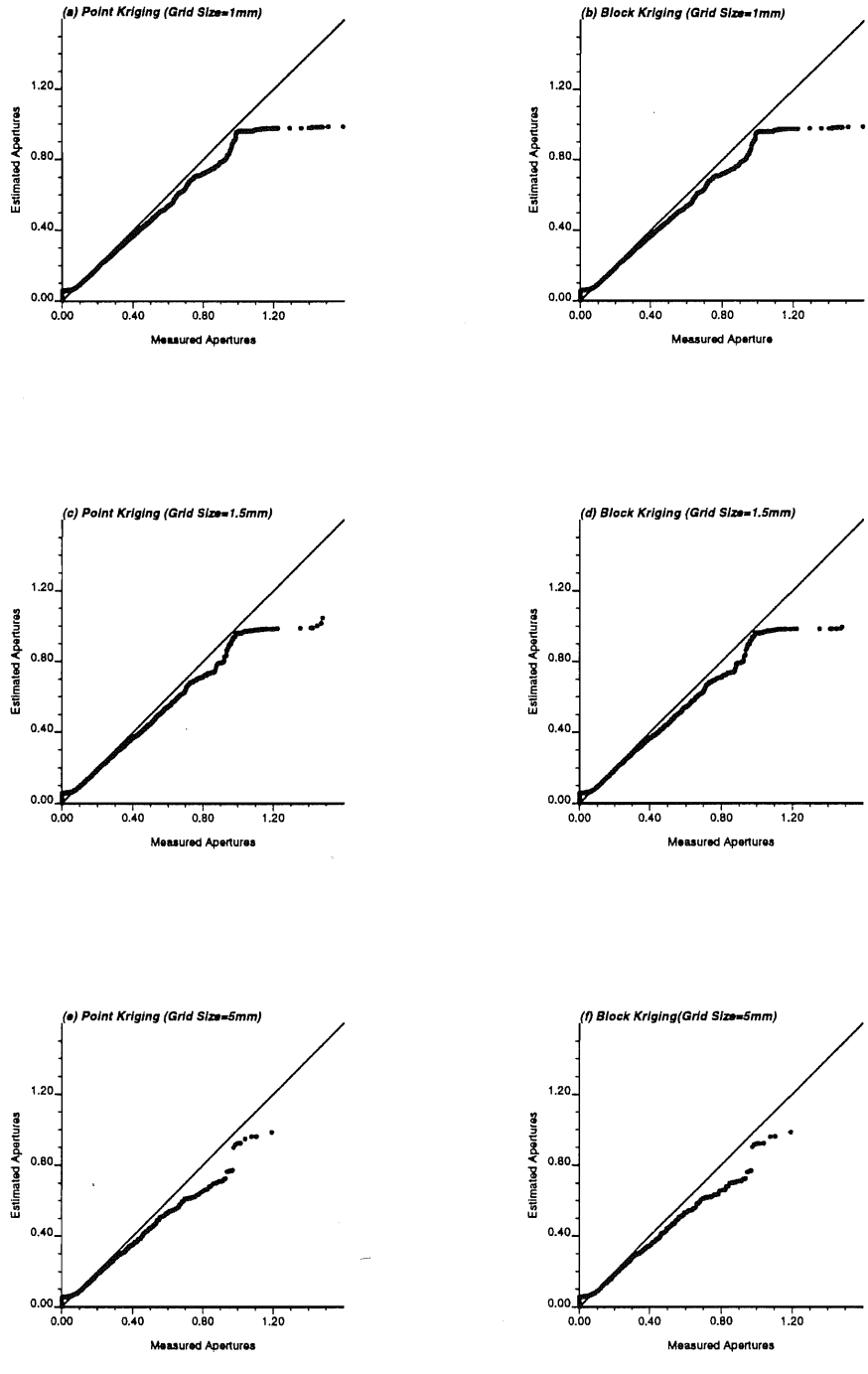

Figure 3-47. Quartile- quartile plots showing the relationship between measured and generated apertures for both point and block kriging at the three selected grid sizes.

on 25 point values. The fracture apertures were kriged for both a 1.5 mm by 1.5 mm grid square and a 5 mm by 5 mm grid square.

The dimensions of the fracture sample (Figure 3-48) were approximately 290 mm long by 190 mm wide. The 1.5 mm grid size required 193 cells in the X direction and 127 cells in the Y direction for a total of 24511 cells. The 5 mm block model required 58 cells in the X direction and 38 cells in the Y direction for a total of 2204 cells to represent the fracture plane.

In order to input the kriged aperture data into MODFLOW the hydraulic conductivity of each grid cell was calculated for each block centered aperture using the parallel plate equation (Louis, 1969) for a rough fracture

$$K_f = \frac{\rho g (2b)^2}{12 \mu \{1+8.8 (k/dh)^{1.5}\}}$$

where K_f is the fracture hydraulic conductivity, ρg is the specific weight, μ is the viscosity and k/dh is the roughness factor (set at 0.5 for a completely rough fracture since the fracture walls are in contact in a macro sense). The equivalent porous media permeability, can be expressed as

$$K = K_f(2b/s)$$

where s is the fracture spacing or the layer thickness; in this case it was set equal to 10 mm. For consistency in computing the velocity of the flow through a discrete fracture, the initial porosity for each grid square in the porous media model was calculated as the ratio of the grid square aperture and the layer thickness.

Cells along both ends of the model were set as constant head boundaries to represent flow in and out of the model while the cells representing the sides of the fracture plane were set as no-flow boundaries. The total flux through the model was calculated as the cumulative flow through all cells on one end of the model. In the initial simulations, the head difference across the model was set to 2.1 m to simulate actual flow test conditions.

The numerical model consisted of 2 layers. The bottom layer, which was used to represent the fracture plane, had a uniform thickness of 10 mm and the hydraulic conductivities were corrected to account for layer thickness in proportion to the aperture values they represented. The upper layer of the model was set to a very low hydraulic conductivity relative to the fracture. Figure 3-48 shows the distribution of hydraulic heads for both the 1.5 mm and the 5 mm grid size models.

Results of the flow simulations using the 5 mm by 5 mm grid were 0.35 mL/s compared to measured results of 0.5 mL/s indicating that the model underestimated the flow through the fracture. However, when the fracture pore space was simulated using the 1.5 mm by 1.5 mm grid block, the results were 0.48 mL/s which compared quite favourably with the measured flowrates (Figure 3-49).

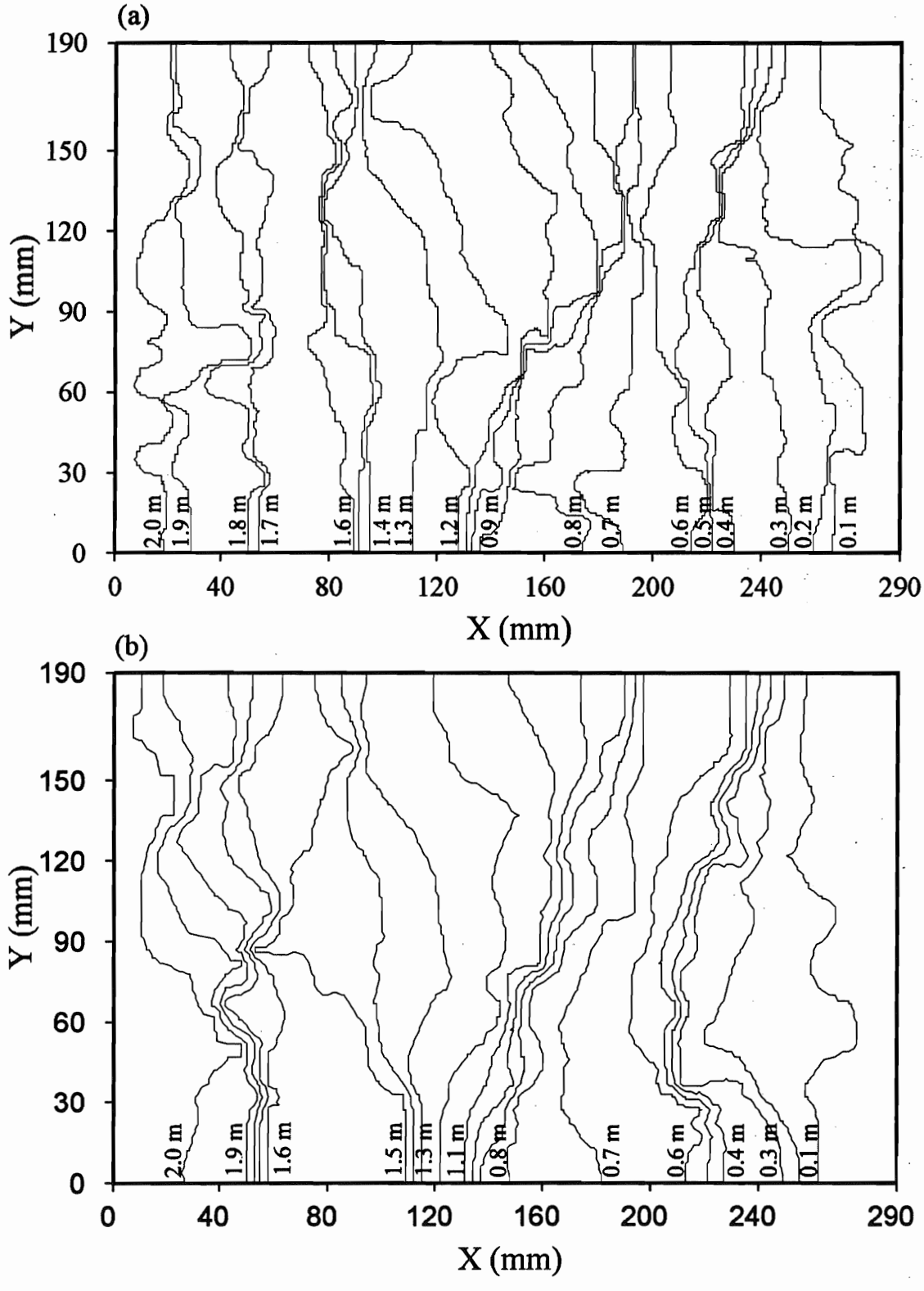

Figure 3-48. Plot of hydraulic head and velocity vectors for (a) cells 1.1 mm by 1.5 mm; (b) cells 5 mm by 5 mm.

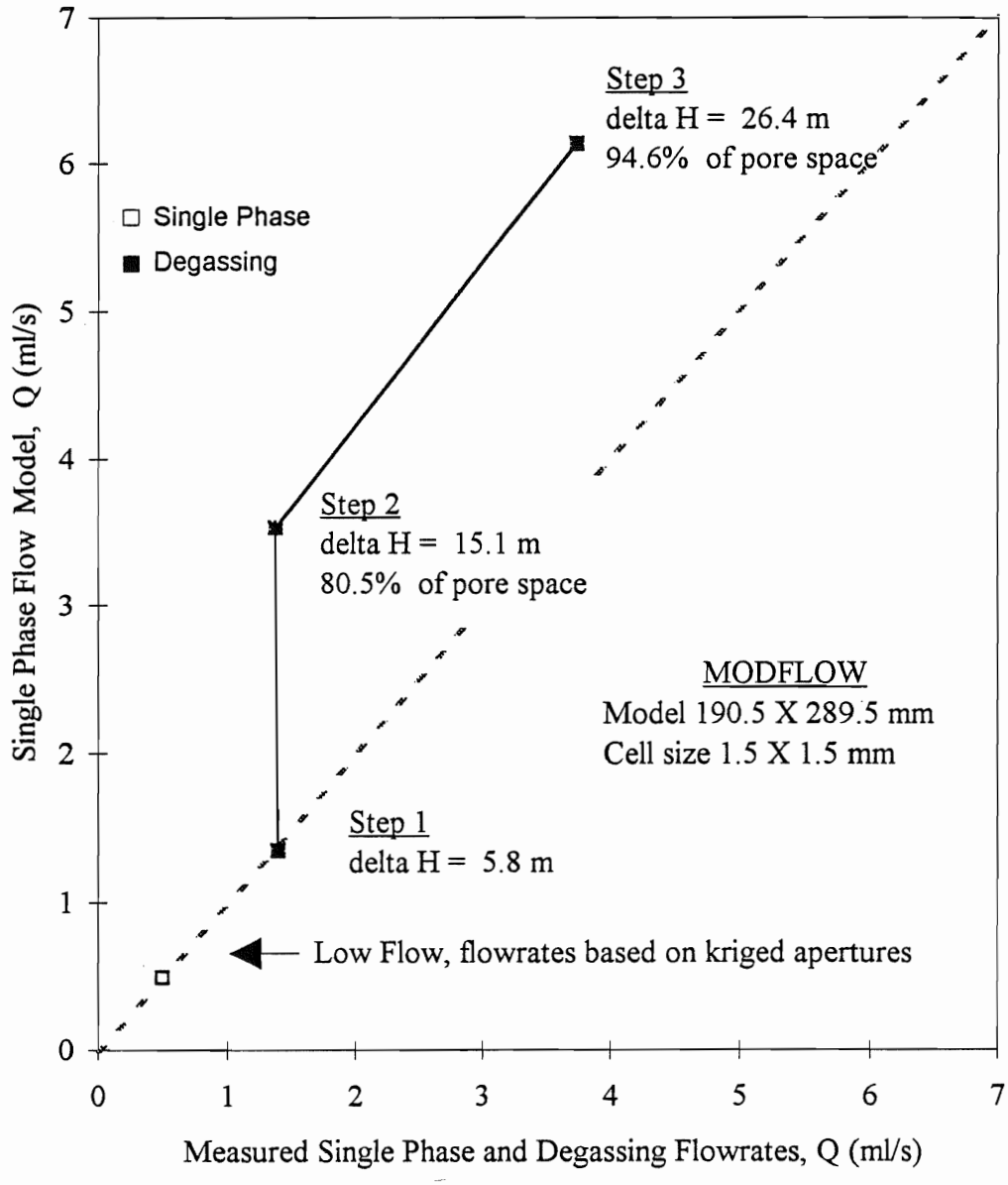

Figure 3-49. Comparison of measured single phase and degassing flowrates with single phase flow simulation using MODFLOW based on removal of large apertures.

3.9 Simulation of Degassing Impacts on Fracture Transmissivitiess

As part of the degassing experiments two phase flow experiments were carried out at different stress levels and at successively higher pressure gradients. The numerical model was used to simulated the flow experiments carried out at 10 MPa before resin was injected. The 1.5 mm grid model was used for these simulations

At 10 MPa the degassing was carried out in three steps, with the change in pressure gradient increasing from 5.8 m to 15.1 m to 26.4 m. At the first step, the calculated flow of 1.35 mL/s agreed with the measured flow of 1.39 mL/s. However when the change in head was increased for steps 2 and 3 the measured flow was much less than the calculated single phase model flux indicating that degassing at the higher pressure gradients created a decrease in hydraulic conductivity.

It has been hypothesized that the decrease in the observed permeability could be caused by gas bubbles coming out of solution and blocking flow through some of the apertures. It has been debated that the gas bubbles accumulate in large pores spaces, removing them from the flow path. Alternatively it has been suggested that gas bubbles as they evolve will more likely block off the smaller apertures. Therefore numerical model simulations were carried out by removing first the large apertures in one set of simulations (Table 3-2) and secondly by removing the small apertures in a second set of simulations (Table 3-3) to fit the flowrates computed by the models to the measured fluxes at the different hydraulic head gradients.

Starting with the basic model using a 1.5 mm block, the largest apertures were successively deleted from the grid and replaced with values equal to the minimum aperture of 0.001 mm. Initially the largest aperture in the model was 1.091 mm and it was found that all apertures greater than 0.502 mm had to be removed to obtain agreement between the flowrates computed by the model and the step 2 measured flowrates (Table 3-2). Removal of these large apertures reduced the fracture pore space volume to 80.5 % of the initial pore space volume. The same approach was taken to fit the model to the step 3 data. However in this case only apertures greater than 0.797 mm had to be removed, reducing the fracture pore space volume to 94.6% of the original pore space volume in the model (Table 3-2).

To model the effects of blocking the smaller apertures, the smaller apertures were successively removed from the model and set to the minimum value of 0.001 mm. In the original model the smallest aperture was 0.002 mm. To match the flowrates computed by the model to the flowrates measured in step 2 all apertures up to 0.100 mm had to be removed which represented a reduction to 91.9 % of the original pore space volume, reducing the average aperture from 0.158 mm to 0.145 mm. To fit the model to the step 3 data, only apertures up to 0.074 mm had to be removed, producing an average aperture of 0.152 mm, representing 96.1 % of the original pore space volume (Table 3-3).

Table 3-2 **Comparison of computed and measured flowrates, showing changes in the largest apertures required to fit the model to the measured data.**

Step	ΔH (m)	Measured Q (mL/s)	Single Phase Model Q (mL/s)	Adjusted Model			
				Largest Aperture (mm)	Average Aperture (mm)	% of Original Pore Space	Model Q (mL/s)
0	2.1	0.5	0.48	1.091	0.158	---	---
1	5.8	1.39	1.35	1.091	0.158	---	---
2	15.1	1.27	3.53	0.502	0.127	80.5	1.25
3	26.4	3.37	6.14	0.797	0.149	94.6	3.1

Table 3-3 Comparison of computed and measured flowrates, showing changes in the smallest apertures required to fit the model to the measured data.

Step	Δ H (m)	Measured Q (mL/s)	Single Phase Model Q (mL/s)	Adjusted Model			
				Smallest Aperture (mm)	Average Aperture (mm)	% of Original Pore Space	Model Q (mL/s)
0	2.1	0.5	0.48	0.002	0.158	---	---
1	5.8	1.39	1.35	0.002	0.158	---	---
2	15.1	1.27	3.53	0.100	0.145	91.9	1.30
3	26.4	3.37	6.14	0.074	0.152	96.1	3.36

4 Visualization of Degassing in Fracture Replicas

4.1 Experimental Design

This experiment was designed to permit direct observation of degassing effects in a fracture replica in which the roughness on the fracture surface was similar to that which was created on the surface of the large scale physical model and on the concrete model fracture surface. The fracture surfaces were first created using a geotextile fabric to imprint the small scale roughness on the surfaces of two well mated concrete blocks as described in Chapter 3 for the concrete sample. The same geotextile fabric was used to create the surfaces on the Large Scale Physical Model, the Concrete model and these fracture replicas. Fracture replicas were then cast at Sandia National Laboratories (SNL) by SNL and Fracflow staff, from these concrete surfaces, using a transparent epoxy, under the overall guidance of Dr. R. Glass and following procedures developed by R. Glass and his staff at SNL.

Figure 4-1 shows the overall experimental configuration for the degassing experiments on the fracture replicas. The experimental system assembled at SNL consisted of a fracture test cell, a CO_2 equilibrium unit, a N_2 pressurization unit, an air confinement unit, a water supply unit, data acquisition unit, and an image acquisition unit. Figure 4-2 shows the details of the test cell that was used in these experiments. Figure 4-3 shows the location of the manometer ports for this model, as well as port (6) in the center of the fracture plane that was used to simulate a borehole for convergent flow (Figure 4-4). The degassing experiments consisted of introducing water saturated with gas (CO_2) into the fracture plane to examine how the gas phase separated from the water as the fluid pressure decreased along the flowlines under both linear and convergent flow. By increasing the confining pressure on the cell, the degassing affects could be examined as the relative roughness and the transmissivity of the fracture plane changed. For this fracture replica, one of the main points of interest was to determine how the relatively uniform roughness of the fracture surface would affect the bubble trapping capacity of the fracture pore space, as the hydraulic gradient and hence the flowrate increased. In addition, these experiments were designed to observe the rate at which a separate gas phase forms for a given set of boundary and flow conditions and gas contents. The main interest was to determine whether or not there was threshold volume or area of gas accumulation or build-up within the fracture plane before the gas phase would impact the computed fracture transmissivity.

4.2 Fracture Test Cell and Data Acquisition

The structure of the fracture test cell is shown in Figure 4-2. The fracture model consisted of a fracture plane formed by two pieces of the cast Epoxy fracture, consisting of the top half and bottom half of the fracture. The fracture plane was 292 × 292 mm in size. One central borehole was located in the top half of the epoxy cast. Six manometer boreholes were drilled in the bottom half of the epoxy cast. Two air pressure holes, one in each side of the model, were used to apply air pressure in the space between the epoxy model and the glass plate and hence maintain a confining pressure on the fracture plane.

The test assembly frame consisted of two Aluminum brackets, one on each side of the model, that were held together by four evenly spaced bolts on each side of the model. The Aluminum frame formed a compression contact with the edges of the 3/4" plate glass that formed the confinement chambers. Two Port and Flow Manifolds (PFM) were fitted to opposite sides of the model along the edge of the fracture plane and pressure sealed. This permitted both constant pressure or no-flow boundary conditions to be maintained for selected experiments. The other two boundaries or edges of the model were sealed to provide no-flow boundary conditions. Both the manifolds and the boundary seals were held in place by a series of laterally applied machine screws. During the calibration and degassing experiments, the test cell was mounted on a rotating test stand that incorporated a light source to highlight the fracture plane and a high resolution camera to image the flow field.

The Data Acquisition system automatically recorded the pressure and temperature of the water in the test fracture plane, and the weight of the water outflow at selected time intervals, which was used to calculated the flowrate (Figure 4-1). The imaging unit consisted of a Macintosh computer and a Rotating Test Stand (RST-1). The RST-1 is equipped with a high resolution Photometrics camera (KA 4200). The RST-1 camera was positioned to acquire images of the entire cell.

Pressure tanks with a bed of marbles in the bottom of each tank, similar to the beds used in the large degassing tanks, were used to saturate the test water, which was dyed blue, with carbon dioxide. The water was pressurized with nitrogen to maintain the CO_2 saturated water at or above the bubble pressure for the given test pressure. A 0.33 MPa check valve was installed on the nitrogen pressure cylinder to provide a safety release to protect the test cell and pressure tanks in the event that the pressure diaphragm ruptured.

Figure 4-5 shows a full image of the fracture replica with 1/8 of the cell volume being occupied with the blue-dyed water. The dark lines in this image are the holes that were drilled in the epoxy to connect up the manometer ports to the pressure sensors that were located outside the model. The black thick line at the top of the image has been added to the photograph to highlight the interface between the fluid and the air filled fracture pore space. The relatively straight nature of this line, and the limited interfingering of the fluid with the open gas filled fracture space, indicates that the fracture aperture is fairly uniform, suggesting that the fabricated fracture plane has a uniform fracture surface roughness.

4.3 Preliminary Experiments

Initial qualitative flow experiments were completed on the 292 by 292 mm fracture replica to determine the nature of the degassing under a range of flowrates, pressure gradients and gas saturations, for both linear flow and convergent flow (from two sides to a central borehole) geometry. The transparent fracture models that were created using the geotextile imprinted surface produced a highly conductive fracture plane, similar to the large physical model. This high conductivity produced high fluid velocities within the fracture plane, even at low pressure gradients and even under confining pressures of 0.18 MPa. Higher confining pressures could not be used since the plastic fracture replicas generally exhibit significant creep effects at the higher confining pressures, leading to a continuous decrease in fracture transmissivity, making it difficult to establish steady state conditions for the degassing experiments.

The preliminary flow tests at different flowrates (Figure 4-6) show that only small hydraulic gradients could be generated in this model at high flowrates for linear flow geometry under maximum confining pressures. However, under convergent flow conditions (Figure 4-7), high hydraulic gradients could be generated over a small area around the central discharge point. When the pressure in the wellbore was dropped to atmospheric, providing the maximum gradient, the flowrate was measured at 15.54 ml/s, which produces very high fluid velocities. Figure 4-8 shows that with increasing gradient, the flowrate versus gradient curve becomes non-linear for single phase flow. The same non-linear relationship is also shown for the two-phase flow measurements with a clear reduction in fracture transmissivity due to degassing of the gas saturated water under convergent flow conditions.

In these preliminary degassing flow experiments, for the low pressure gradients generated under linear flow conditions, it was difficult to maintain the fracture inlet fluid pressures above the bubble pressure for the gas saturated fluid. As the inlet pressure dropped below the bubble pressure, gas bubbles were generated over much of the fracture plane in these qualitative experiments. Gas bubbles that formed within the fracture plane by degassing generally had a low residence time within the fracture plane. However, when the fluid pressures at the inlet were dropped below the bubble pressure the bubbles entering the fracture plane appeared to promote widespread bubble generation within the fracture plane. These bubble clusters tended to have a periodic stability, that is they would grow and then after a sufficient area of the fracture plane had been filled with gas, the bubble clusters would migrate rapidly in the direction of flow. Under convergent flow conditions, the area around the central borehole was swept clear of gas bubbles by the fluid acceleration. The size of this area around the borehole increased with increases in the fluid pressure gradient. The inertial forces due to the high fluid velocities easily overcame the viscous forces and the low trapping forces provided by the uniform nature of the pore space roughness.

4.4 Measurement of Mean Fracture Aperture and Aperture Field

Since the surface roughness of the fracture replicas were thought to form a very uniform pore space, with a low gas bubble trapping capacity, the first step in the experimental programme was to quantify the mean apertures and the aperture fields at different confining pressures. The mean or average aperture of this fracture was measured at 0.028 MPa (4 psi) air confinement pressure, using 1g/L FD&C blue dye, following the standard procedure developed at Sandia. Assuming the area under the o-ring is saturated, the mean aperture was calculated by subtracting the dyed water and air images. The mean aperture under 0.028 MPa (4 psi) confinement pressure was 0.26 mm.

Epoxy replicas exhibit some degree of creep and the apertures are stress dependent. Hence, the aperture field was measured at three cell confining pressures, 0.028 MPa (4 psi), 0.056 MPa (8 psi) and 0.083 MPa (12 psi). Under each confinement pressure, two sets of images were taken in order to get a satisfactory contrast. For each confining pressure, one set of images was taken when the fracture was saturated with clear water and the other was taken when the fracture plane was saturated with 0.125g/L blue dye water. Each final image was a composite of 70 individual images.

The normalized field at 0.028 MPa (4 psi) confining pressure is shown in Figure 4-9. The normalized aperture distributions at effective normal pressures of 0.028 MPa (4 psi), 0.056 MPa (8 psi) and 0.083 MPa (12 psi) are given in Figure 4-10. While there is some slight change in the peak frequencies, there is only a small change in the aperture distribution, and hence in the mean aperture due to these changes in the confining pressures.

The amount of water expelled from the fracture plane was also measured for confining pressures of 0.028, 0.056, 0.083, 0.138 and 0.166 MPa, using a syringe with all ports and outlets closed. The amount of water released from the fracture plane during each 0.028 MPa pressure increment is very similar, about 0.14 - 0.16 cubic centimetres. The higher the confinement pressure, the smaller the volume, indicating a stiffening of the fracture with increasing confining pressure. For the 292 × 292 mm test cell, with each 0.028 MPa pressure increment, the aperture reduces by 2×10^{-6} mm.

At the end of the degassing experiments the fracture plane was injected with a room temperature curing resin, the replica was sectioned and selected cross-sections through the fracture plane were photographed and digitized. Figure 4-11 shows a typical photograph of the resin filled replica cross-section. Figures 4-12 and 4-13 show two of the digitized profiles through part of the fracture replica. Because of the transparency of the epoxy and the resin, the edges of the fracture formed by the resin have been outlined. These profiles and the photograph confirm the large aperture in this fracture replica and show the limited contact area between the adjoining fracture walls as well as the low trapping capacity of the fracture cross-section.

4.5 Degassing Experiments

Degassing tests were carried out under both linear and convergent flow configurations. The degassing tests were conducted by opening the outlet valve gradually until the pressure inside the fracture plane was lower than the CO_2 saturation pressure. The inlet pressure was maintained above the CO_2 saturation pressure. This procedure was designed to observe how the gas phase separated from the CO_2 saturated water. During the degassing experiments, data were recorded at 5 second intervals and images were taken at 1 minute intervals in order to:

1. Delineate the area of the fracture plane that was occupied by the evolved gas at the different pressure steps and estimate the volume of the fracture plane that was filled with gas as a function of time and estimate the percent gas in solution at the start of the experiment.

2. Determine how the structure of the gas phase evolves as a function of time, the nature of the bubble growth and the distribution of the bubbles as a function of measured changes in transmissivities.

3. Determine the size of the zone in which the gas bubbles were continually swept as a function of pressure gradient and flowrate.

These quantitative experiments confirmed the short residence times of the fluid within the fracture plane for fractures with very uniform roughness. The high flowrate in this fracture swept the water and very small bubbles out of the fracture plane before the bubbles could evolve and coalesce. It was practically impossible to develop nucleation inside the fracture plane, when the inlet pressure was maintained above the CO_2 saturation pressure. In order to enhance the gas phase evolution, the inlet pressure would have to be reduced to about 0.0035 MPa (0.5 psi) below the saturation pressure and a large volume of gas saturated water would be needed so that the flow experiment could be maintained for a long period of time. In order to observe the sweeping effect within the time available at the given flowrate, bubbles were introduced into the fracture plane by lowering the inlet pressure by about 0.01 MPa, so that the bubbles started to evolve at the edge of the fracture. Based on these fracture replica experiments, it is apparent that much lower fracture transmissivities and much rougher fracture surfaces with a highly variable pore space are needed to produce pressure drops and induce degassing within the fracture plane at the gas saturations and sample sizes being used in these experiments.

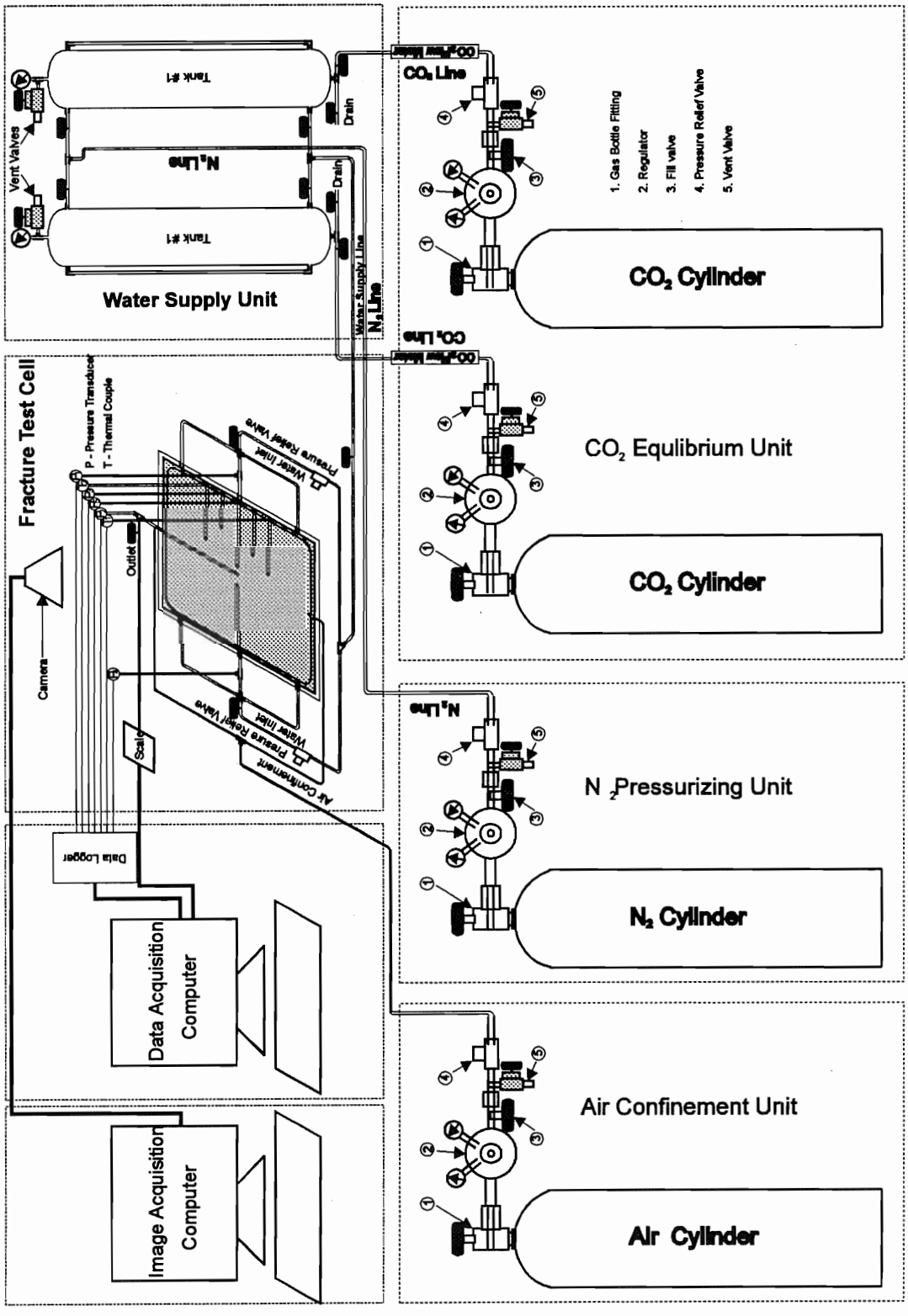

Figure 4-1. Experimental Design for Degassing, Convergent Flow

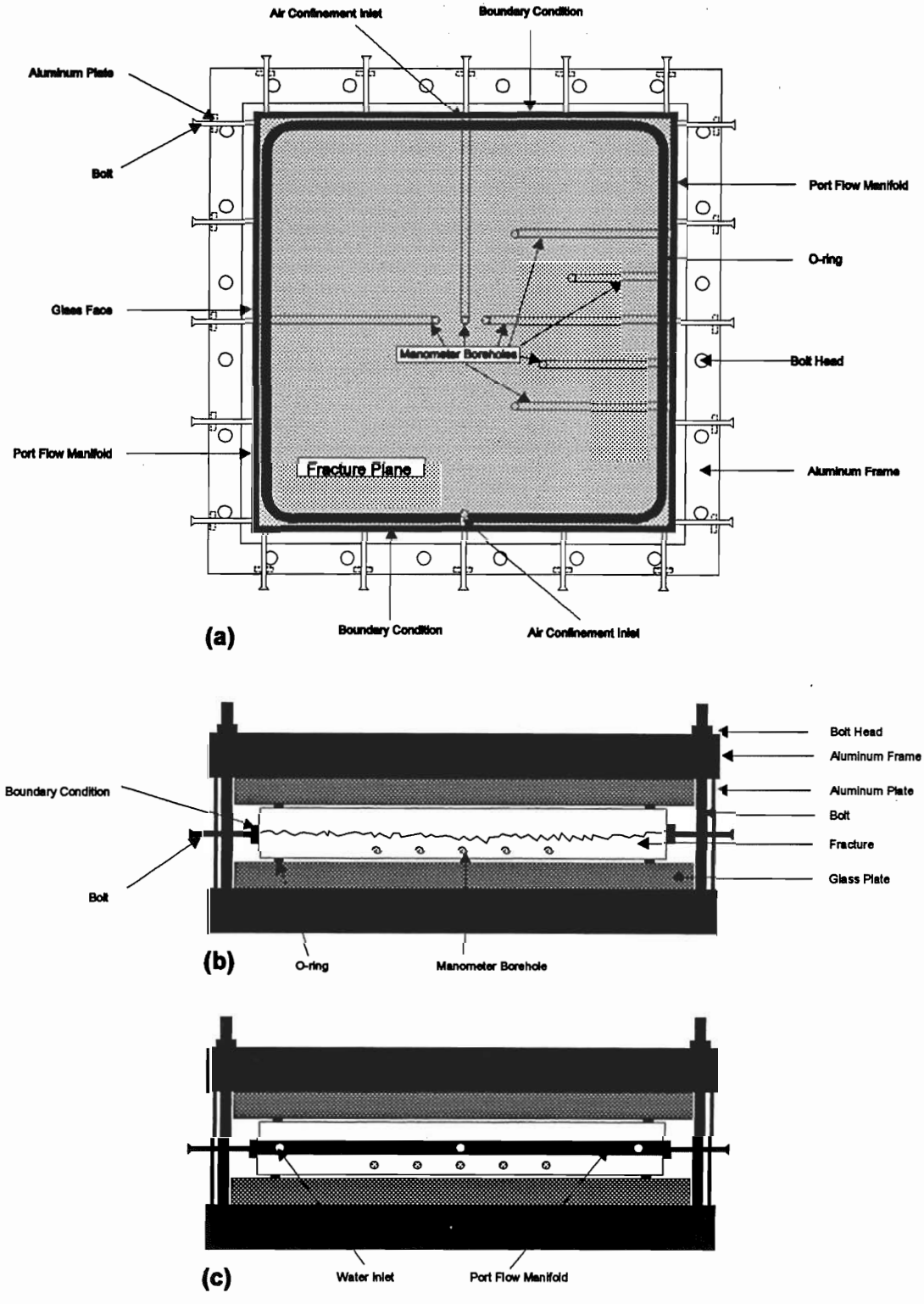

Figure 4-2. Fracture test cell. (a) Top view; (b) Side View without flow manifold; (c) Side view with flow manifold.

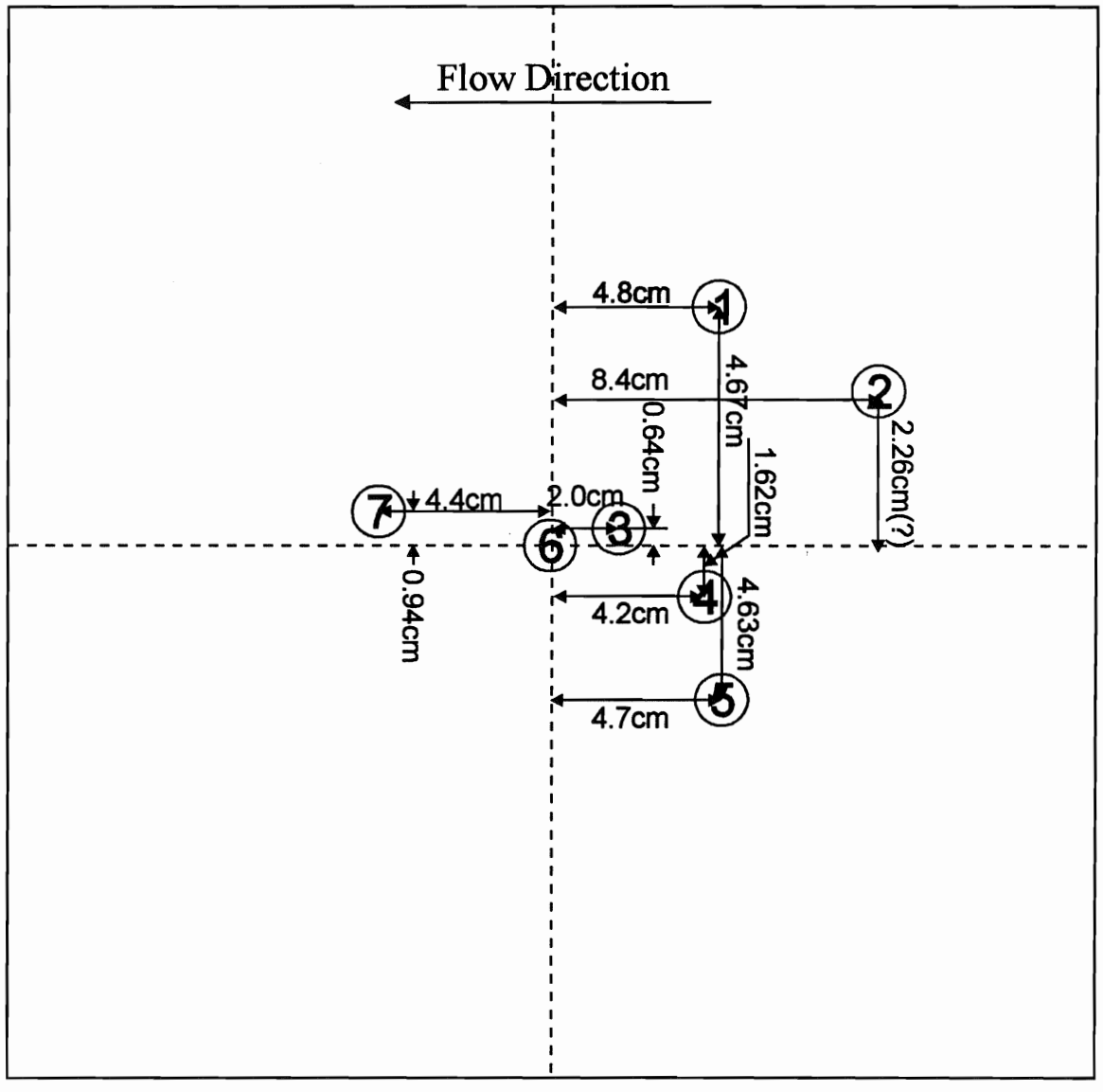

Figure 4-3. Map of Manometer Ports in the Replica (Linear)

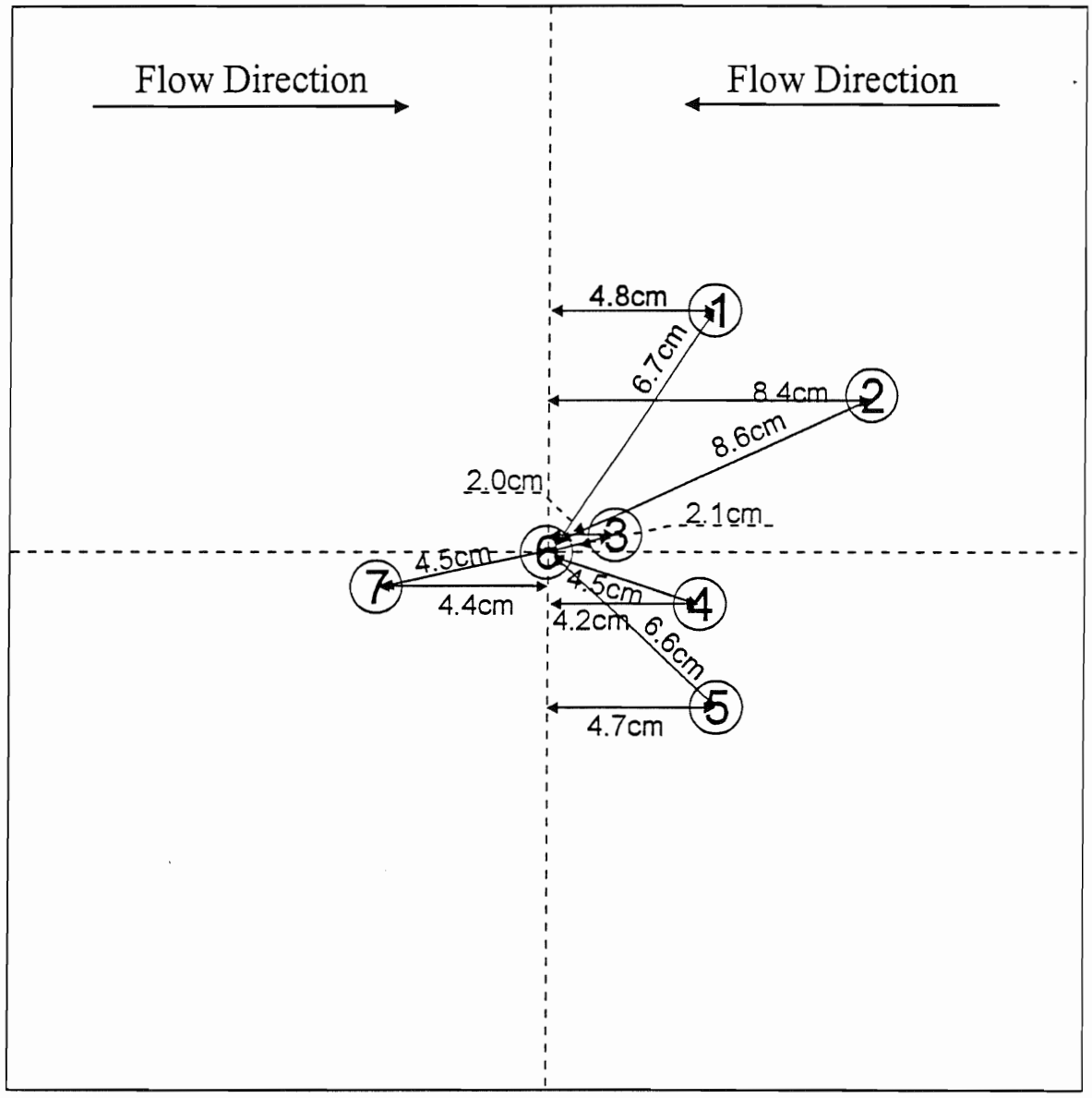

Figure 4-4. Map of manometer ports for convergent flow in the fracture replica.

Figure 4-5. Blue dye (.125g/L) as cell fliud occupying approximately 7/8 of the cell volume. The cell is orientated at a 45 degree angle from the vertical with gravity acting toward the top of the page. The black line indicates the interface between the blue dye (above line) and air (below line).

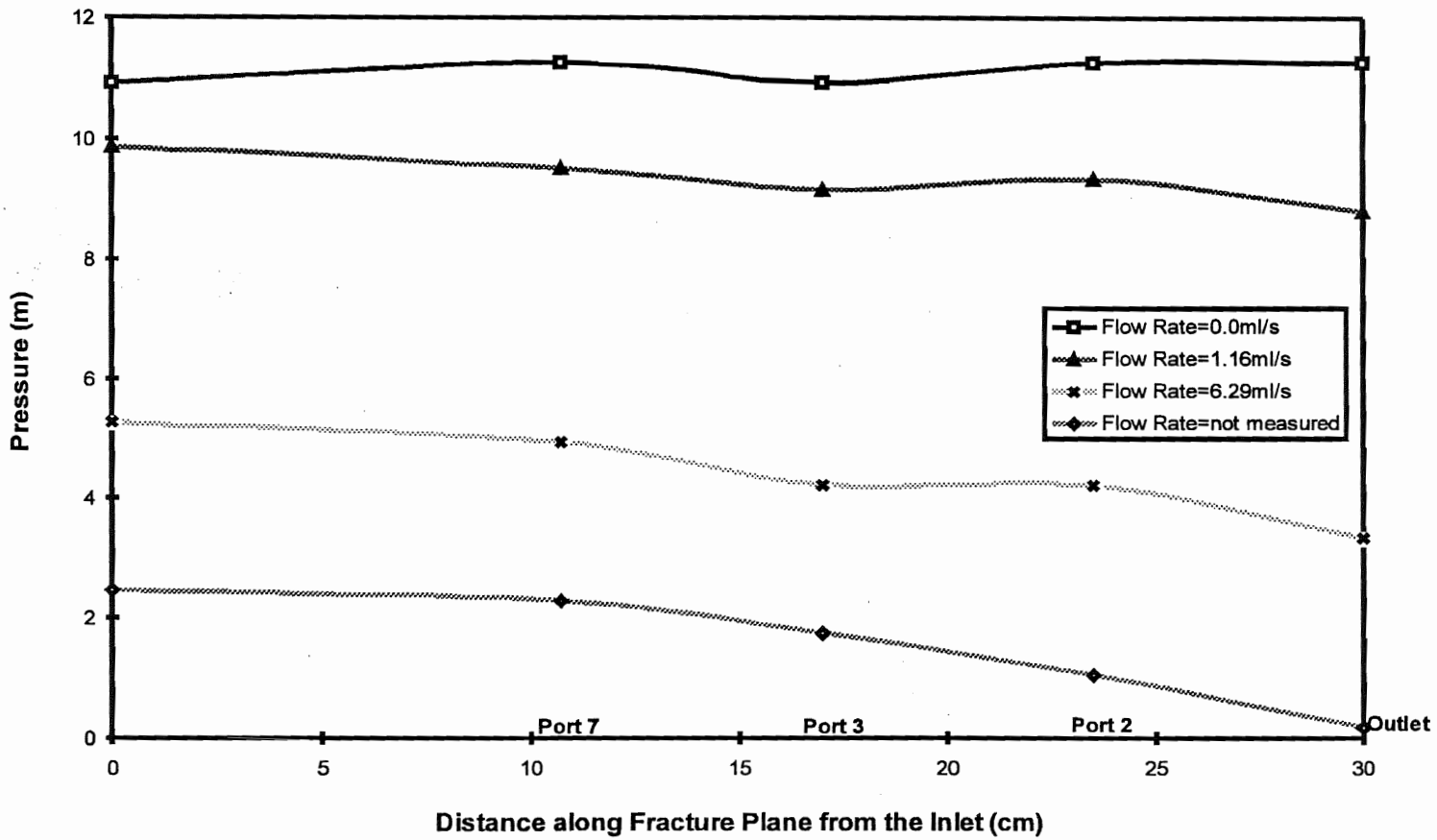

Figure 4-6. Linear flow trial, single phase, pressures measured across the fracture plane, from the inlet on the left to the outlet on the right.

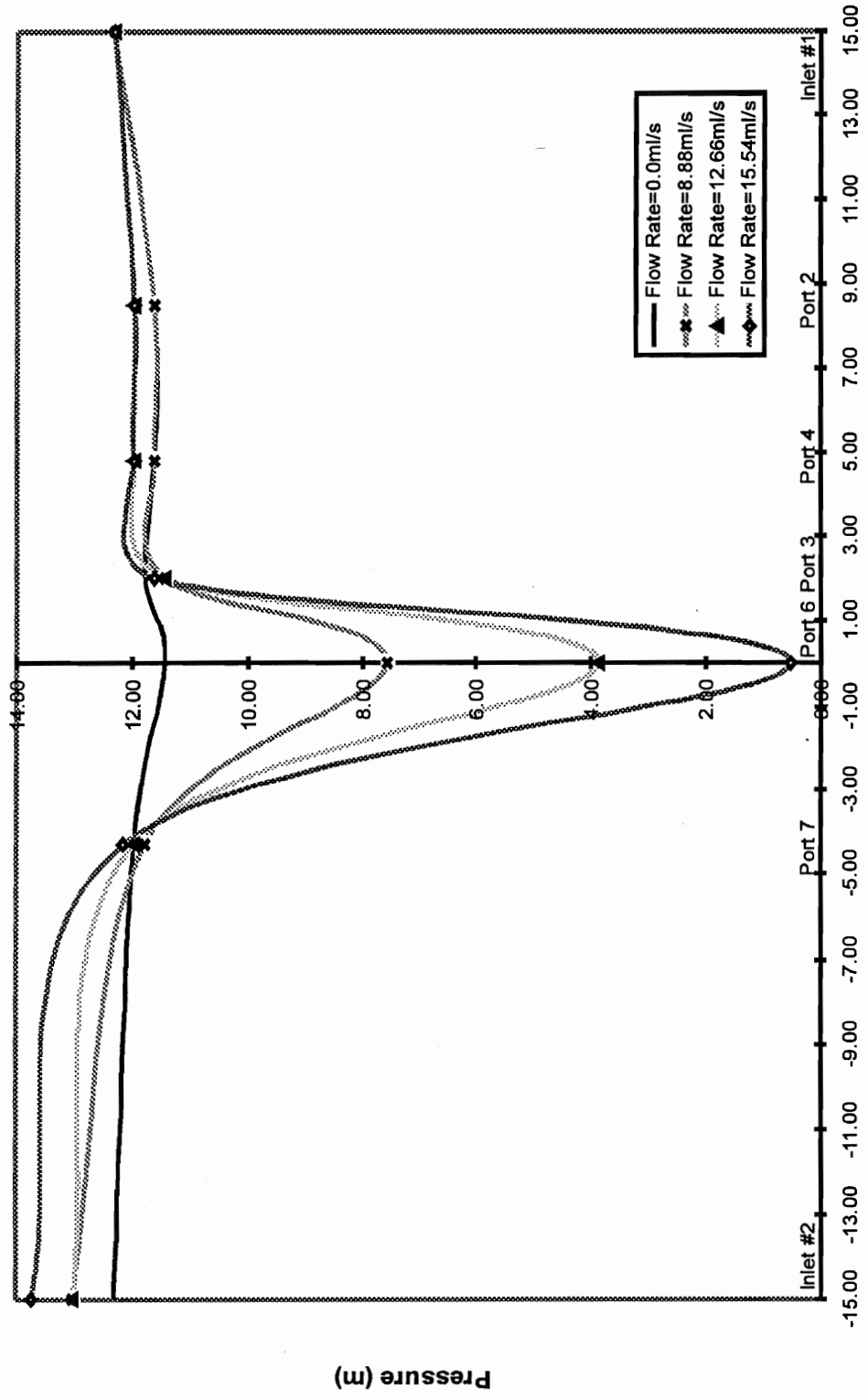

Figure 4-7. Convergent flow trial test 3, single phase, pressures measured across the fracture plane.

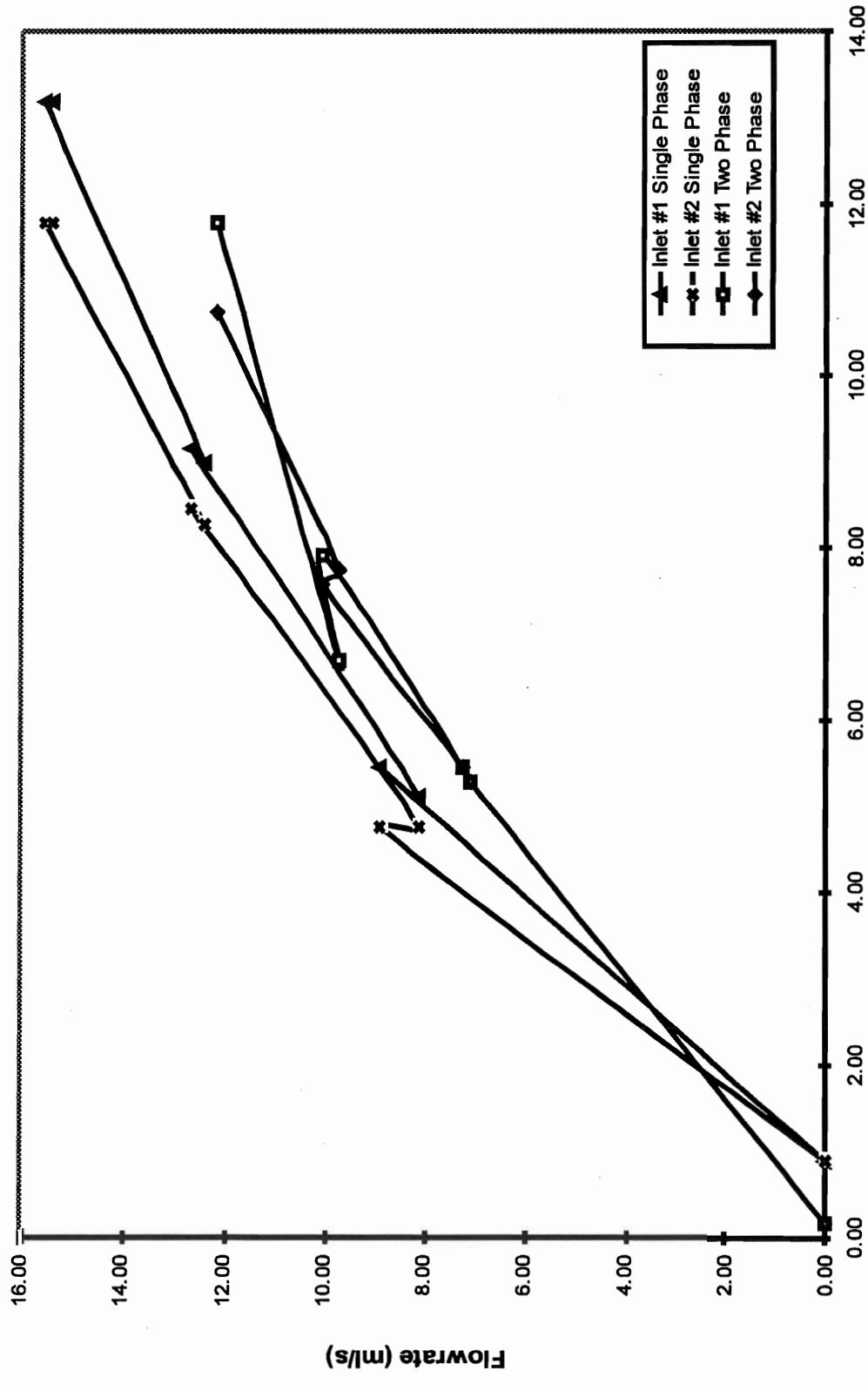

Figure 4-8. Convergent flow trial test 3, flow rate versus pressure gradient between inlet and outlet.

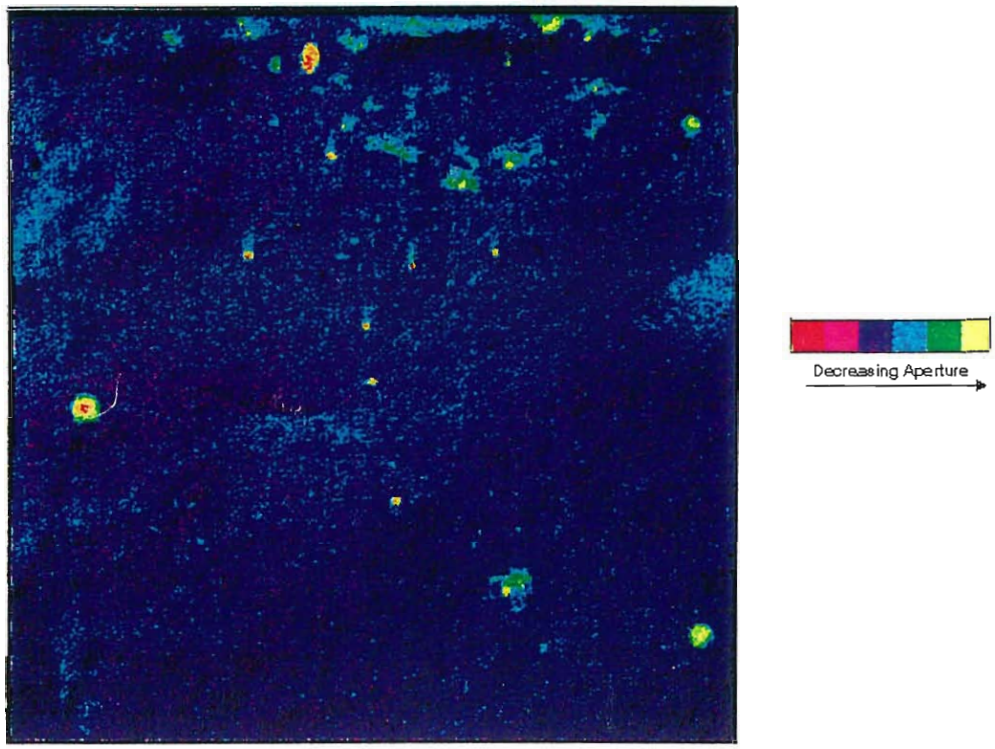

Figure 4-9. Normalized aperture field at 4 psi.

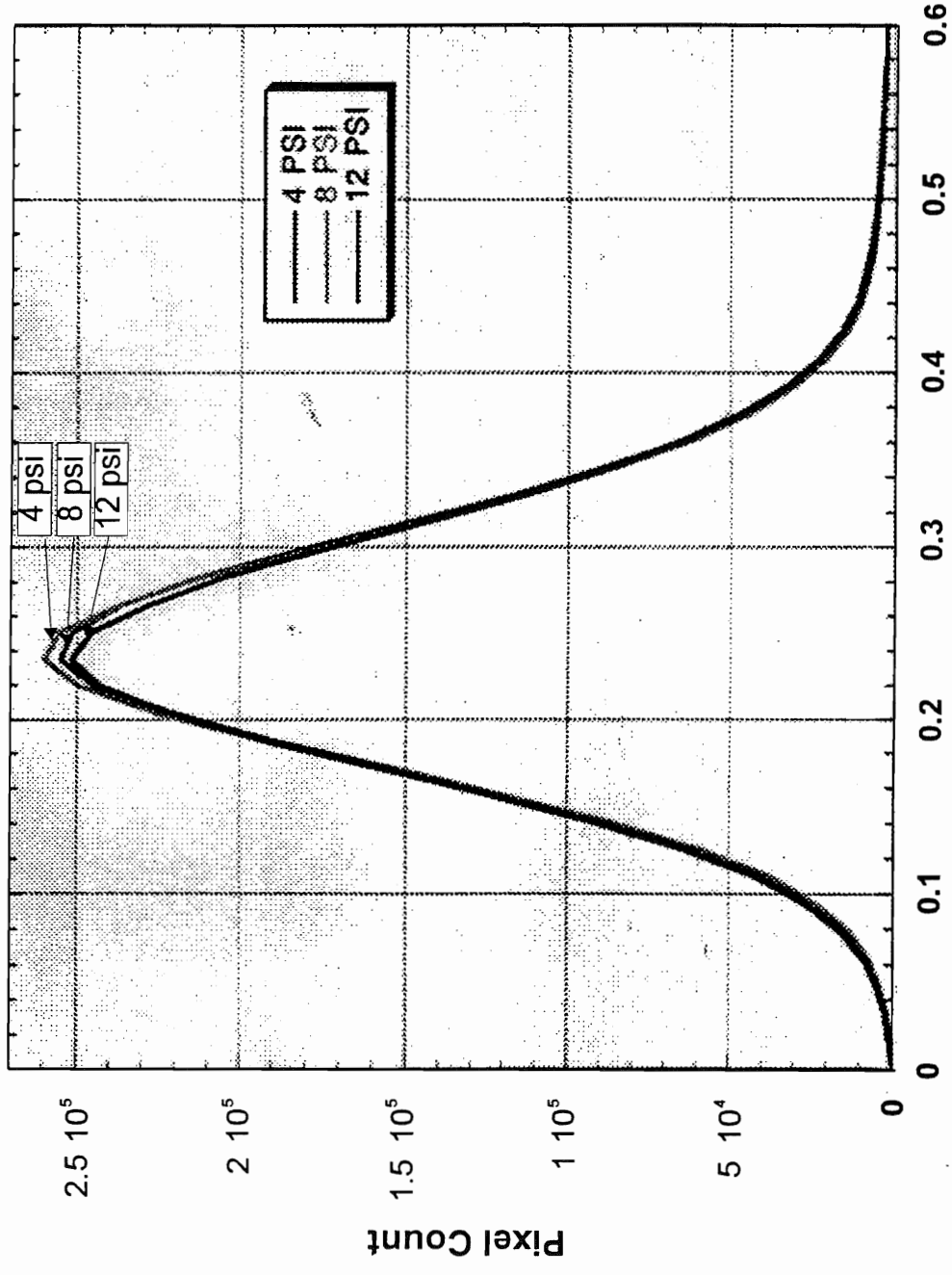

Figure 4-10. Distribution of apertures for three different confining pressures for the fracture replica based on the pixel count over the entire image field.

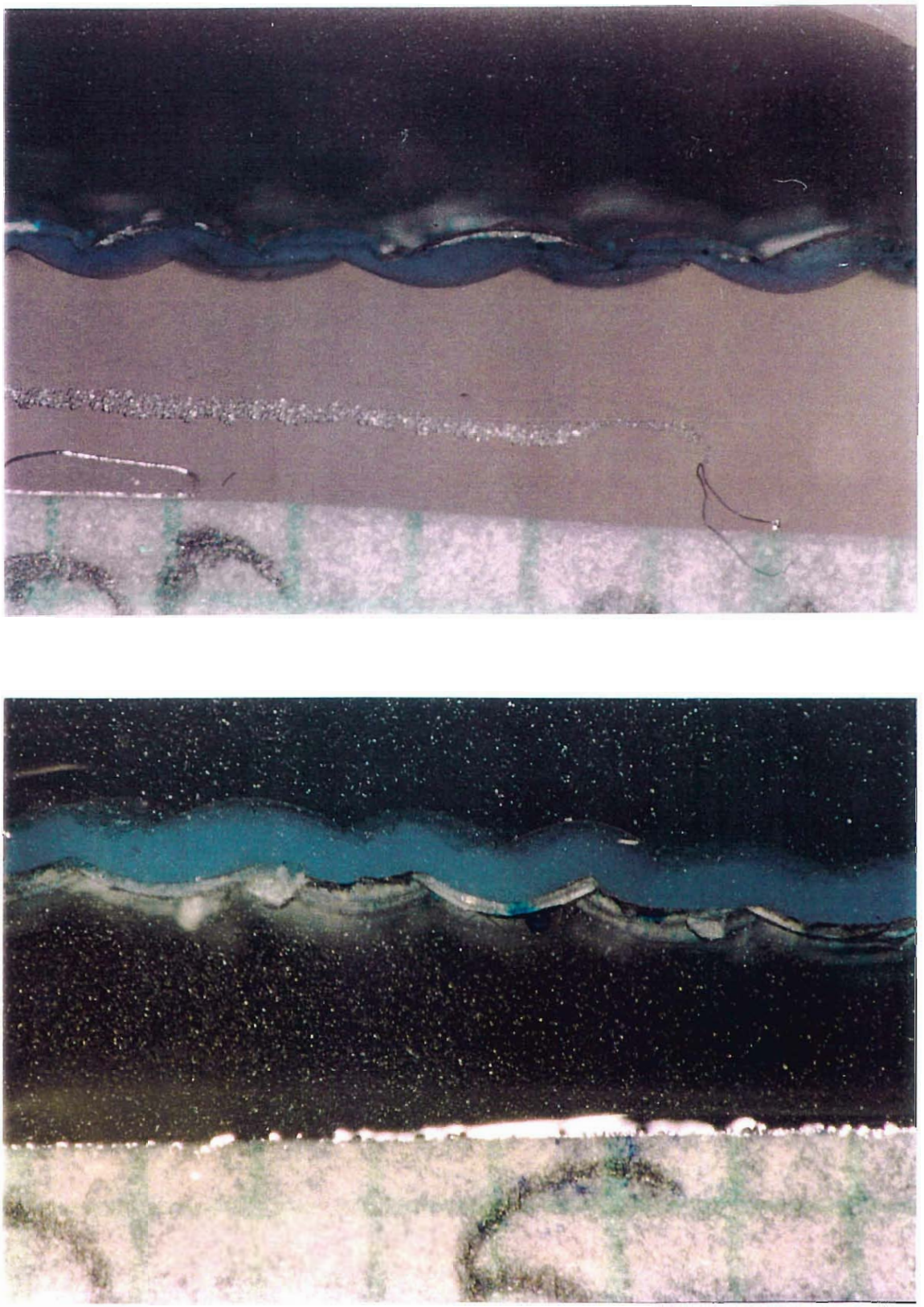

Figure 4-11. Photograph of cross section through resin impregnated replica.

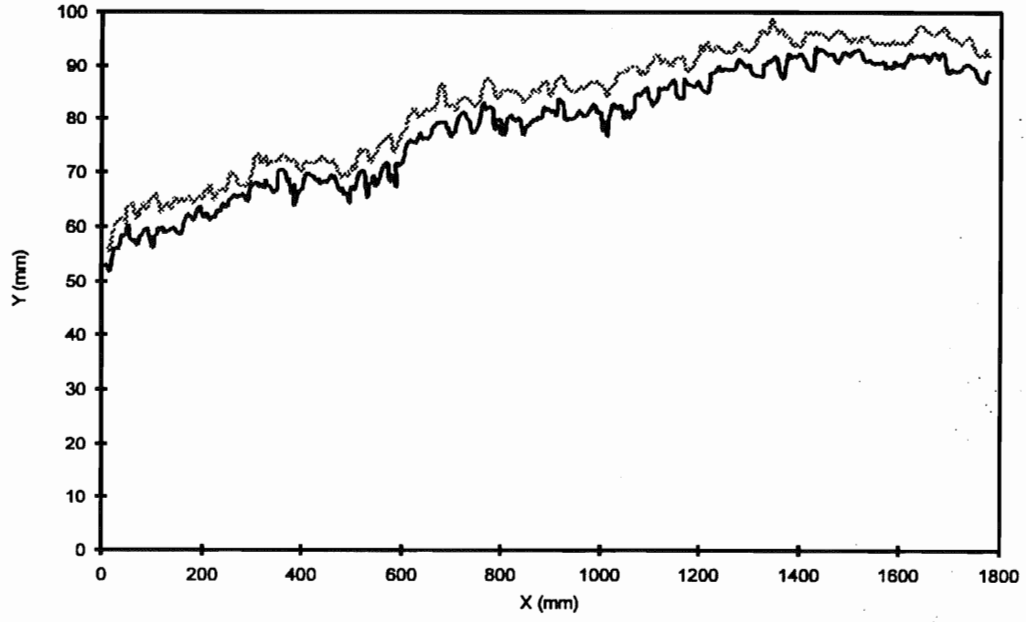

Figure 4-12. Cross section through part of the resin impregnated fracture replica- Profile 3x01a (Part 1).

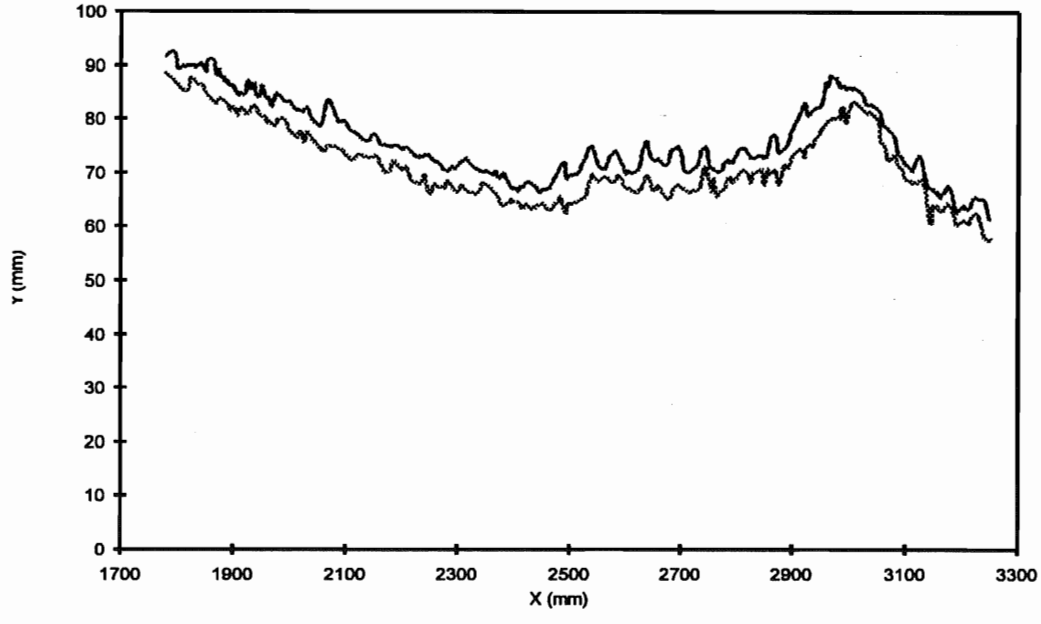

Figure 4-13. Cross section through part of the resin impregnated fracture replica- Profile 3x01a (Part 2).

5 Summary and Conclusions

Three sets of laboratory experiments have been conducted to examine the impacts of gas evolving or degassing within fracture planes as the fluid pressure drops below the bubble pressure, or the pressure at which the water has been saturated with a specific gas, on the transmissivity of discrete fracture planes. The main focus of this work was to determine the relative effects of sample size, fracture deformation, changes in flow regime, two-phase flow and degassing on changes in fracture transmissivity. In addition, these experiments were designed to examine the role of fracture roughness and relative fracture roughness on the trapping capacity of discrete fractures as these factors apply to changes in fracture transmissivity due to degassing.

In the first set of experiments, a series of single phase flow experiments that were being completed on an existing large scale physical model were extended to include a series of two-phase flow experiments. In these two-phase flow experiments, both a water and a gas phase were injected into the fracture plane at the same time. In addition, tests were conducted where a gas saturated water was injected into the fracture plane and the fluid pressure decreased to induce the gas to evolve or degass within the fracture plane. The Large Scale Physical Model (LSPM) provides a fracture surface that is approximately 3.5 square metres in area. This physical model was constructed from high strength concrete and the fracture plane was created by imprinting a geotextile fabric into the concrete surface between the two halves of the model and then separating the two blocks and removing the geotextile material once the concrete had cured. The resulting fracture plane was characterized by a uniform small scale roughness. A 50 mm diameter borehole was drilled into this fracture plane to intersect the fracture plane at an angle of 42 degrees in the center of the fracture plane, creating an elliptical opening or sink within the fracture plane. The fracture plane was instrumented with a series of manometers to measure pressure heads during linear, divergent or convergent flow experiments. Flatjacks, coupled to a reaction frame, were used to change the normal stress acting across the fracture plane and hence induce fracture closure. These changes in load permitted a range of relative fracture roughness to be created in the various single and two-phase flow experiments.

A set of single phase flow experiments was conducted with increasing gradients and flowrates to provide a reference transmissivity at each stress level for the two-phase flow experiments. These single phase flow experiments showed that, with increasing flowrate, the change in flow regime from laminar to turbulent, or some degree of turbulence, produces additional head losses due to increased fluid velocity. When these head losses are used with the measured flowrates to compute fracture transmissivities, major changes in the fracture transmissivity are computed. The addition of gas to the injection water introduces additional head losses and hence additional changes in fracture transmissivity. However, the two-phase flow impacts can be masked by the changes induced by the changes in the flow regime. In addition, the fracture in this LSPM was highly conductive, with a uniform roughness that produced a low gas trapping capacity, and the high flowrates that were associated with the high hydraulic gradients tended to sweep both the raw gas phase during the two-phase experiments and the gas bubbles that were

assumed to have evolved during the degassing experiments out of the fracture plane before the gas could form effective blockage of the fracture pore space. However, despite these offsetting impacts, reductions in fracture transmissivity of up to 80% during the two-phase flow experiments were measured. It is clear that degassing in field situations will be most apparent in rough fractures with low to moderate transmissivities in which the borehole has a small angle of intersection with the fracture plane.

The main effort in this laboratory program consisted of a series of degassing experiments on four small scale samples of both artificial and natural fracture planes. The samples were nominally about 200 mm wide by 300 mm in length. One sample was formed by sand-blasting a sawcut in a limestone sample. The second sample was constructed from high strength concrete using the geotextile approach used in constructing the LSPM discussed above. The two other fracture samples were obtained by overcoring natural fractures at the Pilot Resin site at Äspö. These samples were subjected to a series of normal and shear (for the limestone and concrete samples) loading and unloading cycles that, as the fractures closed and opened, generated a range of relative roughness on the fracture planes. Both single phase, air invasion (imibibition) and air injection tests were conducted on the first two samples. The full suite of tests were completed on the two Äspö samples, including a full suite of degassing experiments at different normal stress levels using water saturated either with carbon dioxide or nitrogen at the water injection pressure.

The air invasion and air injection tests, which focused on measuring the volume of water expelled from the fracture plane, should reflect the differences in the fracture pore structure and the resulting capillary pressure within the fracture plane. It appeared to be difficult to establish reference conditions for each test and for the sequence of tests, due to gas accumulation or flushing between each step in the test sequence. This was particularly apparent when tests using air or nitrogen gas were followed by tests using carbon dioxide gas. For this test sequence, the carbon dioxide tended to flush out the air or nitrogen from the fracture plane, producing an increase in fracture transmissivity rather than a decrease.

For degassing experiments on the first Äspö sample, most of the experiments were conducted with water that was saturated with carbon dioxide gas due to its lower bubble pressure and the higher gas contents that could be achieved at the proposed test pressures. For these experiments, reductions in fracture transmissivity were clearly noted at the different stress levels as the outlet pressure was dropped below the bubble pressure. However, the fracture transmissivity values tended to fluctuate considerably at each pressure step which was assumed to be partly due to a periodic flushing of evolved gas from the fracture plane or capillary pressure effects on the manometer tubes that were used to measure the fluid pressures. This assumption is consistent with the periodic spurts of bubbles of gas in the discharge line. Degassing with nitrogen gas produced a much more stable set of fracture transmissivity values as the outlet pressure was dropped below the bubble pressure. Degassing experiments on the second Äspö sample produced a clear demonstration of the impacts of evolving nitrogen gas on the transmissivity of a discrete fracture. At each normal stress level, as the outlet pressure was decreased below the bubble pressure there was a clear decrease in the fracture transmissivity due to degassing. The role of other factors, such as head loss due to increased fluid velocity and

possible changes in the flow regime from laminar to turbulent flow, in contributing to the observed decreases in fracture transmissivity needs to be assessed.

At the end of each suite of experiments on all four samples, tracer tests were completed at the final loading step, followed by the injection of a room temperature curing resin into the fracture plane. The fracture plane was then sectioned, photographed and the outline of the resin filled fracture plane was digitized. The distribution parameters for the resin filled pore space in each fracture, along with the distribution of the contact areas, was determined for each sample. For the second Äspö sample, the full sample plane was mapped along a series of perpendicular profiles, spaced approximately 10 mm apart. These data were analyzed and the semi-variograms for the pore space were generated. The data were then kriged to determine the spatial distribution of the combined fracture pore space and the contact areas. In addition, the kriged data were used to generate the cell values for a 1.5 mm and a 5 mm grid spacing for the porous media model MODFLOW. Flow simulations demonstrated that using the measured pore space as input parameters with which to calculate cell hydraulic conductivities produced an excellent match between measured and computed flowrates for similar geometry and flow boundary conditions when the 1.5 mm grid values were used. Averaging the apertures over a 5 mm grid reduced the degree of fit between the measured and the computed flowrates.

A key question is how do the gas bubbles as they evolve in the fracture plane reduce the fracture transmissivity. Does the evolving gas fill the large pores or do the bubbles migrate through the pore space and eventually block the smaller pores that form the throats or so called bottle-necks in the fracture pore space? To provide a preliminary assessment of the role of the large and small apertures in reducing fracture transmissivity by degassing, the large apertures were selectively removed from the aperture distribution, and the generated aperture or hydraulic conductivity grid, until the measured degassing flowrates and computed flowrates matched the measured flowrates. To obtain a match for the second step of the degassing experiment, at 10 MPa for the second Äspö sample, the overall volume of the fracture pore space had to be reduced to 80.5 % of the initial pore space volume that was used in the single phase modeling. To fit the numerical model to the measured flowrates at step 3 of this degassing experiment the pore space volume only had to be reduced to 94.6% of the original pore space volume that was represented in the numerical model.

To model the effects of gas blocking the smaller apertures, the smaller apertures were successively removed from the numerical model and set to the minimum value. In the original model, the smallest aperture was 0.002 mm. To match flowrates computed by the model to the flowrates measured in step 2 all apertures up to 0.100 mm had to be removed which represented a reduction of the fracture pore space volume to 91.9 % of the original pore space volume. This reduced the average fracture aperture from 0.158 mm to 0.145 mm. To fit the model to the step 3 data, only apertures up to 0.074 mm had to be removed, resulting in an average aperture of 0.152 mm, such that the volume of the fracture pore space was equal to 96.1 % of the original pore space volume. This set of simple numerical simulations suggests that blocking the small pores with gas bubbles will be more effective in reducing the fracture transmissivity, because of the smaller volumes of gas required. Detailed two-phase flow, discrete fracture, simulations

will be required to determine the transients involved and to determine if the small pores can be effectively blocked in the presence of the local pressure gradients that would exist across the small pores.

The final set of laboratory experiments consisted of constructing replicas of the fracture surface that was used in the LSPM experiment and in the concrete sample. This replica had a very high hydraulic conductivity and a very low bubble trapping capacity. These two factors produced high fluid velocities that effectively swept the bubbles from the fracture pore space before they had an opportunity to coalesce and block the fracture pore space. The observed changes in fracture transmissivity with increasing gradients included both degassing effects and effects due to changes in the flow regime.

This suite of laboratory experiments and preliminary numerical simulations have demonstrated that degassing within fracture planes can produce significant changes in the apparent transmissivity of discrete fractures. The relative impact of degassing on fracture transmissivity is determined both by the magnitude of the fracture transmissivity, the fracture roughness or trapping capacity of the fracture plane, the type of gas present in the water phase and the percent of the gas that is dissolved in the water. In addition, the flow geometry and the resulting changes in flow regime with increasing flowrate or increasing hydraulic gradient can both mask changes in the observed fracture transmissivity and amplify these changes.

6 Acknowledgments

This applied research project has stretched over a considerable period of time, far more than was originally anticipated. Numerous individuals have contributed to the discussions and to the experimental work as well as to the data analysis and report preparation including Peter Lemessurier, Graham Dillabough, Jim Slade, Yan Ma, Barbara Collett, Robert MacLeod, Suelynn Dignard, Colleen Richards, Amy Feltham, and long list of undergraduate students and technical support staff at Memorial University. The Engineering Geology group at Memorial University provided the experimental facilities for the experimental work. The fracture replica work was completed at Sandia National Laboratory by Dr. Robert Glass and his research group with the assistance of Fracflow staff. Dr. Glass provided overall guidance, essential materials, key technical staff and the laboratory infrastructure with which to carry out these initial experiments.

Considerable advice on experimental procedures was provided by Dr. Georgia Destouni and Dr. Jerker Jarsjo of KTH, Dr. Olle Olsson of SKB and the staff at Äspö. Contract funding for this project was provided by SKB. Dr. Olle Olsson provided overall project management for SKB and his patience and support during the extended period of this project are greatly appreciated.

7 References

Atkinson, L.C., Gale, J. E. and Dudgeon, C.R., 1994. New insight into the step-drawdown test in fractured-rock aquifers. Applied Hydrogeology, Vol. 1., p. 9 to p.18.

Deutsch, C.V. and Journel, A.G., 1992. GSLIB - Geostatistical Software Library and User's Guide. Oxford University Press, 340 pp.

Fetter, C.W., 1994. Applied Hydrogeology, Third Edition, 691 pp.

Gale, J., MacLeod, R., and LeMessurier, P., 1990. Site characterization and validation - Measurement of flowrate, solute velocities and aperture variation in natural fractures as a function of normal and shear stress, Stage 3. Stripa Project, Technical Report 90-11, SKB, Stockholm, Sweden.

Gale, J. E., 1994. Assessment of the coupled effects of degassing and excavation induced fracture deformation on drift inflows - feasibility study and preliminary experiments - single fractures. SKB, Stockholm, Sweden.

Klingberg, K., 1996. Sampling for determination of contents and composition of gas dissolved in water (Personal communication).

Lomize, G. M., 1951. Flow in fractured rocks, (in Russian). 127pp., Gosenegoizdat, Moscow.

Long, J. C. S., Olsson, O., Martel, S., and Black, J., 1995. Effects of excavation on water inflow to a drift, in *Fractured and Jointed Rock Masses*, Proceedings, of the conference on fractured and jointed rock masses, Lake Tahoe, California, edited by Myer, L.R., Tsang, C.-F., Cook, N.G.W. and Goodman, R.E., A.A. Balkema, Rotterdam, Brookfield, pp.543-549.

McDonald, M.G. and A.W. Harbaugh. 1998. A Modular Three-Dimensional Finite-Difference Ground-Waer Flow Model, Book 6, Modelling Techniques.

Olsson, O., 1992. Site Characterization and Validation Project. Stripa Project, Final Report 92-22, SKB, Stockholm, Sweden.

Rissler, P., 1978. Determination of the water permeability of jointed rock. Publ. 5, Inst. For Found Eng., Soil Mech. and Water Ways Constr., Aachen Univ. Aachen, Federal Republic of Germany, 150 pp.

Wahlberg, A., 1995. Two phase flow equipment for injection of gas saturated water (Manual) (Personal Communication).

Reda, D.C. and Hadley, R. G., 1985. Saturated permeability measurements on pumice and welded-tuffaceous materials. In Prog. Inter. Cong., Inter. Assoc. of Hydrol., Hydrogeology of rocks of low permeability, Univ. of Arizona, Jan. 7-12, 1985.

Rissler, P., 1978. Determination of the water permeability of jointed rock. Publ. 5, Inst. For Found Eng., Soil Mech. and Water Ways Constr., Aachen Univ. Aachen, Federal Republic of Germany, 150 pp.

Wahlberg, A., 1995. Two phase flow equipment for injection of gas saturated water (Manual) (Personal Communication).